Università degli Studi di Cagliari

DOTTORATO DI RICERCA

In Scienze e Tecnologie Chimiche

Ciclo ……XXX …...

TITOLO TESI

Siliceous and non-siliceous mesostructured iron oxide nanocomposites for H_2S removal from syngas

Settore/i scientifico disciplinari di afferenza

CHIM/02

Presentata da: Claudio Cara

Coordinatore Dottorato Prof. Stefano Enzo

Tutor Prof.ssa Carla Cannas

Esame finale anno accademico 2016 – 2017

Tesi discussa nella sessione d'esame Marzo 2018

University of Cagliari

PhD Course in Chemical Science and Technologies

XXX cycle

Siliceous and non-siliceous mesostructured iron oxide nanocomposites for H_2S removal from syngas

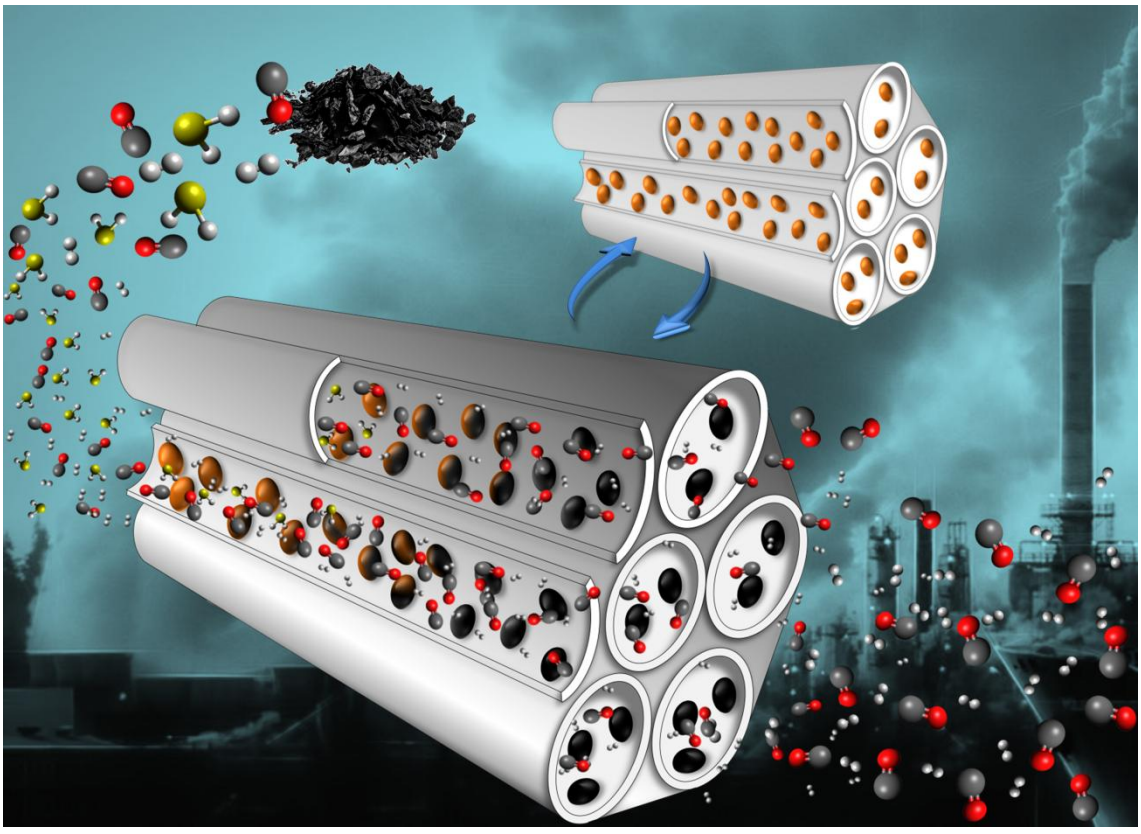

Supervisor

Prof. Carla Cannas

Candidate

Claudio Cara

Acknowledgments

Firstly, I would like to express deep gratitude to my supervisor Prof. Carla Cannas for her guidance, encouragement and gracious support throughout the course of my work, for his expertise in the field that motivated me to work in this area and for is faith in me at every stage of this research.

Besides my advisor, I would like to thank the rest of the research group of Solid state chemistry and nanomaterials from the University of Cagliari: Prof. Anna Musinu, Dr. Andrea Ardu, Dr. Valentina Mameli, Dr. Marco Sanna, Dr Mirko Vacca and Daniel Niznansky from the Charles University of Prague, for their help, support and encouragement. Also I thank my friends Alessandro and Federica for all the fun we have had in the last three years.

I wish to thank all of my co-authors who, with their expertise, have helped me to sharpen the ideas presented in our papers.

My sincere thanks also goes to Prof. Markus Antonietti, Dr. Bernhard Schmidt from the department of Colloids and Interfaces of Max Planck Institute of Potsdam, who provided me an opportunity to join their team as intern, and who gave me access to the laboratory and research facilities. Without their support it would not be possible to conduct this abroad experience.

Last but not the least, I would like to thank my family for supporting me throughout this PhD path and my life in general.

Consorzio AUSI is acknowledged for having funded my PhD grant.

Table of contents

Foreword

The aim of this thesis is to give a contribution to develop new mesostructured iron oxide-nanocomposites for sulphur compounds removal in view of possible applications in syngas, natural gas, hydrogen and air purification. Desulphidation has been receiving dramatic attention since sulphur compounds are hazardous, corrosive and toxic gases that cause environmental and industrial damages, as the pipeline corrosion and catalysts deactivation. Specifically, the present thesis focus on the desulphidation of syngas deriving from coal at mid-temperature conditions. In fact, coal is the largest available fossil fuel, being the world reserves estimated to last 148 years, and represents the most employed global energy source. Moreover, the combination of Integrated Gasification Combined Cycle (IGCC) with Carbon Capture and Sequestration (CCS) could in principle solve the main drawback of the use of coal, *i.e.* the carbon dioxide production, by keeping the cost of power from this coupled plant only 60 % higher than conventional IGCC. This contributes to make coal still an appealing feedstock for energy production. In this framework, the key challenge for producing clean power or hydrogen *via* gasification is the effective purification of the sour syngas, which is usually carried out at low temperatures (around 50 °C), leading to losses in the energy efficiency of the plant. Technologies to clean at temperatures between 300 °C and 600 °C (mid-temperature range) have been investigated in order to sort this issue out. Mesostructured metal oxide-based nanocomposites can be proposed as potential removers in this specific range of temperatures due to their promising features and thermal stability. They consist of a mesostructured inert support able to disperse homogeneusly the active phase. Iron-based systems were chosen as active phase due to their fast kinetics and favourable thermodynamics of the reaction with H_2S, as well as for their low cost and no toxicity. The use of an inorganic mesostructured materials with different textural properties (surface area, pore size and pore structure) as a host for iron oxide nanoparticles can provide an effective way to tailor their size and size distribution and to control its dispersion. From this point of view, mesostructured silica and titania can act as excellent supports. The sol-gel techniques at the basis of their synthesis, due to its great versatility and large number of parameters controlling the process, offer the possibility to obtain products with the demanded characteristics. Based on these points, the first part of the work is devoted to identify the experimental conditions for the synthesis of mesostructured silica and titania supports, stable at the operating temperature and suitable in terms of textural proprieties to host the active phase. In the second part, the most promising supports have been selected to prepare the corresponding iron-oxide-based

nanocomposites and tested for H_2S removal at mid-temperature. The correlation between the textural and structural properties of the nanocomposites with their performances has allowed to get new insights for the development of more and more efficient H_2S sorbents.

This thesis consists of seven chapters organized as follows:

Chapter 1 provides an introduction on mesostructured siliceous and non-siliceous metal oxides, describes the main approaches for their synthesis and their possible application in different fields.

Chapter 2 gives an overview on coal gasification technologies, focusing on the approaches commonly proposed to remove H_2S from sour syngas, known as *syngas sweetening* strategies.

Chapter 3 is devoted to the description of the sorbent requirements for an efficient mid-temperature sweetening process, with particular emphasis on mesostructured nanocomposites.

Chapter 4 deals with the development of synthetic strategies to fabricate mesostructured siliceous (SiO_2) and non-siliceous (TiO_2) supports, with specific attention on the tuning of their textural properties as surface area, pore diameter, wall thickness and particles dimension.

Chapter 5 is dedicated to verify the suitability of MCM-41, in comparison with commercial and SBA15-based sorbents, as novel mesostructured support to create efficient and regenerable Fe_2O_3 nanocomposites (γ-Fe_2O_3@MCM-41) for mid-temperature H_2S removal.

Chapter 6 is aimed to study the effect of different pore structures (hexagonal and cubic) and wall thickness of MCM41S supports on the H_2S removal performances of the corresponding iron oxide-based sorbents.

Chapter 7 is focused on the behaviour, under conditions simulating the syngas composition, of the most promising iron oxide-MCM41 sorbent and of a new sorbent in which the iron oxide phase is embedded into a mesostructured crystalline titania.

At last, some general conclusions about the achievements of the present work are given.

Appendix reports the details of the characterization techniques and setup of the scale-laboratory pilot plant for the sulphidation-regeneration tests.

1. Siliceous and non-siliceous mesostructured oxides and their potential applications

Abstract

This chapter deals with mesostructured siliceous and non siliceous metal oxides highlighting the approaches for their synthesis, their features and their possible applications as sorbents, catalysts and sensors.

1.1 Introduction

The different local environment of atoms located at the surface of a given solid, is the driving force of many physical and chemical processes. Two main approaches can be employed to maximize the number of surface atoms in solids: one is based on the reduction of the size of dense particles down to the nanometer scale, while the other is the creation of an open porous network within the solid (porous material).[1] Although both approaches lead to an increase in surface area, the effect of the former is quite limited while the latter provides a greater degree of versatility by playing with size, shape, and tridimensional organization of the pores. In this framework, within the class of the porous materials, the maximization of the surface area can be achieved when the pores have a diameter below 50 nm and are organized in a well-defined structure (microstructured and mesostructured porous materials). The peculiar features of these materials open the way for a wide range of potential applications to solve global issues, such as increasing energy demands, and at the same time more rigorous environmental standards for industrial pollutants, depletion of resources, and health improvement.[1]

1.2 Porous materials

According to the International Union of Pure and Applied Chemistry (IUPAC),[2] porous materials are divided in three classes depending on their pore size:

- Microporous (pore size <2 nm)
- Mesoporous (2 nm ≤ pore size ≤ 50 nm)
- Macroporous (pore size > 50 nm)

Among them, microporous materials offer the highest surface area, but the intrinsically small dimensions of the pores represent a serious limitation for mass transfer when reactions involve the use of large reactant molecules.[3] Within this class the best known members are zeolites, which show a narrow and uniform micropores size distribution due to their crystallographic defined pore system.

In the attempt to improve the diffusion of the reactants, a great effort has been focused on the enlargement of pore size into the mesoporous range. Mesoporous materials can be therefore considered the right compromise in order to retain high surface area and prevent diffusion drawbacks or plugging *phenomena*, endowing them with potential applications in catalysis, adsorption, sensor, lithium-ion batteries, drug delivery, and nanodevices. Among them, **Ordered Mesoporous Materials (OMM),** also known as **Mesotructured Materials**, possess well-arranged pore channels and extraordinarily large surface areas, which do not only greatly maximize the reactivity toward a specific target or the adsorption capacities, but also facilitate the access within the pore system.[4] Silica and alluminosilicates were the first OMM discovered and two of the most frequently inorganic frameworks studied due to their tetra-connected covalent bonds and their chemical stability.[3] Furthermore, the geometrical flexibility of the tetrahedral building blocks allows their relatively facile synthesis. Despite its great potentiality (chemically stable, inert, high surface areas), silica is an inactive material both as catalyst as well as sorbent and it can be used only as host material for active phases. For these reasons, research is moving toward new non-siliceous mesostructured materials showing activity for diverse applications. Unfortunately, the synthetic strategies used for mesoporous silica are not applicable to non-siliceous oxides and the new synthetic approaches proposed up to now are not yet able to guarantee comparable results. This is mainly due to the high reactivity (hydrolysis) of the non-siliceous precursors, to the possible concomitant redox reactions, or phase transitions, accompanied by thermal breakdown of the mesoporous structural integrity. Therefore, a unique synthetic pathway for the production of a high quality mesostructured non-siliceous materials is still a great challenge for most metal oxides. Being remarkable the differences in terms of synthetic routes, chemistry reactions and corresponding results between siliceous and non-siliceous mesostructured oxides, in the next paragraphs their description will be discussed separately.

1.2.1 Mesoporous siliceous materials

Particular attention will be paid on the description of the strategies to obtain ordered mesoporous siliceous materials which show better features than their counterpart with disordered mesoporous structure.

The first synthesis of an ordered mesoporous material was described in a patent published in 1969.[5] However, due to a lack of analysis, the remarkable features of this product were not recognized.[3] In 1992, a similar material, MCM-41, which stands for Mobil Composition of Matter No. 41, was obtained by scientists at Mobil Oil Corporation laboratories, opening a new field of research.[6] The comprehensive characterization shows a highly ordered hexagonal array of unidimensional pores with a very narrow pore size distribution and an extremely high surface area. Since then, a huge effort has been devoted to the development of synthetic strategies and the study of new applications for these fascinating materials and a large variety of mesostructured materials with different porous structure (two-dimensional (2D) hexagonal, space group *P6mm*, three-dimensional (3D) hexagonal *P6$_3$/mmc*, 3D cubic *Pm3m*, *Pm3n*, *Fd3m*, *Fm3m*, *Im3m*, and bicontinuous cubic *Ia3d*) have been obtained (Figure 1.1).

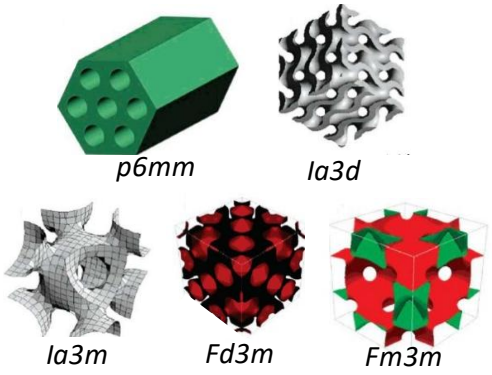

Figure 1.1 Representation of most common porous structures obtained for siliceous mesostructured materials

The principles behind the formation of mesostructured material is the organic-inorganic assembly between the inorganic species (silica precursor or very small entity of silica) and the organic molecules (amphiphilic copolymers or surfactants) used as template. The organic-inorganic assembly is driven by weak non-covalent bonds such as hydrogen bonds, van der Waals forces, and electro-valent bonds between the surfactants and the inorganic species. Two main pathways, *cooperative self-assembly* and *true liquid-crystal templating processes*, appear to be effective routes in the synthesis of mesostructures, as shown in Figure 1.2. In the case of *cooperative self-assembly*, the interaction between inorganic species and organic molecules occurs before the micelles formation. The resulting assembly is coordinated by both organic and inorganic entities (pathway A). In the case of *liquid-crystal templating*, the formation of liquids crystals by the assembly of the organic molecules occurs before the interaction with the inorganic species and is followed by the condensation of the inorganic precursor around the surfactant phase (pathway B).

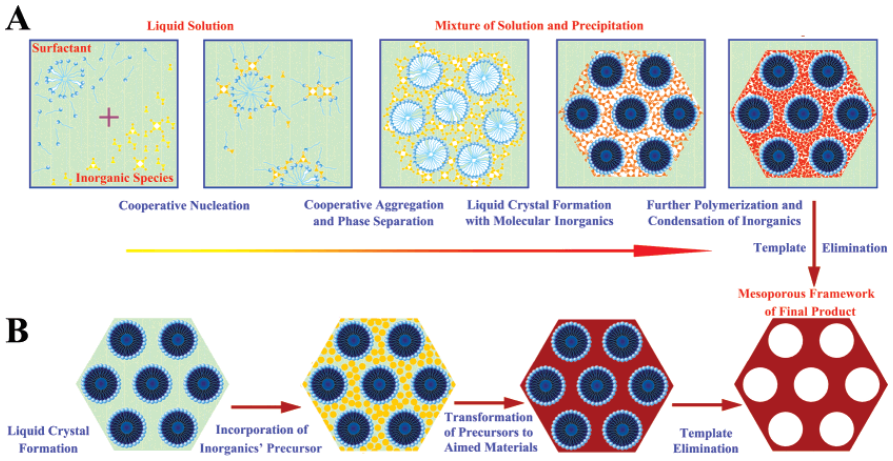

Figure 1.2 Two synthetic strategies to obtain mesostructured materials: cooperative self-assembly (A); true liquid crystal templating process (B). (Templated Synthesis for Nanoarchitectured Porous Materials). Reprinted with permission from ([7]). Copyright (2007) American Chemical Society

The formation of the mesostructured materials was also described in terms of the free energy in the whole process:[8]

$$\Delta G = \Delta G_{inter} + \Delta G_{wall} + \Delta G_{intra} + \Delta G_{sol} \qquad \textit{equation 1.1}$$

where ΔG_{inter} is the energy associated with the interaction between inorganic walls and surfactant micelles, ΔG_{wall} is the structural free energy for the inorganic framework, ΔG_{intra} is the van der Waals force and conformational energy of the surfactant, and ΔG_{sol} is the chemical potential associated with the species in solution phase. For the surfactant-templating assembly of mesostructured silicates, ΔG_{sol} can be regarded as a constant in a given solution system. Therefore, the key factor is the interaction between the surfactant and inorganic species, such as the matching of the charge density. The more negative ΔG_{inter} is the more easily the assembly process proceeds. Elaborated investigations on mesoporous materials have been focused on understanding and utilizing the inorganic-organic interaction.[7] By changing reaction conditions, such as pH, chemicals, inorganic precursors, and templating agents, six routes have been proposed for the syntheses of ordered mesoporous compounds (Figure 1.3). The interactions between the charged inorganic phase and the head group of the surfactants in the route (a-d) are mainly electrostatic, while those between neutral inorganic species and non-electrolyte templating molecules are given by hydrogen bonds (e, f).[9]

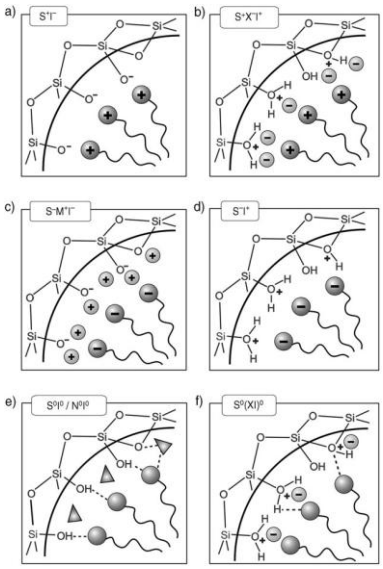

Figure 1.3 Different kinds of interactions between inorganic species and surfactant head groups through electrostatic interactions in basic (a, c), acidic (b) and neutral (d) media or via hydrogen bonds between uncharged species (e) or ion pairs (f). Reproduced with permission from [10]. Copyright 2006 WILEY-VCH Verlag GmbH.

Besides the inorganic-organic interactions, other important key factors that make silica particularly suitable for the mesostructure formation are the well-controlled hydrolysis and condensation of the silica precursors (e.g., siliceous alkoxides), and the thermal stability of the silica framework during the removal of the organic molecular templates (calcination).

1.2.2 Mesoporous non-siliceous materials

Mesoporous non-siliceous oxides have attracted interest due to their unique properties and potential applications. Since the discovery of mesoporous silicates in 1990s, organic-inorganic assembly processes by using surfactant or block copolymers as soft templates have been considered as a feasible path to create mesopores also in metal oxides. However, the wonderful results obtained for siliceous materials, based on the soft template approach, have not been repeated for metal oxides. Therefore, different synthetic pathways have been developed with the ambition to propose a unique and well-defined route able to guarantee a precise mesoporous structure for each metal oxide. During the last two decades, four different synthetic routes have been developed (Figure 1.4):

***Soft template*:** based on the same principles of the synthesis of mesostructured siliceous materials, in which surfactant or block copolymer have been used as templates, with particular adaption in the synthetic route.

***Hard template*:** based on the use of ordered mesostructured silica or carbon preformed as scaffold.

***Colloidal crystal template*:** based on the formation of a uniform close packing by the arrangement of organic (polystyrene (PS), poly-(methyl methacrylate) (PMMA)) or inorganic (silica) uniformly sized spheres and the subsequent filling of the interstitial spaces by inorganic precursors.

***Super lattice*:** based on the use of pre-formed capped-nanoparticles as building blocks, and the interaction and assembly between the capping agent of the nanoparticles and the surfactant (or block copolymers) used as porogen agent to form the mesoporous structure.

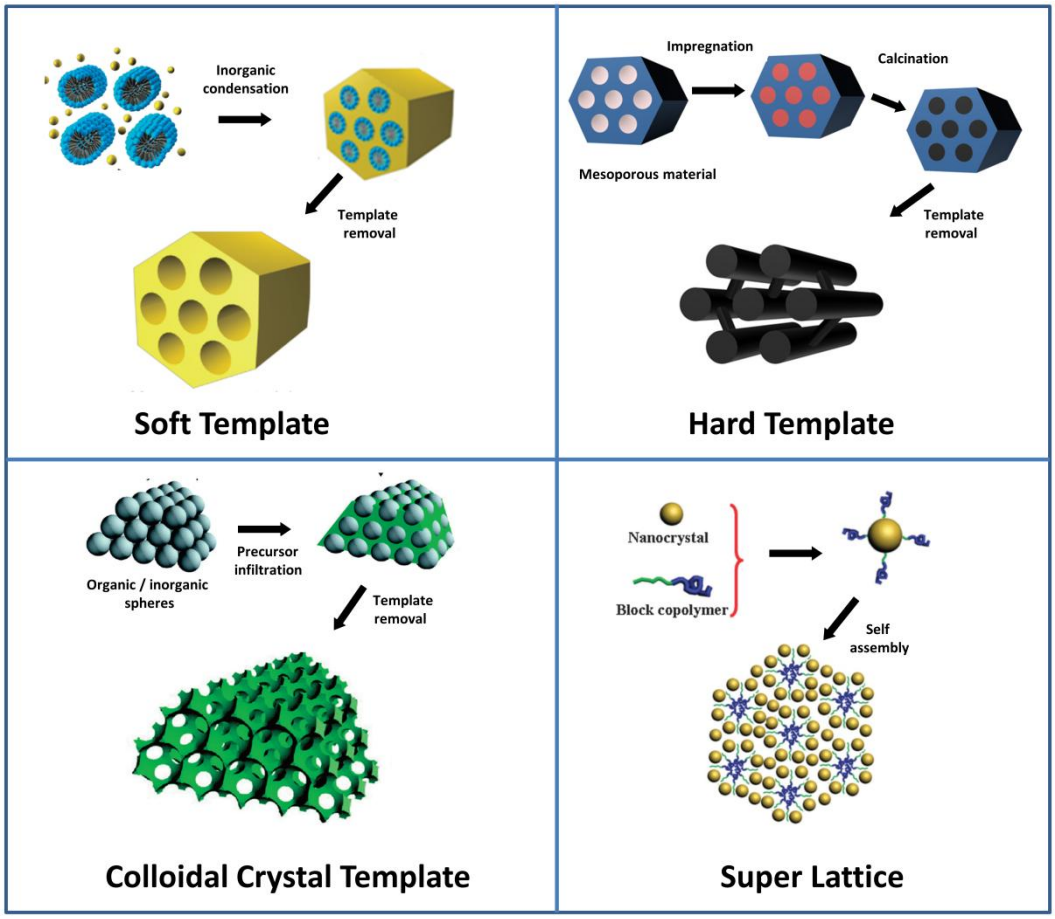

Figure 1.4 Different synthetic pathways developed to obtain ordered mesoporous materials. Adapted with permission from ([11]). Copyright (2008) American Chemical Society. Reprinted from Mingfeng Chen, Huaqing Xuan, Xiaozhong Zheng, Jiyang Liu, Xiaoping Dong, Fengna Xi, N-doped mesoporous carbon by a hard-template strategy associated with chemical activation and its enhanced super capacitance performance, 238, 269-277, Copyright (2017), with permission from Elsevier (Hard template) Adapted from ([12]) with permission of The Royal Society of Chemistry.

The soft template methods suffer from the major problem of losing the porous structure after crystallization of the inorganic precursors, while the hard template and the colloidal crystal template methods are multistep approaches and, as a consequence, hardly applicable in industrial process. Even though the main drawback of the crystallization step could be overcome by the super lattice method, in which the pre-formed nanoparticles are used instead

of an inorganic precursor, it is difficult to properly choose the suitable capping agent and the porogen agent in order to promote the interaction between the two species and the subsequent assembly. Considering the versatility of soft template strategies, to overcome the soft templates issues related to the thermal stability of the porous structure, scientists have learned to develop and use amphiphilic block copolymers with higher thermal stability than temperature of crystallization transition, making this method promising and most useful when compared with the others. Therefore, hereinafter, the attention will be paid on the soft template method.

1.2.2.1 Soft template methods

The most obvious approach to synthesize ordered mesoporous metal oxides is the direct adaption of the pathways that have been successfully applied in the synthesis of mesostructured silica. However, in the same sol-gel aqueous conditions, due to the faster reaction of hydrolysis and condensation of the metal precursors compared to the siliceous one, the loss of the ordered porous structure has always been observed, with the consequent formation of a wormlike porous structure. Apart from a controllable hydrolysis-condensation rate reaction issue, a strong interaction between the templates and precursor is necessary to form ordered mesostructures and avoid macroscale phase separation. On the basis of these points, the first successful synthesis of mesostructured metal oxide was set up in 1995 by Antonelli *et al*.,[13] in which a modification of the sol-gel process permitted to obtain amorphous mesostructured TiO_2. Unfortunately, the resulting materials showed very low thermal stability and traces of phosphate groups after template removal, deriving from the tetradecyl phosphate used as template. In 1999, Stucky and co-workers,[14] proposed a unique method able to synthesize different crystalline metal oxides (TiO_2, ZrO_2, Al_2O_3, NbO_5, Ta_2O_5, WO_3, HfO_2, SnO_2) and amorphous mixed oxides ($SiAlO_{3.5}$, $SiTiO_4$, $ZrTiO_4$, Al_2TiO_5 and ZrW_2O_8), based on the use of amphiphilic tri-block copolymers as templates that, being more robust of the conventional surfactants, guarantee a better thermal stability of the mesostructured metal oxide (Figure 1.5). Block copolymers, such as Pluronic-type triblock, enable to directly obtain a robust mesostructured with long-range ordering lengths, are considered to be one of the most promising templates for the crystal growth of inorganic materials.[15] Their use can be considered one of the key parameter in the development of mesostructured metal oxides. Besides the choice of the copolymer, another crucial step is the sol-gel transition through slow evaporation of the solvent. This approach was firstly presented as solvent evaporation method by Bricker's group for mesostructured silica in 1997[16] and successively called evaporation-

induced self assembly (EISA).[17] The next paragraph will give details of this particular synthetic approach.

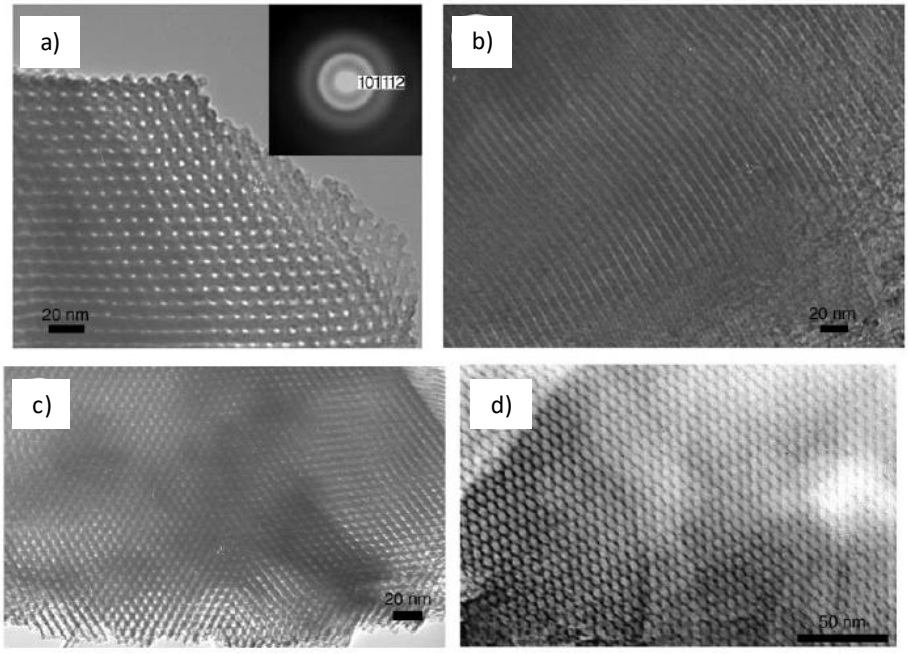

Figure 1.5 TEM images of ZnO_2 (c, d) and Nb_2O_5 (e, f) mesostructured oxides. Reprinted by permission from Macmillan Publishers Ltd [Nature] ([14]), copyright (1998)

1.2.2.2 Evaporation-induced self assembly (EISA)

Originally designed for the preparation of mesostructured silica thin films,[16] the EISA method has been well adapted to mesostructured metal oxide.[14] Being essentially based on sol-gel reactions, the use of non-aqueous solvents allows to strongly slow down the hydrolysis and condensation rates of metal species.

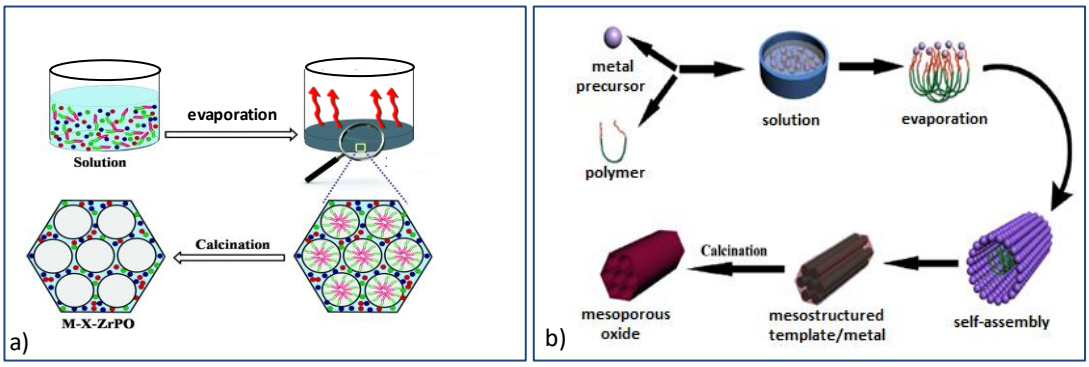

Figure 1.6 Schematic representation of the EISA synthetic approach. (a) Adapted from ([18]) with permission of The Royal Society of Chemistry. (b) Reprinted from Soft templating strategies for the synthesis of mesoporous materials: Inorganic, organic–inorganic hybrid and purely organic solids, 189, Nabanita Pal, Asim Bhaumik, 21-41, Copyright (2013), with permission from Elsevier

Basically, inorganic precursors with low polymerization degrees are dissolved in a volatile polar solvent (typically alcohols or tetrahydrofuran), containing a surfactant. The initial concentration of the surfactant in this solution has to be much lower than the critical micelle concentration (CMC). Slow evaporation of the solvent leads to a gradual increase of the concentration of the surfactant, and to the consequent formation of a liquid-crystal phase, which interacts with the inorganic species. A subsequent humidity aging process, aimed to facilitate the cooperative assembly between inorganic species and block copolymer molecules, should then lead to a robust and highly organized mesostructure.[15] The inorganic framework can be further solidified and crystallized by a post treatment and the surfactants can be easily removed by calcination (Figure 1.6). In situ small angle X-ray scattering (SAXS) coupled with interferometry analysis have been used by Sanchez and co-workers[19] to study the formation of mesostructured TiO_2. It has been found that the hybrid mesostructure was formed through a disorder-to-order transition step from an isotropic sol to a worm-like phase, up to an aligned and organized micelle phase. The authors found a transition during the aging step, from a cubic porous structure to a triclinic one (Figure 1.7).

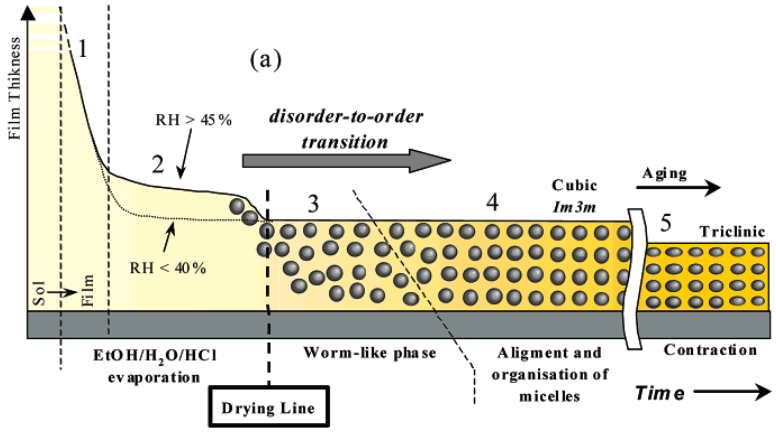

Figure 1.7 Schematic representation of the stages of film formation during the dip-coating process. Reprinted with permission from ([19]). Copyright (2003) American Chemical Society."

The different transition steps involved during the mesostructure formation are a clear indication of the difficulties and the necessity of carefully controlling the experimental conditions. Indeed, each experimental parameter could induce a unique and decisive effect on the long-range ordering of the mesoporous structure. However, even if the EISA method is performed accurately, the calcination step results to be, as in the other soft template methods, crucial to retain the porous mesostructure during the amorphous-to-crystalline transition.

1.2.2.3 Crystallization of the amorphous framework

Being the loss of the mesostructure during the crystallization step one of the main drawback of the soft template approach, different strategies have been studied during the last decades to resolve this issue. One of the key points to overcome this problem is hidden in the suitable choice of the organic template, which should ensure high thermal stability and a robust scaffold during this crucial step. Conventional surfactants commonly used in the synthesis of mesostructured silica start to decompose at temperature near 200 °C (*e.g.* cetyltrimethylammonium bromide, CTAB) and show low thermal stability resulting unsuitable for the design of mesostructured metal oxides. Among the different classes of organic, block copolymers can be considered the most appropriate.[15] Owing to their mutual repellence between the two or more chemically distinct homopolymer subunits (blocks), they show excellent self-assembly capacity to construct robust mesostructures.[15] At concentrations above CMC, block copolymer molecules should aggregate to minimize their free energy, forming spherical micelles. A progressive increase in concentration leads to the initial formation of hexagonal micelles and liquid crystalline aggregate, such as hexagonal, cubic, or lamellar mesophase (Figure 1.8a).[20] Amphiphilic tri-block copolymers (poly(ethylene oxide)-poly(propylene oxide)-poly(ethylene oxide), PEO-PPO-PEO), commercially known as Pluronics®, are the most common and used block copolymers, but, due to the low thermal stability of the polyester groups, easily decompose at relatively low temperatures (200-350 °C), even in an inert atmosphere.[20] To overcome this drawback, two main solutions have been proposed: the first is based on the use of a Pluronic in the presence of sulphuric acid, that after thermal treatment under inert atmosphere should cause the acid carbonization of the copolymer, leading to the formation of a more stable carbon scaffold (Figure 1.8b).[21] The second solution consists in the use of lab-made block copolymers (*e.g.* poly(ethylene oxide)-polystyrene (PEO-PS) or poly(ethylene oxide)-polyisoprene (PEO-PI)), which show higher thermal stability due to the lower oxygen content and higher carbon content (Figure 1.8c). The utilization of these typologies of block copolymer has allowed the development of a new method called CASH (Combined Assembly by Soft and Hard)[22] based on the transformation of the di-block copolymer, rich in sp^2-hybridized-carbon, in a more stable carbon scaffold through a thermal treatment under inert atmosphere. Both methods guarantee high thermal stability of the scaffold and the preservation of the porous structure even after the complete removal of the carbon by calcination.

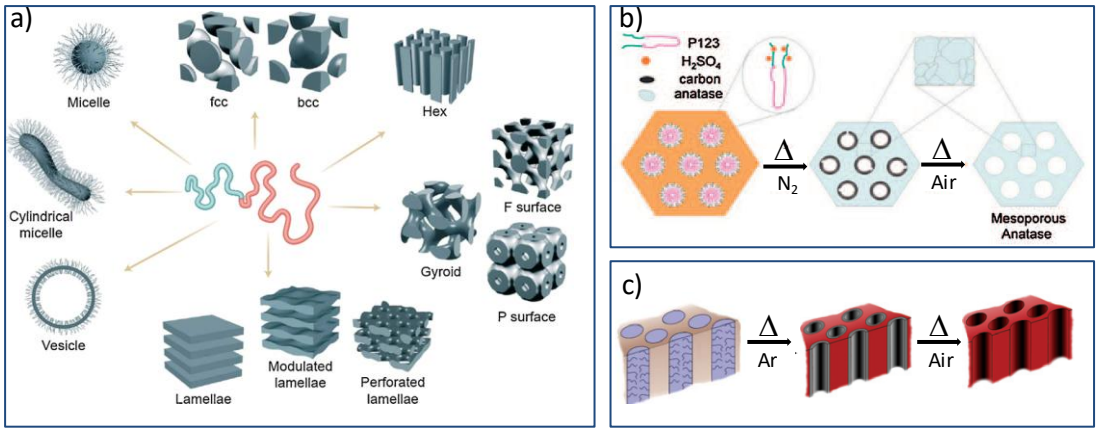

Figure 1.8 (a) Schematic phase diagram of the various morphologies formed by block copolymers, including spherical and cylindrical micelles, vesicles, spheres with face-centered cubic (space group: Fm3m) and body-centered cubic (Im3m) packing, hexagonally packed cylinders (p6m), bicontinuous gyroid (Ia3d), F surface (Fd3m), P surfaces (Pm3n, Pn3m, or Pm3m), and lamella. Adapted with permission from ref. [23]. (b) Schematic illustration of the acid carbonization method. Reproduced with permission from [21]. Copyright 2010 WILEY-VCH. (c) Schematic representation of CASH method. Reprinted by permission from Macmillan Publishers Ltd: [Nature] ([22]), copyright (2010)

1.3 Applications

Mesostructured materials featuring large specific surfaces and easy pore accessibility have found wide applications in heterogeneous catalysis, sorption, separation, gas sensing, optoelectronics, host-guest chemistry, molecular electronic devices and medicine.[24] Up to now, due to the extensive knowledge on silica sol-gel chemistry and surfactant self-assembly, rational design of mesoporous SiO_2-based materials have been successfully realized,[7] and therefore their applications result to be more widespread than those of mesostructured metal oxides. In the following paragraphs, various potential applications of siliceous and non-siliceous metal oxide materials will be described.

1.3.1 Application of siliceous-based materials

Although SiO_2 is an inert material and is not often used as such, its surface is easily activated by the incorporation of active sites or by deposition of active species. The advantage of using ordered mesoporous silica are the relatively large pores which facilitate mass transfer and the very high surface area which allows a high concentration of active sites per mass of material.[25] In the literature, many possible pathways have been proposed to modify mesoporous surface with organic molecules or inorganic active phase, both during the synthesis or post-synthesis.

The functionalisation of mesostructured silica with organic molecules follows three main pathways (Figure 1.9):

- **Grafting or post synthesis functionalisation**: in which the hybrid materials is synthesized through condensation reaction between Si-OH groups of the pore walls and appropriate reagents such as chlorosilanes (*e.g.* $ClSiR_3$), alkoxyorganosilanes (*e.g.* $RSi(OR)_3$), aminorganosilanes ($NH_2RSi(OR)_3$ or silane terminated polymers (polymer-$Si(OR)_3$)
- **Co-condensation or one-pot synthesis**: where a trialkoxyorganosilane ($R'Si(OR)_3$) is added during the synthesis of the mesostructured silica.
- **Periodic mesoporous organosilicas**: when bridged organosilica precursor of the type $(R'O)_3Si\text{-}R\text{-}Si(OR')_3$ is used to lead to a better distribution of the organic motives in the pore walls.

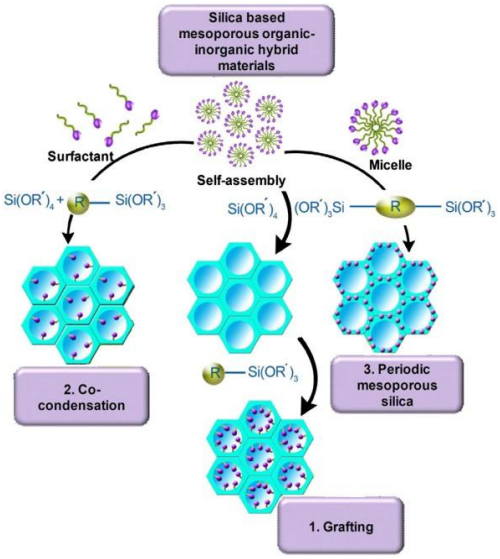

Figure 1.9 Different methods for the synthesis of organic-inorganic hybrid mesoporous silica: 1. Grafting, 2. Co-condensation or *in situ* grafting and 3. Periodic mesoporous silica. Reproduced with permission from [10]. Copyright 2006 WILEY-VCH Verlag GmbH

These materials have found many applications as pollutant sorbents,[26,27] catalysts at low temperatures,[28] and sensors.[29,30] An interesting use of these hybrid organic-inorganic composites has been proposed by Song *et al.*,[31] who impregnated SBA-15 and MCM-41 by using polyethylenimine (PEI) and employed the obtained composites to remove selectively CO_2 or H_2S from a syngas flow, just by changing the adsorption temperature (75 °C in the case of H_2S and 22 °C for CO_2) (Figure 1.10).

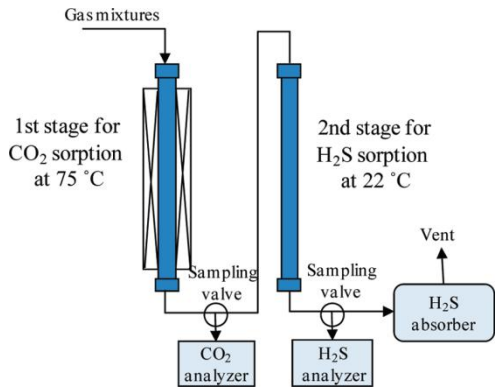

Figure 1.10 Scheme of the experimental two stages process for CO_2 and H_2S removal from a model fuel gas. Reprinted (adapted) with permission from ([31]). Copyright (2009) American Chemical Society

Concerning the functionalisation with inorganic active phases, also in this case one or two steps synthesis routes are possible. In the first case, the metal oxide precursor is directly added during the synthesis of the mesostructured silica while, in the second case, a further step of impregnation with a suitable solution of the metal precursor, has to be performed. However, the integration of a metal oxide precursor during the silica synthesis could cause a loss of order in the porous structure. Hence, the two steps method is preferred.

SiO_2-Me_xO_y composites obtained by impregnation strategies are largely used in different fields as catalysts,[25] sorbents,[32–34] and sensors (Figure 1.11). In the last few years, the design of nano-sized silica particles, showing dimension lower than 100 nm, has opened the way for further applications in biomedical field, especially as drug delivery systems.[35] Up to now, some examples in which SiO_2-based have been employed in the industrial field are already present. For instance, in the Catalin Inc. (Albermarle Catilin) a pilot plant has been developed in which mesostructured silica nanoparticles-based catalysts are employed in an environmentally-friendly process for biodiesel production.[35]

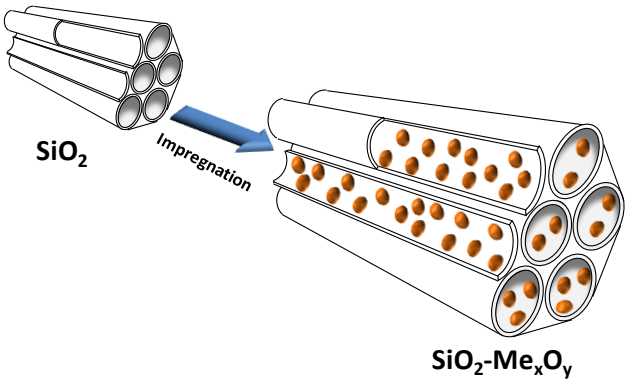

Figure 1.11 Schematic illustration of the synthesis of SiO_2-Me_xO_y by impregnation

1.3.2 Application of non-siliceous materials

Ordered mesoporous metal oxides have attracted considerable interest due to their diverse, and often unique properties, functionalities and potential applications, when compared to their silica counterparts. Even though in the last ten years substantial achievements have been made concerning their synthesis and structural characterization,[12] just in some cases, the application of the mesostructured metal oxides is presented, due to the fact that the main aim in most of the cases is the presentation of the synthetic pathway able to generate the mesostructure. Moreover, in many types of applications, the mesostructure is often lost during the repeated cycles causing a remarkable drop in the initial performances. However, some examples can be reported. Mesostructured SnO_2 materials have been prepared by using both surfactant[36–38] and mesoporous silica[39] as template, and the potential applications as H_2, H_2 and NO_x, CO sensors[36–38] and batteries[39] have also been showed. Nanocasted mesoporous cobalt oxide materials showing high surface areas up to 300 m^2g^{-1} have been used as catalysts,[40] (50 % of their activity was lost after 4 hours use due to the loss of the surface area) and as negative electrodes in rechargeable lithium-ion batteries.[41] Mesoporous zinc oxide with a wurtzite-like nanocrystalline framework has been synthesized by using Schiff-base amine as template.[42] The resulting material shows photoconductivity and photoluminescence at room temperature under visible light irradiation.[42] Nevertheless, due to the unique photocatalytic properties, the availability of its appropriate commercial precursors to generate the mesostructure, as well as its easier handling compared to other metals precursors, mesostructured titanium oxide is the most studied and employed metal oxide. Its applications include photocatalysis, dye-sensitized solar cell, electrochromic and photoelectrochromic devices, chemical energy storage (*e.g.* Li ion batteries[43,44] and supercapacitor[45]), luminescent devices,[45,46] and drug delivery.[47]

References

1 V. Valtchev and L. Tosheva, *Chem. Rev.*, 2013, **113**, 6734–6760.

2 S. Lowell, J. E. Shields, M. A. Thomas and M. Thommes, *Characterization of Porous Solids and Powders: Surface Area, Pore Size and Density*, Springer Netherlands, Dordrecht, 2004, vol. 16.

3 A. Taguchi and F. Schüth, *Microporous Mesoporous Mater.*, 2005, **77**, 1–45.

4 B. Zhou, B. Shi, D. Jin and X. Liu, *Nat. Nanotechnol.*, 2015, **10**, 924–936.

5 F. Di Renzo, H. Cambon and R. Dutartre, *Microporous Mater.*, 1997, **10**, 283–286.

6 J. S. Beck, J. C. Vartuli, W. J. Roth, M. E. Leonowicz, C. T. Kresge, K. D. Schmitt, C. T. W. Chu, D. H. Olson, E. W. Sheppard, S. B. McCullen, J. B. Higgins and J. L. Schlenker, *J. Am. Chem. Soc.*, 1992, **114**, 10834–10843.

7 Y. Wan and Zhao, *Chem. Rev.*, 2007, **107**, 2821–2860.

8 Q. Huo, D. I. Margolese, U. Ciesla, D. G. Demuth, P. Feng, T. E. Gier, P. Sieger, A. Firouzi and B. F. Chmelka, *Chem. Mater.*, 1994, **6**, 1176–1191.

9 B. Samiey, C.-H. Cheng and J. Wu, *Materials (Basel).*, 2014, **7**, 673–726.

10 F. Hoffmann, M. Cornelius, J. Morell and M. Fröba, *Angew. Chemie Int. Ed.*, 2006, **45**, 3216–3251.

11 A. Stein, F. Li and N. R. Denny, *Chem. Mater.*, 2008, **20**, 649–666.

12 D. Gu and F. Schüth, *Chem. Soc. Rev.*, 2014, **43**, 313–344.

13 D. M. Antonelli and J. Y. Ying, *Angew. Chemie Int. Ed. English*, 1995, **34**, 2014–2017.

14 P. D. Yang, D. Y. Zhao, D. I. Margolese, B. F. Chmelka and G. D. Stucky, *Nature*, 1998, **396**, 6–9.

15 J. H. Pan, X. S. Zhao and W. I. Lee, *Chem. Eng. J.*, 2011, **170**, 363–380.

16 Y. Lu, R. Ganguli, C. A. Drewien, M. T. Anderson, C. J. Brinker, W. Gong, Y. Guo, H. Soyez, B. Dunn, M. H. Huang and J. I. Zink, *Nature*, 1997, **389**, 364–368.

17 C. J. Brinker, Y. Lu, A. Sellinger and H. Fan, *Adv. Mater.*, 1999, **11**, 579–585.

18 Z. Miao, H. Zhao, J. Yang and J. Zhao, *New J. Chem.*, 2015, **39**, 1322–1329.

19 E. L. Crepaldi, G. J. d. A. A. Soler-Illia, D. Grosso, F. Cagnol, F. Ribot and C. Sanchez, *J. Am. Chem. Soc.*, 2003, **125**, 9770–9786.

20 D. Grosso, F. Cagnol, G. J. D. A. A. Soler-Illia, E. L. Crepaldi, H. Amenitsch, A. Brunet-Bruneau, A. Bourgeois and C. Sanchez, *Adv. Funct. Mater.*, 2004, **14**, 309–322.

21 R. Zhang, B. Tu and D. Zhao, *Chem. - A Eur. J.*, 2010, **16**, 9977–9981.

22 J. Lee, M. Christopher Orilall, S. C. Warren, M. Kamperman, F. J. DiSalvo and U. Wiesner, *Nat. Mater.*, 2008, **7**, 222–228.

23 D. G. Bucknall, *Science (80-.).*, 2003, **302**, 1904–1905.

24 G. J. D. A. A. Soler-Illia, C. Sanchez, B. Lebeau and J. Patarin, *Chem. Rev.*, 2002, **102**, 4093–4138.

25 A. Taguchi and F. Schüth, *Microporous Mesoporous Mater.*, 2005, **77**, 1–45.

26 R. Sanz, G. Calleja, A. Arencibia and E. S. Sanz-Pérez, *J. Mater. Chem. A*, 2013, **1**, 1956.

27 R. Sanz, G. Calleja, A. Arencibia and E. S. Sanz-Pérez, *Microporous Mesoporous Mater.*, 2012, **158**, 309–317.

28 S.-Y. Chen, C.-Y. Huang, T. Yokoi, C.-Y. Tang, S.-J. Huang, J.-J. Lee, J. C. C. Chan, T. Tatsumi and S. Cheng, *J. Mater. Chem.*, 2012, **22**, 2233–2243.

29 Y. Zhu, H. Li, Q. Zheng, J. Xu and X. Li, *Langmuir*, 2012, **28**, 7843–7850.

30 I. G. Shenderovich, G. Buntkowsky, A. Schreiber, E. Gedat, S. Sharif, J. Albrecht, N. S. Golubev, G. H. Findenegg and H. Limbach, *J. Phys. Chem. B*, 2003, **107**, 11924–11939.

31 X. Ma, X. Wang and C. Song, *J. Am. Chem. Soc.*, 2009, **131**, 5777–5783.

32 C. Cara, E. Rombi, A. Musinu, V. Mameli, A. Ardu, M. Sanna Angotzi, L. Atzori, D. Niznansky, H. L. Xin and C. Cannas, *J. Mater. Chem. A*, 2017, **5**, 21688–21698.

33 M. Mureddu, I. Ferino, A. Musinu, A. Ardu, E. Rombi, M. G. Cutrufello, P. Deiana, M. Fantauzzi and C. Cannas, *J. Mater. Chem. A*, 2014, **2**, 19396–19406.

34 M. Mureddu, I. Ferino, E. Rombi, M. G. Cutrufello, P. Deiana, A. Ardu, A. Musinu, G. Piccaluga and C. Cannas, *Fuel*, 2012, **102**, 691–700.

35 S.-H. Wu, C.-Y. Mou and H.-P. Lin, *Chem. Soc. Rev.*, 2013, **42**, 3862.

36 T. Wagner, C. Kohl, M. Fröba and M. Tiemann, *Sensors*, 2006, **6**, 318–323.

37 T. Hyodo, S. Abe, Y. Shimizu and M. Egashira, *Sensors Actuators B Chem.*, 2003, **93**, 590–600.

38 T. Hyodo, N. Nishida, Y. Shimizu and M. Egashira, *Sensors Actuators B Chem.*, 2002, **83**, 209–215.

39 H. Kim and J. Cho, *J. Mater. Chem.*, 2008, **18**, 771.

40 H. Tüysüz, M. Comotti and F. Schüth, *Chem. Commun.*, 2008, **0**, 4022.

41 K. M. Shaju, F. Jiao, A. Débart and P. G. Bruce, *Phys. Chem. Chem. Phys.*, 2007, **9**, 1837–1842.

42 D. Chandra, S. Mridha, D. Basak and A. Bhaumik, *Chem. Commun.*, 2009, 2384.

43 D. Fattakhova-Rohlfing, M. Wark, T. Brezesinski, B. M. Smarsly and J. Rathouský, *Adv. Funct. Mater.*, 2007, **17**, 123–132.

44 J. M. Szeifert, J. M. Feckl, D. Fattakhova-Rohlfing, Y. Liu, V. Kalousek, J. Rathousky and T. Bein, *J. Am. Chem. Soc.*, 2010, **132**, 12605–12611.

45 T. Brezesinski, J. Wang, J. Polleux, B. Dunn and S. H. Tolbert, *J. Am. Chem. Soc.*, 2009, **131**, 1802–1809.

46 D. Grosso, C. Boissière, B. Smarsly, T. Brezesinski, N. Pinna, P. A. Albouy, H. Amenitsch, M. Antonietti and C. Sanchez, *Nat. Mater.*, 2004, **3**, 787–792.

47 A. A. Ayon, M. Cantu, K. Chava, C. M. Agrawal, M. D. Feldman, D. Johnson, D. Patel, D. Marton and E. Shi, *Biomed. Mater.*, 2006, **1**, L11–L15.

2. Sweetening of syngas

Abstract

In this chapter a brief description of coal, its classification and gasification will be given. Then, the Integrated Gasification Combined Cycles (IGCC) plant will be described, followed by the presentation of the different approaches to remove H_2S from syngas.

2.1 Introduction

Rising world demands for oil and finite petroleum reserve have increased the interest in alternative, secure and affordable fuel sources.[1] In this context, coal is an available and abundant carbon source. Taking into account that the 25% of the global production of NH_3 and the 39% of the methanol are coal-based,[2] the use of coal in our society is still determinant. To be used in these specific fields of the industry application, coal needs to be gasified through a process known as gasification, in which any carbonaceous feedstock is converted into a gaseous product.[2] The as-obtained gas, namely synthesis gas ($CO+H_2$ or syngas), has several applications in the synthesis of chemicals, as methanol and its derivatives (formaldehyde, solvents, methyl *tert*-butyl ether (MTBE), acetyls, dimethyl ether (DME), gasoline via Exxon Mobil MTG and olefins), oxo alcohol, monoethylene glycol (MEG) and synthetic fuel (made by Fischer-Tropsch synthesis). Besides the applications in the chemical industry, coal represents an important global energy source, in particular for power generation: 40% of the electricity produced by fuel derives from coal (data referred to 2014).[*] Nevertheless, coal contributes to more than 70% of CO_2 emission arising from electricity generation and 40% of global anthropomorphic CO_2.[3] To play its role as a sustainable form of energy, its environmental footprint needs to be reduced; a more efficient use of coal may represent an important first step. Besides efficiency improvements, carbon capture and sequestration must be deployed to make achieve a remarkable reduction in CO_2 emission.[4] The most common type of coal-fired power plant is pulverized coal combustion (PCC). The estimated cost of this plant coupled with carbon capture and sequestration is about double the cost of pulverized power production without these processes. Integrated gasification combined cycle (IGCC) coal plant with carbon capture and sequestration (CCS) has attracted a great deal of interest because the cost of power from this plant is only 60% higher than conventional pulverized coal-generated

[*] numerical data presented in aggregated or graphical format: Based on IEA data from [Key World Energy Statistic 2016 IEA database] © OECD/IEA [2016], www.iea.org/statistics, Licence: www.iea.org/t&c.

electricity.[5] The above-described *scenario* makes coal an appealing industrial feedstock and also a convenient energy source, as long as sustainability and efficiency are assured.

A brief overview of coal, its features and uses will be presented in the following section, along with a description of its gasification process.

2.2 Nature of Coal

2.2.1 Geologic origin of coal

The transformation of vegetable matter into coal is known as *coalification*. This process involves biochemical and physiochemical steps. During the biochemical *coalification* anaerobic bacteria initiate and assist the chemical decomposition of vegetal matter and its conversion into peat and brown coal. During the physiochemical step, peat is converted into coal by high pressures and elevate temperatures over millions of years. The physical and chemical structure of coal changes over time: the youngest (least converted) coal is known as *lignite*, which can be further converted to *sub-bitumunous coal*, *bituminous coal*, and finally *anthracite*.[5]

2.2.2 Fixed carbon estimation

Coal is used primarily as a fuel, so its most important property is heat of combustion, which is related to the fixed carbon amount (i.e. fraction of coal that is not moisture, volatiles and ash). This fraction can be estimated by different tests:

- The *high heating value* (HHV) is a calorimetric test: the measurement is carried out by measuring the heat when coal is burned in a constant-volume calorimeter, with an oxygen pressure of 2 to 4 MPa.
- *The proximate analysis,* involving a thermal gravimetric analysis that permits to determine the amount of different species (moisture, volatiles, ash and fixed carbon).
- *The ultimate analysis* describes coal in terms of its elemental composition. For a dried coal, weight percentages of carbon, hydrogen, nitrogen, sulphur, and ash are measured. The remainder of the coal sample is assumed to be oxygen.

2.2.3 Coal rank

Coal rank increases from lignite to anthracite, due to the content of fixed carbon in agreement with the reference values reported in Table 2.1 for each coal typology.

	Fixed carbon limits (dry mineral-matter-free basis), %		Volatile matter limits (dry, mineral-mater-free basic), %	
Rank	Equal or greater than	Less than	Greater than	Equal or less than
Meta-anthracite	98	n/a	n/a	2
Antracite	92	98	2	8
Semi-anthracite	86	92	8	14
Low volatile bituminous coal	78	86	14	22
Medium volatile bituminous coal	69	78	22	31
High volatile A bituminous coal	n/a	69	31	n/a

Table 2.1 Classification of anthracitic and bituminous coals [5]

Since only a small amount of anthracite is available, bituminous and sub-bituminous coals are the primary commercial coals. Lignite is abundant but its transportation costs are economically unsustainable, so most of it is consumed close to the mines. Table 2.2 reports the gross calorific value limits for bituminous, sub-bituminous and lignite.

	Gross calorific value limits (moist, mineral-matter-free basis)			
	Btu/Ib		MJ/Kg	
Rank	Equal or greater than	Less than	Greater than	Equal or less than
High volatile A bituminous coal	14000	n/a	32.557	n/a
High volatile B bituminous coal	13000	14000	30.232	32.557
High volatile C bituminous coal	11500	13000	26.743	30.232
Sub-bituminous A coal	10500	11500	24.418	26.743
Sub-bituminous B coal	9500	10500	22.09	24.418
Sub-bituminous C coal8300	8300	9500	19.30	22.09
Lignite A	6300	8300	14.65	19.30
Lignite B	n/a	6300	n/a	14.65

Table 2.2 Classification of bituminous, sub-bituminous and lignite coal[5]

2.2.4 Coal reserves and resources

In the first half of the twentieth century, coal was the major world energy source, until it was overtaken by oil in the 1960s. Indeed, although coal production has continued to increase over time, it has remained in second place behind oil and just ahead of natural gas. Nevertheless, among the fossil fuels, the global coal reserves[**] are the most abundant. Today, the coal world reserves are estimated to run out within 148 years and the price are expected to gradually increase due to increasing mining costs. However, improvements in mining technology, in IGCC plants efficiency, and also the adoption of *in-situ* coal gasification, may constitute important factors in preserving coal as an advantageous energy source.

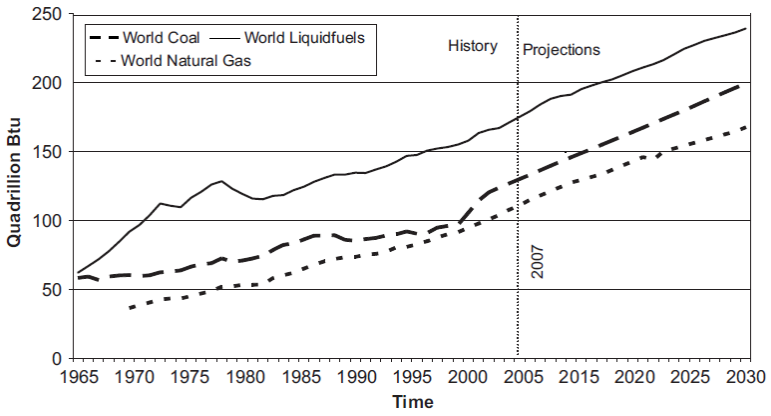

Figure 2.1 Consumption of energy fuel worldwide from1965 to 2030. Reprinted from Publication When will fossil fuel reserves be diminished?, 37 , Shahriar Shafiee, Erkan Topal, Pages 181-189, Copyright (2009),[6] with permission from Elsevier.

2.3 Coal gasification

Gasification is an incomplete combustion of coal or another solid feedstock. The primary goals of gasification are:

- To convert the entire non-ash fraction of the feed to gas
- To produce gasses that preserve, as much as possible, the heat of combustion of the feedstock

Gasses from a gasifier can be burned to produce energy or chemically converted to other products. Typical gasifier feeds are coal, oxygen, and water. The possible reactions involved during this process are described as follows:

[**] The global amount of coal, regardless of the cost or practicality of recovery, are known as *resources*. A more practical measure of the quantities of coal available are known as *reserves*, which is the subset of resources that can be mined at current prices using current technology. For example, there are 275 billion tons of coal reserves in the United States, compared to approximately 4 trillion tons of coal resources.[52]

$2C(s) + O_2(g) \rightarrow 2CO(g)$	$\Delta H^0 = -221.31\ KJ/mol$	*equation 2.1*
$C(s) + O_2(g) \rightarrow CO_2(g)$	$\Delta H^0 = -393.98\ KJ/mol$	*equation 2.2*
$2CO(g) + O_2(g) \rightarrow 2CO_2(g)$	$\Delta H^0 = -566.65\ KJ/mol$	*equation 2.3*
$2H_2(g) + O_2(g) \rightarrow 2H_2O\ (g)$	$\Delta H^0 = -484.23\ KJ/mol$	*equation 2.4*
$2CH_4\ (g) + O_2(g) \rightarrow 2CO(g) + 4H_2(g)$	$\Delta H^0 = -71.44\ KJ/mol$	*equation 2.5*
$C(s) + H_2O(g) \rightarrow CO(g) + H_2\ (g)$	$\Delta H^0 = +131.46\ KJ/mol$	*equation 2.6*
$C(s) + CO_2(g) \rightarrow 2CO(g)$	$\Delta H^0 = +172.67\ KJ/mol$	*equation 2.7*
$C(s) + 2H_2(g) \rightarrow CH_4(g)$	$\Delta H^0 = -74.94\ KJ/mol$	*equation 2.8*
$CO(g) + H_2O(g) \rightleftarrows CO_2\ (g) + H_2$	$\Delta H^0 = -41.21\ KJ/mol$	*equation 2.9*
$CH_4(g) + H_2O(g) \rightleftarrows CO(g) + 3H_2(g)$	$\Delta H^0 = +206.20\ KJ/mol$	*equation 2.10*

The reactions involving complete combustion (*equations 2.2, 2.3 and 2.4*) are the most exothermic and release a great amount of heat, but the produced gasses have no further combustion value. The steam reaction and the CO_2 gasification process (*equation 2.6* and *2.7*, respectively) are endothermic, meaning that the produced gasses have a greater combustion value than the reactants. Therefore, to maximize the combustion value of the syngas, endothermic gas-forming reactions are preferable. These reactions do not occur spontaneously, so exothermic reactions with oxygen increase the mixture temperature to the desired gasification temperature and provide heat for the endothermic gas-forming reactions. Temperature is controlled by varying the oxygen/water balance:

- the reactions with oxygen are all exothermic, so oxygen tends to increase the gasifier temperature;
- the steam gasification reaction (*equation 2.6*) is endothermic, so it tends to reduce the gasifier temperature.

Carbon dioxide can be used instead of steam (*equation 2.7*), but this reaction is slower.

In conclusion, to optimize the gasifier operation, suitable (O_2 +H_2O)/coal and O_2/H_2O ratios have to be set up. However, gasifier configuration, operating conditions and the chosen coal (for further detail see paragraph 2.2.3) are other key parameters to be considered.

2.4 Integrated gasification combined cycle (IGCC)

Integrated Gasification Combined Cycle (IGCC) is a process based on coal gasification technology to produce electricity. A schematic illustration of the IGCC plant is reported in Figure 2.2. Essentially, coal is gasified with air and /or oxygen in a closed pressurised reactor to form a mixture of carbon monoxide and hydrogen (CO + H_2, syngas). Since this process produces other gasses and slag, the resulting syngas is subsequently cooled down to be cleaned and burned with pure oxygen or N_2-enriched air in the turbine, to produce electricity. The residual heat from this process is recovered to produce electricity by steam turbines. However, there are different key points in the process that can affect the efficiency of the whole plant. Such plants use oxygen as oxidant in the gasification. Therefore, they should be equipped with an air separation unit and a significant amount of energy should be provided to carry out cryogen distillation. Furthermore, it would be desirable to clean the raw syngas without cooling. Indeed, purification usually takes place at low temperatures (around 50°C), but other technologies to clean at temperature between 300 °C and 600 °C have been tested in order to increase the overall efficiency.[1] After the cleaning process, CO_2 may also be captured by amine scrubber (methyldiethanolamine, MDEA). However, this process can also affect the whole efficiency of the plant principally due to the high energy consumption during the regeneration of the scrubber.

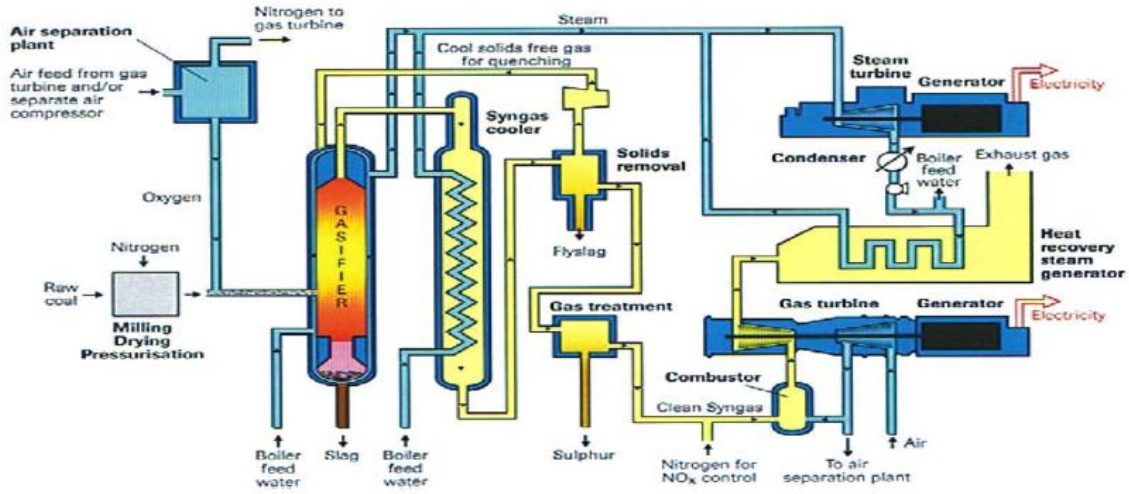

Figure 2.2 Schematic of IGCC showing key system components. Reprinted from Publication Fuel, 84, Andrew J. Minchener Coal gasification for advanced power generation, 2222-2235, Copyright (2005), with permission from Elsevier

The power efficiency of the IGCC plant are affected by several factors:

Coal type: coals are extremely heterogeneous, varying widely in their fixed carbon content and properties from country to country, mine to mine, and even from seam to

seam. The main impurities are ash-forming minerals and sulphur. Higher moisture and ash content of low rank coals require high energy to vaporize moisture and to melt ash.

- **Gasification technology**: gasification technologies including syngas coolers for heat recovery from hot gas, are more efficient than those with a water quench.
- **Degree of air separation unit**: integration of the air separation unit with gas turbine increase the electrical efficiency.
- **Other technologies:** gas turbine technology, inlet turbine temperature and the choice of steam cycle have a significant impact on electrical efficiency.

So far, the power efficiency of IGCC plant has reached a value of almost 40 %.[5] A crucial role in the final energy consumption is related to the syngas cleaning process. Indeed, although the major component of the syngas and the outlet gasifier are CO, H_2, and CO_2 while H_2O, N_2, Ar and small amount of CH_4 may also be present together with other species needed to be removed. This aspect will be discussed in the following paragraph.

2.5 Syngas cleaning processes

A major technical barrier in the use of coal to generate clean energy is represented by the inherent high level of impurities, which make cleaning processes necessary.[4] The main impurities of raw syngas from coal gasification are sulphur species (H_2S, COS), hydrogen chloride (HCl), ammonia (NH_3), hydrogen cyanide (HCN) and volatile species of various trace metals, such as mercury (Hg), arsenic (As), and selenium (Se). At high temperature also alkali can be present. Chlorides, ammonia, and hydrogen cyanide are generally removed in a water wash. Alkali and metal traces can be removed either wet in a scrubber or dry in a particulate filter. These processes are generally integrated into the gasification process. Therefore, residual impurities are represented only by sulphur-containing species and their removal is carried out in a specific unit, according to the requirements of the downstream process.[2]

Coal-derived syngas typically contains 100 - 15 000 ppm of sulphur,[7] and the major part (>90%) is in form of hydrogen sulphide (H_2S) and the rest in form of carbonyl sulphide (COS), while compounds such as SO_x and CS_2 are essentially absent. Being COS not easily removable, a hydrolysis unit is required to convert the COS to H_2S before cleaning processes take place.[4] The U.S. Environmental Protection Agency defines the removal of acid sulfur compounds, primarily H_2S, with the term *sweetening*.[8] The H_2S threshold obtainable after the cleaning process can be quite different depending on the final use: less than 100 ppm are required to make the syngas suitable for IGCC plant,[9] 5-15 ppm is acceptable in natural gas depending on the country, <1

ppm is required for fuel cell applications, where the electrodes are very susceptible to sulphur poisoning. A brief section of the hydrogen sulphide features and different technologies/materials cleaning processes will be described in the next paragraphs.

2.6 Hydrogen sulphide (H_2S)

Hydrogen sulphide (H_2S) is a colourless gas with a characteristic odour of rotten eggs. It is highly toxic, corrosive, and flammable. Since it is heavier than air, it tends to settle in low-lying and poorly ventilated areas. It causes irritation to the eyes, nose, and throat at concentration as low as 5 ppm and is fatal over 1000 ppm. Inhalation is the primary route of exposure. At ~30 ppm, H_2S cripples the sense of smell and is rapidly absorbed into the bloodstream, resulting in poor oxygen uptake at the cellular level.

H_2S occurs naturally, at various concentrations, in different hydrocarbon sources such as crude petroleum, natural gas, and biogas. It is also formed by hydrolysis reactions of metal sulphides in volcanic rocks. Moreover, anaerobic respiration of sulphate-reducing bacteria, *i.e.,* chemosynthetic organisms able to produce energy from sulphate and releasing sulphide as metabolic waste constitutes another major natural source. Landfills, rotten vegetation, and composting sites can also contribute to H_2S generation.

The main anthropogenic source of H_2S is oil refineries. Indeed, sulphur-containing species should be removed from fuels to avoid harmful sulphur oxide emissions (main responsible of acid rains) in the atmosphere when ignited in engines.

2.7 Hydrogen sulphide cleaning processes (*sweetening*)

So far, different technologies of syngas *sweetening* have been proposed. According to Abatzoglou and Boivin's review, they can be divided in two categories: (i) those involving physicochemical phenomena and (ii) those involving biological processes.[10] However, most of the biotechnologies still requires further optimization and scale-up in order to compete with their physical/chemical counterparts. Therefore, the discussion will be focused on the description of the physical-chemical technologies. The abundant literature available on H_2S removal may be broadly classified according to the removal mechanism into four categories: absorption (2.7.1), adsorption (2.7.2), membranes (2.7.3) and cryogenic distillation (2.7.4), as shown in Figure 2.2.

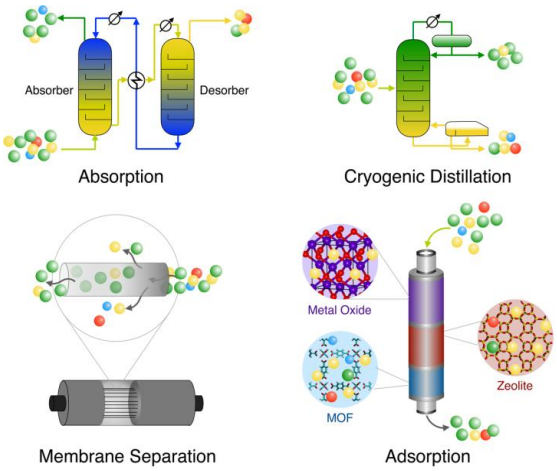

Figure 2.3 Different ways to remove H_2S from syngas. Reprinted with permission from [8]. Copyright (2017) American Chemical Society.

2.7.1 Absorption

Absorption involves physical or chemical *phenomena* in which atoms, molecules or ions enter some bulk liquid or solid material and interact with its volume.[11]

Absorption by solvents for H_2S removal has proven to be the most useful purification technique for nearly 100 years. Depending on the strength of the interaction between the gas molecules and the solvent and the nature of the absorption isotherm, these employed solvents may be broadly classified into chemical and physical. Chemical absorption shows stronger interaction and the isotherm increases sharply at low partial pressure and reaches plateau at higher partial pressure. The plateau is shifted to much higher pressure than in physical absorption, and often there is not a plateau, for the investigated partial pressure range, therefore gas solubility continues to increase with pressure.[8]

Among chemical solvents, alkanolamines are the most widely used. However, when high gas partial pressure is available, physical solvents (methanol, N-methyl-2-pyrrolidone, and Poly(ethylene glycol) Dimethyl Ether) can show high absorption capacity.

2.7.1.1 Alkanolamines

For several years, diethanolamines (DEAs) have been commonly used in refineries to remove acid gases. However, these secondary amines show the main drawback to absorb preferentially CO_2 instead of H_2S. Therefore, tertiary amines such as methyldiethanolamine (MDEA) have been proposed, being able to remove selectively H_2S. Indeed, CO_2 is removed by tertiary amines via bicarbonate formation (*equation 2.11*), which is slower when compared to the CO_2-secondary amine reaction, resulting in a carbamate ion (*equation 2.12*).

$$CO_2 + R_3N + H_2O \rightleftarrows R_3NH^+ + HCO_3^- \qquad \textit{equation 2.11}$$

$$CO_2 + 2R_2NH \leftrightarrows R_2NH_2^+ + R_2COO^- \qquad \textit{equation 2.12}$$

The H_2S-tertiary amine reaction, as well as all other amines, involves a proton transfer (*equation 2.13*) and result to be faster than the CO_2-tertiary amine reaction.[12]

$$H_2S + R_3N \rightleftarrows R_3NH^+ + HS^- \qquad \textit{equation 2.13}$$

Therefore, MDEAs are applied as low-temperature H_2S removers in IGCC plants.[8,13]

2.7.1.2 Methanol (Rectisol process)

The Rectisol process, developed independently by Linde and Lurgi in the late 1950s, involves physical absorption using methanol at temperature between -40 and -60 °C. Since methanol has a low viscosity, it can be used in very-low-temperature absorption processes, in particular for feeds with low partial pressures of acid gases. Since the high vapor pressure of methanol required to wash all streams with water to recover methanol vapors, all streams are humidified during the process.[14]

2.7.1.3 N-methyl-2-pyrrolidone (Plurisol process)

Plurisol process based on N-methyl-2-pyrrolidone (NMP) permits to overcome the limit of Rectisol, being performed at higher temperature (near ambient temperature) without excessive solvent loss, due to its much lower pressure.[14]

2.7.1.4 Poly(ethylene glycol) Dimethyl Ether (Selexol process)

The Selexol process, based on the use of poly(ethylene glycol) dimethyl ether (PEGDME, mixture of $CH_3O(CH_2CH_2O)_nCH_3$ oligomers with n=2-9), developed by allied Chemical Corporation, was first applied in 1970. Compared to the other solvents, PEGDME has a higher viscosity, which reduces mass-transfer rates, especially at low temperature.[8]

2.7.1.5 Ionic liquids

Ionic liquids (ILs) are salts having moderately low melting points (<100°C). Their ionic character is responsible for a large cohesive energy in the liquid phase, leading to extremely low vapor pressure over a wide temperature range. Due to their polar character, ionic liquids show a high affinity for polar molecules such as H_2O and H_2S, while non polar molecules like CH_4 and other alkanes exhibit a much smaller solubility. Jou and Mather first investigated H_2S absorption in an ionic liquid (1-N-butyl-3-methylimidazolium hexafluorophospate, [$bmim^+$]-[PF_6^-]), and observed that H_2S was physisorbed.[15] However, Pomelli *et al.*[16] extended this investigation to a wider range of cations and anions and demonstrated an extremely high interaction between

ILs and H_2S, and hypothesize hydrogen bond formation between H_2S and ILs. The H_2S solubility is affected by both cation and anion species, and therefore it is not ~~be~~ possible to predict their removal efficiency without trying all the possible pairs.[8]

2.7.2 Adsorption

According to IUPAC, adsorption is defined as the increase of the concentration of a dissolved substrate at the interface of a condensed and a liquid phase due to the operation of surface forces.[17]

In syngas *sweetening*, a selective and high-capacity solid substrate can be used to preferentially remove H_2S by *physisorption* or *chemisorption*, depending on the strength of sorbate-sorbent interaction. These adsorbents, known also as sorbents, can be classified as metal oxides, metal organic frameworks (MOFs), zeolites, carbons, and composite materials. For any adsorption application, it is desirable that the adsorbent shows:

- high separation selectivity for the target molecule;
- high capacity for the adsorbate;
- stability under extreme acid gas environments;
- structural regenerability and long lifetime.

2.7.2.1 Metal oxide

Since 1960s, metal oxides have been used for desulphidation of syngas. Several theoretical studies have pointed out the potential suitability of different metal oxides as H_2S removal candidates at mid-high temperature (400-1200 °C).[18,19] Different experimental have confirmed this finding for a wide range of temperatures.[1,19,20] Among these oxide, zinc oxide results to be the most employed. Indeed, Zn-oxide sorbents are commercially available and a full-scale testing has been performed at the Puertollano IGCC plant in Spain.[21] However, due to the high volatility of zinc oxide and the low kinetic of the reaction with H_2S, research is moving towards valid alternatives. More details about this issue will be provided in the next chapter (Chapter 3).

2.7.2.2 Metal-organic frameworks (MOFs)

Metal organic frameworks MOFs are porous structures resulting from coordination of metal ions or clusters to organic ligands. The main advantages of their use are related to (i) the maximization of the number of metal centers available to interact with the adsorbate molecules and (ii) the use of appropriately functionalized organic ligands which can contribute to the selectivity towards the desired gas molecule. However, the weak coordination bonds

between the metals and the organic ligands make the MOF structure very susceptible to hydrolysis and thermally instable.

2.7.2.3 Zeolites

Zeolites are crystalline porous aluminosilicates consisting of a three-dimensional framework of SiO_4 and AlO_4 tetrahedra. Their pores are defined by the crystal structure and have precise sizes and shapes, that fall in the microporous range. Maghsoudi *et al.* found high H_2S capacity at 25°C and 2 bar in an all-silica zeolite, suggesting this material a promising remover.[22] Aluminosilicate zeolites, which can accommodate a variety of cations such as Na^+, K^+, Ca^{2+}, may provide stronger selectivity.[8] Adsorption mechanism of H_2S in cation exchanged zeolites has been extensively studied by FT-IR, UV/vis and NMR spectroscopy on different typologies of alluminosilicate zeolite. It was found that when the Si/Al ratio is almost 2.5, the first H_2S molecules were adsorbed dissociatively, while when Si/Al > 2.5, adsorbtion of H_2S molecules occurs without dissociation.[23]

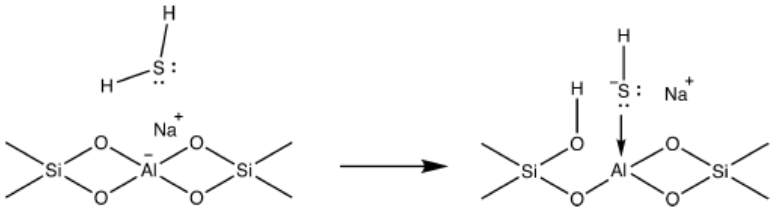

Figure 2.4 Schematic representation of dissociative H2S adsorption on an aluminosilicate zeolite. Reprinted with permission from [8]. Copyright (2017) American Chemical Society.

2.7.2.4 Activated Carbons

Activated carbon, usually with surface areas higher than 1000 m^2g^{-1} due to a high degree of microporosity, is a well-known material for adsorption in catalysis. Different strategies have been implemented to increase surface areas, pore volume, and to change the surface acidity of the activated carbon, increasing H_2S-removal permormances.[24–26] In different cases, impregnation pathways, performed to give a basic character to the sorbent, caused a worsening in H_2S-adsorption capabilities due to pores blocking phenomena. A 10% decrease of the H_2S retention capacity was detected on activated carbon impregnated with urea, probably due to an 18% decrease in the surface area.[27] Moreover, poor H_2S removal capacities were observed by loading 3-aminopropyltriethoxysiliane (APTES).[28]

2.7.2.5 Structured carbon

Structured nanoporous carbon materials may be broadly classified into two main groups: graphene-based materials and carbon nanotubes. Several groups have theoretically investigated H_2S adsorption on graphene surface, mainly for sensor application.[29–31] Strong

adsorption was found in the case of Pt-doped graphene due to a large H_2S-Pt binding energy.[32] Adsorption experiments on carbon nanotubes decorated with tungsten nanoparticles or amino-functionalized were carried out on by Mohamadalizadeh and co-workers.[33] The performances of these materials were comparable with those of activated carbon, and better regenerability was found in the case of carbon nanotubes.

2.7.2.6 Composites

Multicomponents material in the form of composites may be used to combine the textural properties of a support and the H_2S removal capacity of an active phase. Order mesoporous silica, showing high surface area and pore volume, has opened a new area for novel heterogeneous catalysts. Indeed, the presence of larger pore size, when compared to their microporous counterparts, allow their functionalization with different active phases. In the following paragraphs, two main examples of these composites will be presented.

2.7.2.6.1 Supported metal oxide on mesoporous silica

As already discussed, metal oxide sorbents show high affinity for H_2S but suffer drops in surface area and porosity values over different sulphidation and regeneration cycles, leading to a worsening in therms of performance. Moreover, nanoparticles tend generally to sinter forming larger crystallites during the process of high-temperature regerenation. Therefore, their dispersion on a suitable silica matrix can be in principle a way to prevent this *phenomena*, thus assuring high performances over several sulphidation and regeneration cycles. Wang *et al.*[34] investigated for the first time the adsorption of H_2S on metal-oxide-impregnated mesoporous silica, (ZnO/SBA-15 and Fe_2O_3/SBA-15) at room temperature. Dhage *et al.*[35] highlighted an effective improvement of the performances of ZnO/SiO_2 composites with respect to the unsupported commercial (BASF and Sub-Chemie) counterpart. Moreover, the use of dopants such as Mn, Fe, Co, Ni, and Cu allow to further optimize ZnO sorbents, with the most remarkable effect from copper. Mureddu *et al.* proved that ZnO/SBA-15[36] and Fe_2O_3/SBA-15[37] sorbents show better performances when compared to commercial unsupported ZnO sorbents at mid-temperatures, even over repeated sulphidation regeneration cycles.

2.7.2.6.2 Supported amines on mesoporous silica

Supported amine adsorbent can be used instead of the conventional amine solution to avoid corrosion phenomena and the loss of the amine solution during the regeneration.[38] In this context, different composites have been developed, using different amines / imines and silica supports.[39–42] The most promising system have been proposed by Song *et al.*[13]: a

polyethylenimine (PEI)/SBA-15 sorbent able to absorb preferentially CO_2 or H_2S just changing the operating temperature.

2.7.3 Membrane separation

Membrane technologies represent an alternative way to remove impurities including water, carbon dioxide, nitrogen, hydrogen sulphide, and other hydrocarbon from syngas.[43] There are different typologies of membranes, and in this section a brief description will be given.

2.7.3.1 Polymeric membrane

Polymer membranes for H_2S removal have been investigated since the 1950s. To maximize the membrane area per unit volume, two main configurations are widely used: hollow fibers and flat sheets in the form of spiral-wound modules.[8] An important feature to be considered is the glass transition temperature (Tg), which determines the state of the polymer membrane as hard and relatively brittle "glassy" amorphous (< Tg) or soft and viscous "rubber" (>Tg). Glassy polymers offer size-selective separation by virtue of differential diffusivity, while rubbery polymers suffer reduced size selectivity because of increased elasticity of the polymer chains, and its selectivity is governed by the relative gas solubilities. As in the case of alkanolamines, there is a need for membranes with high H_2S selectivity with respect to CO_2. Although both glassy and rubbery polymers can separate CO_2 and H_2S, in practice the former is more suitable for CO_2 whereas the latter is more suitable for H_2S, which is larger and more condensable gas than CO_2.[8]

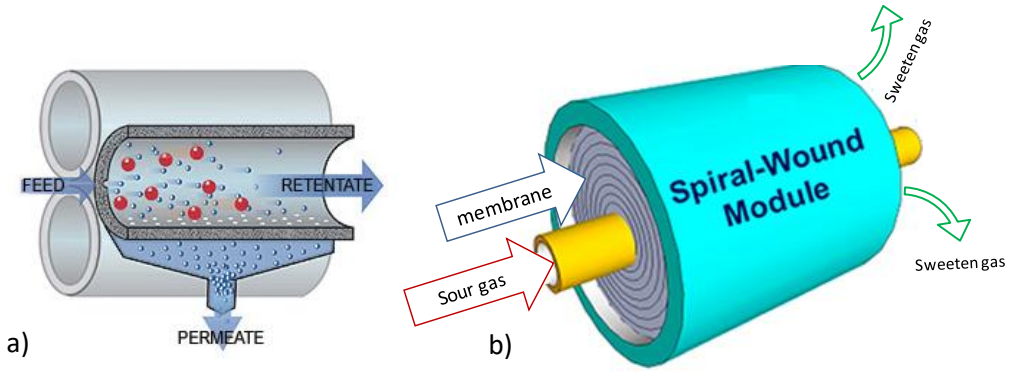

Figure 2.5 Representation of hollow fiber (a) and spiral wound modules membranes (b)

2.7.3.2 Membranes for gas-liquid contact

Integrated systems, in which a membrane features high surface area and microporosity is coupled with a suitable solvent, may be suitably used as membranes for gas-liquid contact. These technologies combine the advantages of high surface area per unit volume of membrane contactors with the selective absorption of a solution (for instance amine solution).

The gas-liquid interfaces may be achieved by flowing a gas on the outside of a membrane and with liquid flowing within its lumen. These gas-liquid membranes offer several advantages over conventional contacting devices, such as high surface area per unit contactor volume, independent control of gas and liquid flows, small size, known gas-liquid interfacial area, modularity and easiness to be scaled up.[44] Hollow-fiber membrane contactors have shown promising H_2S selectivity.[8]

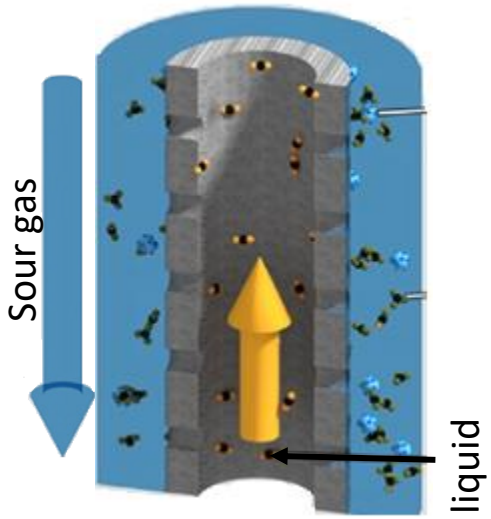

Figure 2.6 Illustration of membrane for gas liquid contact[45]

2.7.4 Cryogenic distillation

Distillation is a very energy-consuming process which requires boiling and condensing of the entire feed stream. However, in the case of very sour gasses, its use can be advantageous in comparison with common scrubbers. Total Institut Français du Petrole, have developed a cryogenic process namely SPREX (Special PRe-EXtraction) aimed to remove H_2S from very sour gasses.[46] This cryogenic treatment reduces the H_2S content in the gas, but a further amine sweetening step is required to lower H_2S content to acceptable values.

The following Table 2.3 summarize the main operatives features, drawbacks and advantages of the most common H_2S removal technologies.

System	Operating temperature (°C)	Regeneration process	Drawbacks	Advantages
Alkanolamines	25 < T < 100[12]	heating <100 °C [12]	- low operating temperature - degradation of the amine[12]	high efficiency low cost[12]
Rectisol process	-40 < T < -60[8]	lower the pressure [14]	very low operating temperature[8]	- low cost of the methanol - low degradation due to the physical absorption[8]
Plurisol process	35[14]	lower the pressure[14]	low operating temperature[14]	- high absorptive capacity[14]
Selexol process	~low temperature(<100 °C)[47]	heating at 150 °C[47]	low operating temperature	- high absorptive capacity[8]
Ionic liquids	<200°C[48]	heating[49] or bubbling air[48]	-low operating temperature - relative high cost of ILs	- high absorptive capacity, [48] - high regenerability[48]
Metal oxide	25-1200[1]	heating[1]	low regenerability[8]	low cost - wide operating temperature - high adsorptive capacity[1]
MOF	<200 °C	heating	low thermal stability[8]	high adsorptive capacity[8]
Zeolites	low-mid temperature (25-600 °C) [50]	heating[50]	plugging phenomena[1]	- high thermal stability - good regenerability[50]
Activated Carbons	low-mid temperature (25-300 °C)[8]	heating[51]	plugging phenomena[1]	low cost[51]
Supported metal oxide on mesoporous silica	25-700	heating[8]	low ratio active phase/mass sorbent[8]	- high regenerability - low cost[8] - wide range operating temperature[8] - wide choice of active phase[8]
Supported amines on mesoporous silica	<100[13]	heating[13]	low operating temperature	easy to adle
Membrane separation	low temperature (25-300 °C) [8]	heating or lowering pressure[8]	low selectivity toward H_2S separation[8]	easily to scale up[8]
Cryogenic distillation	-35/-65[8]	-	High-energy consuming process[8]	useful with very sour syngas[8]

Table 2.3 The main operatives features, drawbacks and advantages of the most common H_2S removal technologies

References

1 S. Cheah, D. L. Carpenter and K. A. Magrini-Bair, *Energy and Fuels*, 2009, **23**, 5291–5307.

2 C. Higman and S. Tam, *Chem. Rev.*, 2014, **114**, 1673–1708.

3 K. Burnard and S. Bhattacharya, *POWER GENERATION FROM COAL Ongoing Developments and Outlook*, 2011.

4 H. Yang, H. Ye, S. Zhai and G. Wang, *2011 Int. Symp. Adv. Control Ind. Process.*, 2011, 258–261.

5 D. A. Bell, B. F. Towler and M. Fan, in *Coal Gasification and Its Applications*, Elsevier, 2011, pp. 1–15.

6 S. Shafiee and E. Topal, *Energy Policy*, 2009, **37**, 181–189.

7 J. P. Wakker, A. W. Gerritsen and J. A. Moulijn, *Ind. Eng. Chem. Res.*, 1993, **32**, 139–149.

8 M. S. Shah, M. Tsapatsis and J. I. Siepmann, *Chem. Rev.*, 2017, **117**, 9755–9803.

9 Z. F. Zhang, B. S. Liu, F. Wang, W. S. Wang, C. Xia, S. Zheng and R. Amin, *Appl. Surf. Sci.*, 2014, **313**, 961–969.

10 N. Abatzoglou and S. Boivin, *Biofuels, Bioprod. Biorefining*, 2009, **3**, 42–71.

11 John E. McMurry, *Fundamentals of Organic Chemistry*, Brooks/Cole, 2002.

12 Y. A. Anufrikov, G. L. Kuranov and N. A. Smirnova, *Russ. J. Appl. Chem.*, 2007, **80**, 515–527.

13 X. Ma, X. Wang and C. Song, *J. Am. Chem. Soc.*, 2009, **131**, 5777–5783.

14 G. Hochgesand, *Ind. Eng. Chem.*, 1970, **62**, 37–43.

15 F.-Y. Jou and A. E. Mather, *Int. J. Thermophys.*, 2007, **28**, 490–495.

16 C. S. Pomelli, C. Chiappe, A. Vidis, G. Laurenczy and P. J. Dyson, *J. Phys. Chem. B*, 2007, **111**, 13014–13019.

17 in *IUPAC Compendium of Chemical Terminology*, IUPAC, Research Triagle Park, NC, 1990, p. 85.

18 P. R. Westmoreland and D. P. Harrison, *Environ. Sci.*, 1976, **10**, 659–661.

19 W. F. Elseviers and H. Verelst, 1999, **78**, 601–612.

20 J. Skrzypski, I. Bezverkhyy, O. Heintz and J. Bellat, *Ind. Eng. Chem. Res.*, 2011, **50**, 5714–

5722.

21 M. D. Dolan, A. Y. Ilyushechkin, K. G. McLennan and S. D. Sharma, *Asia-Pacific J. Chem. Eng.*, 2012, **7**, 1–13.

22 H. Maghsoudi, M. Soltanieh, H. Bozorgzadeh and A. Mohamadalizadeh, *Adsorption*, 2013, **19**, 1045–1053.

23 M. S. Shah, M. Tsapatsis and J. I. Siepmann, *Chem. Rev.*, 2017, **117**, 9755–9803.

24 F. Adib, A. Bagreev and T. J. Bandosz, *J. Colloid Interface Sci.*, 1999, **214**, 407–415.

25 A. Bagreev, F. Adib and T. J. Bandosz, *J. Colloid Interface Sci.*, 1999, **219**, 327–332.

26 T. J. Bandosz, *Carbon N. Y.*, 1999, **37**, 483–491.

27 F. Adib, A. Bagreev and T. J. Bandosz, *Langmuir*, 2000, **16**, 1980–1986.

28 S. Tian, H. Mo, R. Zhang, P. Ning and T. Zhou, *Adsorption*, 2009, **15**, 477–488.

29 Y.-H. Zhang, L.-F. Han, Y.-H. Xiao, D.-Z. Jia, Z.-H. Guo and F. Li, *Comput. Mater. Sci.*, 2013, **69**, 222–228.

30 J. E. Castellanos Águila, H. H. Cocoletzi and G. H. Cocoletzi, *AIP Adv.*, 2013, **3**, 32118.

31 D. Borisova, V. Antonov and A. Proykova, *Int. J. Quantum Chem.*, 2013, **113**, 786–791.

32 M. D. Ganji, N. Sharifi, M. Ardjmand and M. G. Ahangari, *Appl. Surf. Sci.*, 2012, **261**, 697–704.

33 A. Mohamadalizadeh, J. Towfighi, A. Rashidi, A. Mohajeri and M. Golkar, *Ind. Eng. Chem. Res.*, 2011, **50**, 8050–8057.

34 X. Wang, T. Sun, J. Yang, L. Zhao and J. Jia, *Chem. Eng. J.*, 2008, **142**, 48–55.

35 P. Dhage, A. Samokhvalov, D. Repala, E. C. Duin, M. Bowman and B. J. Tatarchuk, *Ind. Eng. Chem. Res.*, 2010, **49**, 8388–8396.

36 M. Mureddu, I. Ferino, E. Rombi, M. G. Cutrufello, P. Deiana, A. Ardu, A. Musinu, G. Piccaluga and C. Cannas, *Fuel*, 2012, **102**, 691–700.

37 M. Mureddu, I. Ferino, A. Musinu, A. Ardu, E. Rombi, M. G. Cutrufello, P. Deiana, M. Fantauzzi and C. Cannas, *J. Mater. Chem. A*, 2014, **2**, 19396–19406.

38 X. Wang, X. Ma, L. Sun and C. Song, *Green Chem.*, 2007, **9**, 695.

39 H. Y. Huang, R. T. Yang, D. Chinn and C. L. Munson, *Ind. Eng. Chem. Res.*, 2003, **42**, 2427–2433.

40 X. Chu, Z. Cheng, Y. Zhao, J. Xu, H. Zhong, W. Zhang, J. Lü, S. Zhou, F. Zhu, Y. Zhou and L. Zhou, *Ind. Eng. Chem. Res.*, 2012, **51**, 4407–4413.

41 Q. Xue and Y. Liu, *J. Ind. Eng. Chem.*, 2012, **18**, 169–173.

42 X. Xu, I. Novochinskii and C. Song, *Energy & Fuels*, 2005, **19**, 2214–2215.

43 P. Pullumbi, in *Membrane Reactor Engineering*, John Wiley & Sons, Ltd, Chichester, UK, 2016, pp. 256–279.

44 A. Mansourizadeh and A. F. Ismail, *J. Hazard. Mater.*, 2009, **171**, 38–53.

45 J. Hou, M. Y. Zulkifli, M. Mohammad, Y. Zhang, A. Razmjou and V. Chen, *J. Memb. Sci.*, 2016, **520**, 303–313.

46 F. Lallemand, F. Lecomte and C. Streicher, in *International Petroleum Technology Conference*, International Petroleum Technology Conference, 2005.

47 R. Anantharaman, O. Bolland, N. Booth, E. van Dorst, C. Ekstrom, E. Sanchez Fernandes, F. Franco, E. Machhi, G. Manzolini, D. Nikolic, A. Pfeffer, M. Prins, S. Rezvani and L. Robinson, 2011, 1–112.

48 Y. Ma, X. Liu and R. Wang, *J. Hazard. Mater.*, 2017, **331**, 109–116.

49 K. Huang, X.-M. Zhang, L.-S. Zhou, D.-J. Tao and J.-P. Fan, *Chem. Eng. Sci.*, 2017, **173**, 253–263.

50 M. Ozekmekci, G. Salkic and M. F. Fellah, *Fuel Process. Technol.*, 2015, **139**, 49–60.

51 C. Weinlaender, R. Neubauer, M. Hauth and C. Hochenauer, *Chemie-Ingenieur-Technik*, 2017, **89**, 1247–1254.

52 G. D. Croft and T. W. Patzek, *Nat. Resour. Res.*, 2009, **18**, 173–180.

3. Design of sorbents for H_2S removal at mid-temperature

Abstract

In this chapter the advantages of the sweetening processes at mid-temperature are described and successively the attention will be focused on the design of suitable H_2S sorbents for this range of temperatures (300-600 °C).

3.1 Mid-temperature desulphidation

Amine scrubbing is the dominant technology currently used in industry for removing CO_2 and H_2S from various gas streams, as the amine solutions have a high capacity and selectivity for removing acidic gases. However, there are some drawbacks in this process:[1]

- high energy consumption deriving from cooling and reheating cycles due to the low removal temperature (more details in Chapter 2, paragraph 4.4.1.1.);
- low absorption/desorption rate, resulting in a larger size scrubber for increasing the gas-liquid interface;
- degradation and evaporation of the amine during in the whole process;
- material corrosion of the scrubber due to the liquid amine solution;
- difficulty in removing sulphur to the level required for the fuel cell application (< 5 ppm).

If the solvent degradation, evaporation and corrosion issues can be potentially overcome using hybrid organic-inorganic composites as amine anchored on silica matrix, the main problem related to the low operating temperature, that inevitably affects of few percent the whole energy efficiency of the IGCC plant, cannot be solved.[2] A brief review of the removal methods proposed in the previous chapter, highlights as all the absorption sweetening methods need to be performed at low-temperature. Theoretically, the heat energy can be partially recovered using heat exchange equipment, but tar formed on the surface of the reactor and the pipes during the condensation could render the heat recovery challenging.[3] Therefore, mid- (300-600 °C) and high-temperature (600-850 °C) syngas sweetening processes offer potential economic advantages by allowing gasification, gas clean-up, and downstream processes at similar temperatures.[3]

Keeping out metal organic framework (MOF), which has showed low thermal stability, metal oxide, zeolite, activated-carbon and metal oxide composites can be potential candidates as removers for mid- and hot-gas sweetening processes. However, different typologies of non-reactive H_2S adsorbents such as activated-carbon and modified activated-carbon suffer from low sulphur uptake capacity,[4] whereas the main drawback of the zeolites is represented by plugging *phenomena*, due to the small pores dimension, leading to short lifetime of the corresponding sorbents. Therefore, the better perspectives are offered by **metal oxides** and **metal oxide composites**. In this context, since the 1960s, metal oxides MeO (Me = Zn, Cu, Fe, Ca, Mn, etc.)[5–7] have been proposed and extensively investigated as hot-gas desulphurization removers.[7,8] However, some technical disadvantages are particularly critical when the sulphidation is performed at high-temperature: (i) the limited sorbent lifetime due to its thermal instability, which could causes sintering in pure metal oxide or porous structure collapse in composites,[9] and/or volatilization of metals (as in the case of the Zn[10]) under high temperature and strong reducing atmosphere, and (ii) the difficulty to collect and filter liquid alkali (commonly used as gasification catalyst,[11] during the pre-treatment before the sulphidation of the raw syngas).[3] These drawbacks can be partially overcome by operating at mid-temperatures (300-600 °C), in which the increase of the sorbent's lifetime as well as the easy recovery of the alkali powders by filtration are expected.[5] Moreover, according to the RTI international, the thermal efficiency* of a 600 MW IGCC plant could increase of 3.6 points if the desulphidation is performed in the mid-temperature range rather than by conventional Selexol technology. [3,12]

In the next paragraph the main features of potential sorbents useable in this range of temperature (metal oxide and metal oxide composites) will be discussed.

3.2 Requirements of the sorbent for mid-temperature

The general requirements needed to be considered for a **sorbent** potentially suitable for H_2S cleaning process at mid-temperature, can be summarized in the following points:

- Large selectivity toward H_2S deriving from thermodynamics and kinetics;
- High adsorption capacity to reduce both sorbent quantity and process equipment size;
- Easy regenerability;
- Good mechanical strength and thermal stability;

* Thermal efficiency is defined as the ratio between the net work done and the heat content of the fuel.

- Steady performance for high numbers of cycles (to increase the lifetime of the sorbent)
- Chemical stability in the typical reducing environment of syngas;
- Low-cost raw material;
- Low toxicity.

Moreover, **process requirements** have to be taken into consideration for the suitability of metal oxide for H_2S removal at mid-temperature:

- high sulphidation rate and stability of the metal sulphide under reduction condition;
- minimization of side reactions under reduction condition during the sulphidation runs (e.g. formation of metal carbides, reduction to zero-oxidation state etc.);
- high regeneration rate and production of SO_2 or elemental sulphur under oxidizing gas condition;
- minimization of sides reactions under oxidizing gas (e.g. sulphates) and hydrothermal stability during regeneration.

3.3 H_2S removal by metal oxides phase

3.3.1 Sulphur reaction of metal oxide

Metal oxide (MeO) based sorbent reacts with H_2S, according to the general reaction:

$$MeO_{(s)} + H_2S_{(g)} \rightleftarrows MeS_{(s)} + H_2O_{(g)} \qquad \textit{equation 3.1}$$

The regeneration, usually performed under air flow, is represented by the overall equation:

$$MeS_{(s)} + \tfrac{3}{2}O_{2(g)} \rightleftarrows MeO_{(s)} + SO_{2(g)} \qquad \textit{equation 3.2}$$

The regeneration reaction equilibrium strongly depends on the oxygen partial pressure. An unwanted side-reaction is the formation of sulphates:

$$MeS_{(s)} + 2O_{2(g)} \rightleftarrows MeSO_{4(s)} \qquad \textit{equation 3.3}$$

Being sulphates inert toward H_2S, the direct consequence is a worsening of sorbent performances.[2] The pioneering work of Westmoreland,[7] based on a thermodynamic study opened the road to several metal oxide candidates. Beyond the thermodynamics, kinetics of the H_2S and metal oxide reaction represents another crucial point on the final performances of the metal oxide. Several studies indicate that the intrinsic reaction kinetics of the sulphidation of ZnO, MnO, CaO, Fe_2O_3 is of the first order with respect to H_2S concentration.[3] Rodriguez *et*

al.[13,14] studied adsorption of H_2S on a series of metal surfaces (Al_2O_3, MgO, α-Cr_2O_3 (0001), ZnO, Cu_2O,and Cr_3O_4(111)) using synchrotron-based high resolution photoemission. It was observed that the reactivity of H_2S molecules is inversely correlated to the band gap of the metal oxide (Figure 3.1). According with these results, α-Cr_2O_3, showing the smallest band gap, interacts more strongly with H_2S. This fact was already known for some catalysists for Superclaus process[15] based on α-allumina-supported iron and chromium oxide. However, due to the severe toxicity of chromia, continuing research to develop new materials for these important reactions is underway.[16]

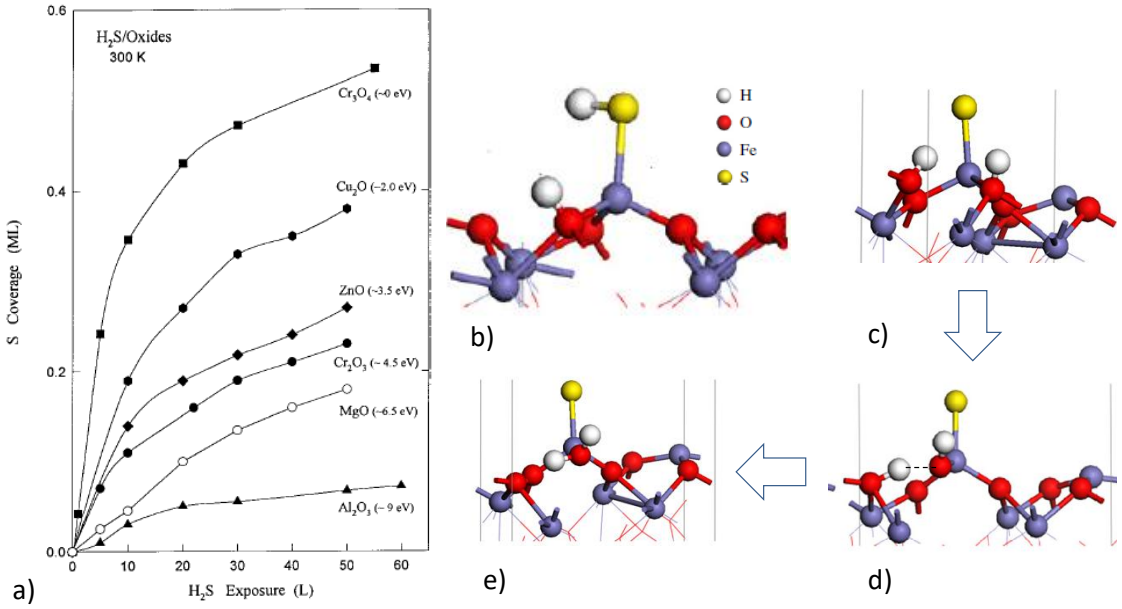

Figure 3.1 (a) Total coverage of sulphur (HS+S) as a function of H_2S exposure to a series of oxides (Al_2O_3, MgO, Cr_2O_3, ZnO, Cu_2O, Cr_3O_4) at 300 k. The numbers in parentheses denote the band gap of each oxide. Reprinted (adapted) with permission from ([17]). Copyright (2000) American Chemical Society. (b) Representation of dissociative adsorption of H_2S to SH ad S on α-Fe_2O_3 (0001) surface. (c, d, e) Representation of the possible mechanism leading to the H_2O formation in α-Fe_2O_3 (0001) surface. (b-e) Adapted from "A density functional theory study on the interaction mechanism between H_2S and the α-Fe2O3(0001) surface", 115, Jiajia Song, Xiaoqi Niu, Lixia Ling,Baojun Wang, 26-33, Copyright (2013), with permission from Elsevier([18])

Moreover, several DFT studies on H_2S reaction with Zn,[19] Fe,[18] and Cu[20] provide interesting details on dissociation mechanism in the H_2S adsorption (Figure 3.1b).

3.3.2 Non catalytic gas-solid reaction models.

The reaction between H_2S and a metal oxide belongs to the class of non-catalytic gas-solid reactions. These reactions have been most commonly theorized using either the unreacted shrinking core model (USCM) or the grain model. USCM assumes that the reaction of a pellet is much faster than diffusion and hence occurs at the solid reactant surface, leading to an unreacted core.

The model permit to correlate the necessary time (t) to reach a given conversion (X) of a solid:

$$t = \tau_{DP}[1 - 3\left(1 - X\right)^{2/3} + 2\,(1 - X)\Big] + \tau_{MT}[X] + \tau_{R,SC}[1 - (1 - X)^{1/3}] \qquad \textit{equation 3.4}$$

Where τ_{DP} is the characteristic time for diffusion through the pellet's product layer, τ_{MT} is the characteristic time for external mass transfer from the bulk gas to the surface of the pellet (film diffusion), and $\tau_{R,\,SC}$ is the characteristic time for chemical reaction at the interface between the unreacted core of the pellet and the reacted product layer, (see Figure 3.2a) and X is the conversion of the pellet, defined as:

$$X = 1 - (\frac{R_c}{R})^3 \qquad \textit{equation 3.5}$$

where R_c is the radius of the core and R is the radius of the pellet (Figure 3.2a).

In the grain model it is assumed that the pellet structure is made of very small spherical grain, and each grain reacts independently according to USCM. If the diffusivity of the gaseous reactants in the core of the pellet is comparable to that in the completely (or partially) reacted grain at the surface of the pellet, then the gases can reach the center of the pellet even if only a thin layer of the grains in the surface of the pellet are reacted. This is shown in Figure 3.2b, in which the dark color represents the already reacted grains, while the bright color represents the unreacted grains. Also in this case, a relationship describing the time needed to reach a conversion is reported:

$$t = (\tau_{DP} + \tau_{DG}[1 - 3\left(1 - X\right)^{2/3} + 2\,(1 - X)\Big] + \tau_{MT}[X] + \tau_{R}[1 - (1 - X)^{1/3}] \textit{ equation 3.6}$$

Where τ_{DG} is the characteristic time for diffusion through the grain and τ_R is the characteristic time for chemical reaction at the interphase between the unreacted core and the reacted layer of the grain. τ_{DP} and τ_{MT} are defined as in the unreacted shrinking-core. The mean conversion at each time in the whole pellet is calculated by the following equation:

$$X(t) = \Big[\int_0^R 4\pi R^2 X(R,T)dR\Big] / (\frac{4}{3}\pi R^3) \qquad \textit{equation 3.7}$$

These models can be considered suitable for non-porous pure metal oxide, but in the case of nanoporous materials (< 100 nm) other models have to be contemplated due to the importance of diffusion *phenomena*. Among them, the Knudsen model is the most commonly proposed. When the pore diameter is smaller than the mean free path of the gas molecules (ŋ), the diffusion is the dominant mechanism, and therefore the frequency of molecular collisions would be small relative to that of molecule-wall collisions, and therefore these latter

phenomena govern the gas diffusion (Figure 3.2c). In this particular case, the diffusion coefficient can be described by the Knudsen equation:[21,22]

$$D = \frac{2}{3} r \sqrt{\frac{8RT}{\pi M}} \qquad \textit{equation 3.8}$$

Where r is the porous radius, R the gas constant, T the temperature and M the molar mass

The diffusion decreases with decreasing pore diameter. The kinetic theory of gases can be used to estimate the mean free path, ŋ:

$$\eta = \frac{2.33 \times 10^{-20} T}{\varepsilon^2 p} \qquad \textit{equation 3.9}$$

where Ɛ is the molecular diameter (cm) and P the pressure (torr).

However, the Knudsen assumption breaks down when the pore diameter is nearly the same size as the molecule diameter and other models have to be taken into account.

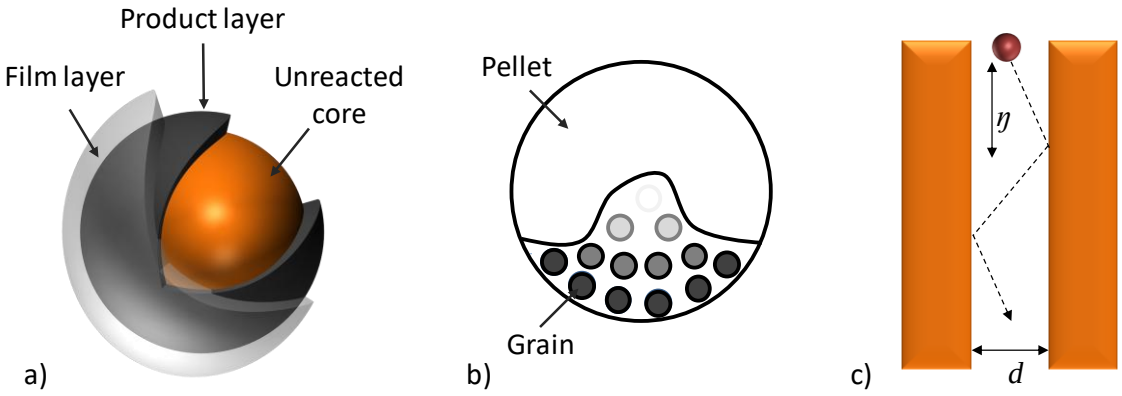

Figure 3.2 Representation of: a) unreacted shrinking core model; b) grain model and c) Knudsen model

3.4 Selection of the metal oxide phase

Zinc, manganese, copper, iron, rare earth, oxides and calcium carbonate are among the most promising and most extensively studied systems. A brief description of the features has been reported in the following.

Calcium-based sorbent: calcium carbonate such as limonite ($CaCO_3$) and dolomite ($CaCO_3 \cdot MgCO_3$) are low cost and can be used in both reduction and oxidation conditions from about 600 °C to 800 °C. A remarkable increase of the H_2S performance occurs from 880 °C, when $CaCO_3$ is decomposed to CaO (lime) and CO_2. This property renders these materials suitable for system operating at high temperature.

Copper-based sorbent: copper oxide permits to achieve low level of H_2S if it is not reduced to elemental copper. However, copper oxide readily reduces under high temperature and reducing atmosphere to elemental copper whose activity for sulphidation is an order of magnitude lower than Cu_2O and CuO.

Zinc-based sorbent: zinc oxide is one of the metal oxides that has the most favourable thermodynamics for H_2S removal, but under reducing atmosphere of syngas at temperature above 550 °C the vaporization of elemental zinc can represent a significant problem.

Manganese-based sorbent: manganese oxide under a reducing gas environment is reduced to MnO. The thermodynamics of MnO sulphidation is not as favourable as for some other metal oxides such as zinc oxide and copper oxide. However, MnO does not readily decompose to elemental manganese in reducing environment, offering the advantage to be stable at high temperature. The main disadvantage of manganese sorbent is the high regeneration temperature.[23]

Iron-based sorbent: low cost and potential fast reaction kinetics with H_2S makes it one of the most promising sorbent at mid-temperature. Above 500 °C, iron oxide reduction and possible carbide formation can inhibit the performance. Furthermore, at 700 °C in presence of syngas, Fe_3O_4 is reduced to FeO, that shows detrimental effects on the sulphidation reactivity.[3]

Cobalt-based sorbent: cobalt oxide shows good desulphidation performance up to 600 °C. However, in the reducing atmosphere at temperature higher than 300 °C, the reduction to metallic cobalt takes place, limiting its use to low temperature.[7]

Rare earth-based sorbents: rare earth-based sorbents show promising performance, but are very expensive and critical material. In contrast to copper, where reduced species are not very efficient to H_2S removal, the reduced species of cerium and lanthanum have been proved to be more active than the starting oxide phase. This makes rare-earth materials suitable for desulphidation in highly reducing syngas.[3]

Mixtures of different oxides (ZnO, CuO, $ZnO\text{-}Fe_2O_3$, $CuO\text{-}Fe_2O_3$, $CuOAl_2O_3$)[3] **or mixed metal oxides** ($ZnFe_2O_4$,[24] $CoFe_2O_4$,[25] $ZnTiO_3$[26]) have been further proposed, profiting of the synergic effect of the different metal oxides.

Among these potential metal oxides and mixed metal oxides, calcium carbonates show interesting desulphidation performances just at high temperature, while manganese oxide[23] need to be regenerate at temperatures over the mid-temperature range. These conditions

render these materials difficult to be proposed, being one of the main conditions strictly related to the temperature range (300-600 °C) of the process (intended as sulphidation and regeneration steps). Another key factor is related to the cost of the active phase: the continuous rise of the earth rare and cobalt price makes the corresponding sorbents hard to be considered as substitutes of the amines.

Taking into account these aspects, among the other proposed systems, our interest has fallen on **iron-based sorbents**. The choice derives from several reasons:

- low cost and no toxicity that make it available and easy to be handle;

- the sulphidation reaction with H_2S is favourite from a thermodynamic point of view;[7]

- fast reaction kinetics even at relative low temperature;[27]

- wide array of phases can be proposed, from hydroxides (goethite, ferrihydrite, etc.) to oxides (hematite, maghemite, magnetite etc.);

- sulphidation and regeneration can be performed in the mid-temperature range;

- a few studies at mid-temperature.

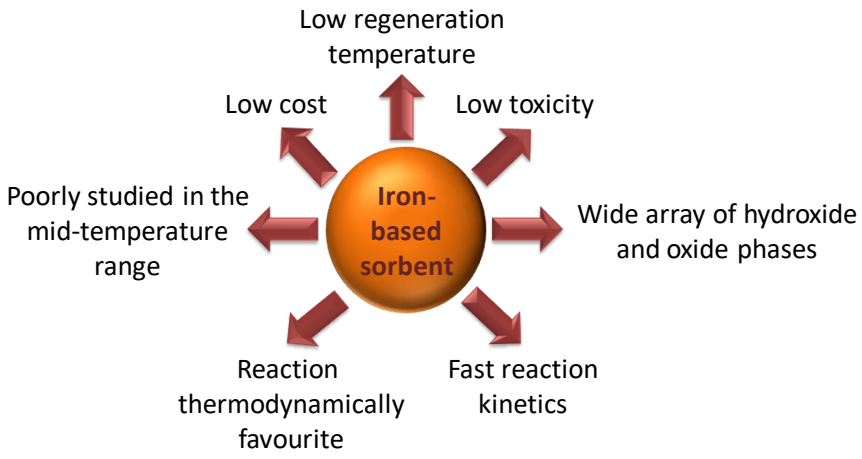

Figure 3.3 Potential advantages of using iron based-sorbents

The next section will deal with a brief but more detailed discussion of the different iron-based phases used as sorbents for H_2S removal.

3.5 Iron oxide based-sorbent

3.5.1 Sulphidation reactions of iron-based sorbents

Among the iron-based sorbents, iron oxides and iron hydroxides have been the most employed materials to remove H_2S since 1970s.[3] The general reaction during the desulphidation on iron(III) oxide at room temperature is:

$$Fe_2O_{3\,(s)} + 3H_2S_{(g)} \rightarrow Fe_2S_{3\,(s)} + 3H_2O_{\,(l)} \quad \Delta H = -22\ KJ/mol\ (at\ 25°C) \qquad equation\ 3.10$$

However, both temperature and reduction conditions of the syngas can lead to others sulphidation reactions.

High-temperature (600-900 °C) kinetic study of H_2S removal on 45 wt% iron oxide mixed with silica under syngas flow was carried out by Tamhankar *et al.*[28]. At these temperatures, the reaction between iron oxide and (H_2 + CO) (*equation 3.11*) takes place before the one with H_2S (*equation 3.11*) and almost all Fe_2O_3 is converted to metallic iron that reacts with H_2S (*equation 3.12*).

$$Fe_2O_{3\,(s)} + \frac{3}{2}\left(H_{2\,(g)} + CO_{(g)}\right) \rightarrow 2Fe_{(s)} + \frac{3}{2}(H_2O_{(g)} + CO_{2\,(g)}) \qquad equation\ 3.11$$

$$(1-x)Fe_{(s)} + H_2S_{(g)} \rightarrow Fe_{1-x}S_{(s)} + H_{2\,(g)} \qquad equation\ 3.12$$

Where $Fe_{1-x}S$ represents pyrrhotite phase and x may range between 0 and 0.2. Kinetics studies have shown that the hydrogen concentration has no effect on the sulphidation rate in a wide range of concentrations, and the sulphidation reaction is of the first order with respect to H_2S concentration. Moreover, the low activation energy for sulphidation (3.3 kcal/mol) has been attributed to the dissociative adsorption mechanism.[28] This mechanism has been even proposed by Davydov *et al.*[29] for the sulphidation of hematite (α-Fe_2O_3) or amorphous ferric hydroxide at room temperature. Replacement of O^{2-} anion by one of the two different species formed from the dissociation of H_2S (S^{2-} and SH^-) has been detected, accompanied by water formation. Comparison between the sulphidation at high and room temperature, points out as the temperature plays a crucial role on the sulphidation reaction.

The same authors carried out a desulphidation study with ferric hydroxide at room temperature: beyond the formation of Fe_2S_3 species, another reaction leads to sulphur elemental formation by oxidation of S^{2-} to S^0 and reduction of Fe^{3+} to Fe^{2+}, according with the main reaction:

$$2Fe(OH)_{3(s)} + 3H_2S_{(g)} \rightarrow 2FeS_{(s)} + \frac{1}{8} S_{8(s)} + 6H_2O_{(l)}$$ *equation 3.13*

with sulphur distribution of 67 % on FeS and 33 % on S^0.

Another fundamental aspect that can affect the sulphidation performance is played by the crystallographic phase of the iron based-sorbent. Several studies have been devoted to identify the most reactivity iron-based phase. Cantrell *et al.*[30] proved as ferrihydrite ($5Fe_2O_3 \cdot 5H_2O$) showed better H_2S sulphidation performances than hematite (α-Fe_2O_3) and goethite (α-FeOOH) at room temperature, with about 80 %, 11 % and 0.6 % of the available ferric iron involved in the reaction with H_2S for ferrihydrite, goethite, hematite respectively. Comparable results were found by Huang *et al.*[31] for commercial hematite: almost zero H_2S was removed at low temperature (experiment performed up to 80°C). The authors justified this result with the necessity of working at 300-400 °C in order to overcome the activation barrier of the sulphidation reaction. Furthermore, the H_2S removal performances were tested even on maghemite (γ-Fe_2O_3), highlighting as this phase showed remarkable sulphidation performance also at low temperature, with a gradual improvement with increasing temperature. At low temperature, the reaction between γ-Fe_2O_3 and H_2S can occur through a direct exchange of sulphur with oxygen ions to form sulphide species and water:

$$Fe_2O_{3(s)} + 3H_2S_{(g)} \rightarrow Fe_2S_{3(s)} + 3\,H_2O_{(l)}$$ *equation 3.14*

Pure maghemite phase was tested at mid-temperature (300 °C) by Mureddu *et al.*[27] in order to understand the possible sulphidation reactions. After the sulphidation run, the corresponding XRD patterns showed the presence of pyrrhotite ($Fe_{1-x}S$) and pirite (FeS_2), as well as a minor amount of unreacted maghemite. These examples point out as different parameters, e.g. the operating temperature and the active phase, can be crucial on those reactions directly correlated with the performance of the sorbent.

3.5.2 Regeneration reactions of iron oxide-based sorbents

Beyond the sulphidation step, the regeneration step has to be considered. Also in this case, different chemical reactions can take place on the basis of the operating conditions. If the Fe_2S_3 phase is preserved, the regeneration leads to the formation of elemental sulphur,[32] according to the following reaction:

$$\frac{1}{3}Fe_2S_{3(s)} + \frac{1}{2}O_{2(g)} \rightarrow \frac{1}{3}Fe_2O_{3(s)} + S_{(s)}$$ *equation 3.15*

However, the Fe_2S_3 is thermodynamically unstable under mid- and hot-temperature conditions, and reacts further to form pyrite (FeS_2) and Fe_3S_4.[33] Therefore, under these conditions, the regeneration process can be described by the following reactions:[34]

$$4FeS_{2(s)} + 11O_{2(g)} \rightarrow 2\,Fe_2O_{3(s)} + 8\,SO_{2\,(g)} \qquad \textit{equation 3.16}$$

$$Fe_3S_{4(s)} + 2O_{2(g)} \rightarrow Fe_3O_{4(s)} + 4S_{(s)} \qquad \textit{equation 3.17}$$

The last equation should lead to the formation of magnetite (Fe_3O_4). The regeneration was further studied by Tseng *et al.*[28] under O_2 or SO_2 gas flows at hot-temperature. The pyrrhotite ($Fe_{1-x}S$) species obtained after sulphidation at high-temperature leads to the formation of Fe_2O_3 (no phase declared) when O_2 was employed, while the use of SO_2 leads to the formation of magnetite (Fe_3O_4) and elemental sulphur.

3.6 From micrometric to nanometric metal oxide

From the previous discussion, it is clear that the sulphur removal capacity of a sorbent is strictly related to the operating temperature and the crystallographic phase but other factors as textural properties strongly affect it. Indeed, it is well known that in principle the performances can be maximised if the number of atoms able to interact to the H_2S is maximised too. In this framework, the use of nanoparticles in place of microparticles could be considered a logical step to improve the number of atoms available at the surface. However, already at mid-temperature, sintering *phenomena* between the nanoparticles could take place, causing the formation of micrometric particles, and thus the inevitable decrease of the removal capacity. The possible solutions to overcome this issue could be (i) the creation of thermally stable mesoporous/mesostructured metal oxide or (ii) the dispersion of the active phase as nanophase into a thermally stable mesoporous/mesostructured support. Figure 3.4 summarizes the various approaches to maximize the contact surface of the metal oxide with H_2S.

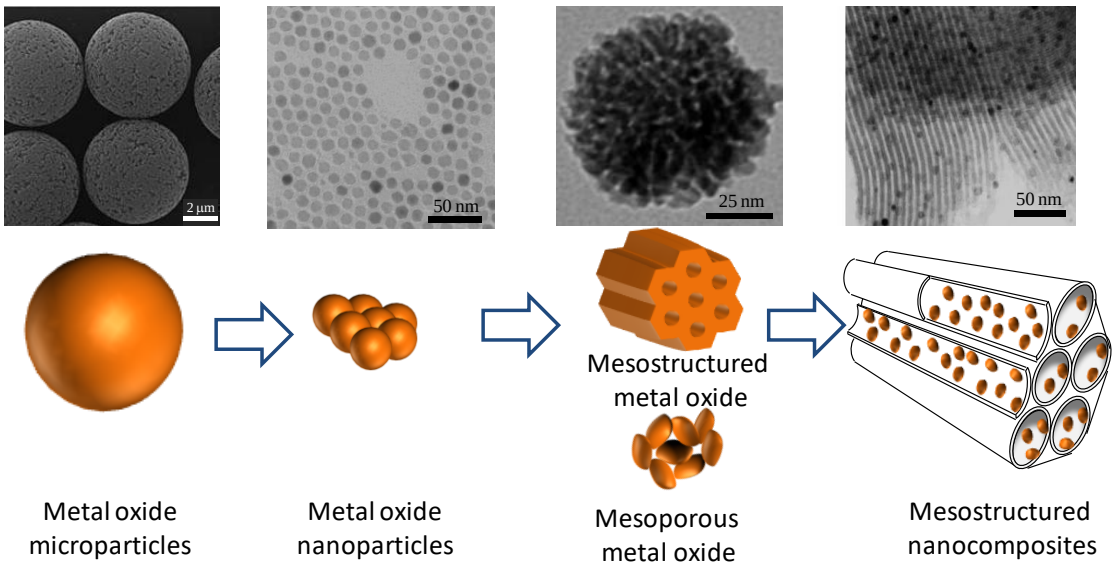

Figure 3.4 Representation of the potential ways to improve the contact surface in a metal oxide. Adapted in part from {[35]} with permission of The Royal Society of Chemistry

3.6.1 Mesoporous nanostructured metal oxide

Mesoporous and mesostructured metal oxides showing high surface area, have been proposed as a H_2S sorbent during the last decades. Two recent examples will be presented following.

Pahalagedara *et al.*[25] synthesized and tested under low temperature condition (<300 °C) mesoporous cobalt oxides (Co_3O_4) based-sorbents (Figure 3.5 a, b). The most promising sorbent showed sulphur retention capacity almost 50 times higher than that of micrometric commercial Co_3O_4 powder, due to the higher surface area and nanometric particles dimension. However, after the first regeneration run, the H_2S performance of the mesoporous sample results to be halved (from 67.7 g_S /100 $g_{sorbent}$ to 33.7 g_S / 100 $g_{sorbent}$) probably due to the partial collapse of the porous structure.

Three-dimensionally ordered macroporous (3DOM) magnetite prepared by a colloidal crystal templating method (Figure 3.5 c, d) (see chapter 1 paragraph 2.3) have been successfully tested by Huang *et al.*[31] The sorbent shows notable surface area value (~120 m^2g^{-1}) and much better H_2S removal performance than commercial maghemite sorbent, probably due to the higher surface area. However, after the first regeneration step, the performance reduces to less than one-third of that of the fresh materials, probably due to, once again, a significant decrease of the surface area (from 223 m^2g^{-1} to 78 m^2g^{-1}).

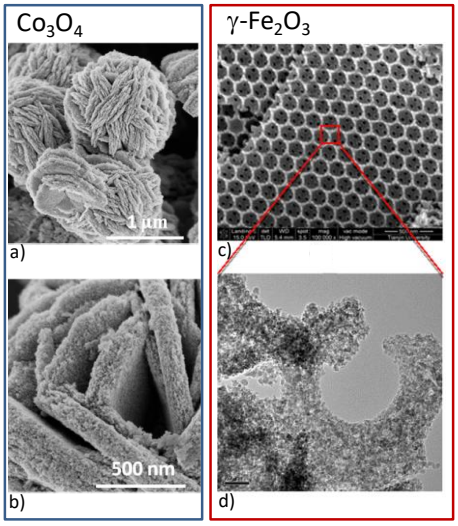

Figure 3.5 a, b) Mesoporous cobalt oxide synthesized by Pahalagedara and co-workers. Reprinted (adapted) with permission from ([25]). Copyright (2014) American Chemical Society. c, d) Three-dimensionally ordered macroporous (3DOM) iron oxides. Reprinted with permission from ([31]). Copyright (2015) American Chemical Society

Considering these results, the main limitation of the metal oxide based-sorbents seems to be hidden behind their lacking pores stability that causes, after the first regeneration run, a partial collapse of the porous structure and an inevitable loss of the surface area really available for the gas-solid reaction.[36] Therefore, the potential extraordinary performance of mesoporous metal oxide built up employing a promising metal oxide active phase with respect to the corresponding bulk material, will be kept just in a limited number of sulphidation-regeneration cycles. Indeed, even if the thermal stability of the porous structure is much more higher than operating temperature, the phase transition from a species to another one during the sulphidation-regeneration cycles can cause and inevitable collapse of the porous structure, due to the different cell parameters of the different phases.[36]

3.6.2 From pure nanometric metal oxide to mesostructured nanocomposites.

An efficient strategy to overcome the typical issues of non-porous and porous (mesoporous/mesostructured) pure metal oxide-based sorbents could be the dispersion of the metal oxide (active phase) into thermally stable ad inert porous supports. The corresponding **composites** obtained by this combination will show, at least in principle, steady sulphidation performances during numerous cycles, due to the intrinsic capacity of the porous support to inhibit the sintering of the active phase. Moreover, being the diameter of the pores a real limitation in the active phase particles' growth, the use of mesoporous/mesostructured support (pore diameter within 2-50 nm) will guarantee the production of **nanocomposites**, in which the active phase is nanosized.

Recently, different mesostructured MeO nanocomposites have been proposed as H_2S removers, confirming remarkable and better desulphidation-regeneration performance than the corresponding non supported counterpart.[37,38] A few of them are devoted to iron oxide. Wang *et al*. for the first time investigated adsorption of H_2S on ZnO/SBA-15[32] and Fe_2O_3/SBA-15[39] at room temperature, while Mureddu *et al*. proved as ZnO/SBA-15[40] and Fe_2O_3/SBA-15[27] can be used repeatedly at mid-temperature.

Among the examples proposed in the literature, some of them are devoted to mesostructured composites in which the high content of the active phase chosen induced the formation of microparticles outside the pore, and as a consequence suffers of sintering drawback, typical for non supported phases.[41,42] On the basis of the results reported in the literature it is clear that the strategy to disperse the active phase, as well as the active phase content, play a key role in the sorbents performances. For these reasons, the next section will be devoted to the description of the impregnation techniques employed to create the mesostructured nanocomposites.

3.6.3 Impregnation methods to mesostructured nanocomposites.

The impregnation is a common technique used to functionalize material surfaces with metal species (as metals, oxides, sulphites) to obtain the corresponding composites. The main advantage is its simplicity and the limited waste production. The impregnation techniques consist in contacting a solid with a liquid containing the species to be deposited into/over the support.[43] The process is largely used to render inactive materials that shows other peculiar properties active. A representative example could be the mesostructured silicas, that show unique features such as high surface area, ordered porous structure and high pore volume, but result to be inactive as sorbents. During the impregnation different processes take place with different rates:

- Selective adsorption of species (charged or not) by Coulomb force, van der Waals forces or H-bonds;
- Ion exchange between the charged surface and the electrolyte;
- Reaction of the species (molecules, ions) attached to the surface (such as condensation).

Usually, during impregnation a suitable support is contacted with a solution containing the precursor of the active phase. The successive removal of the solvent (by evaporation or filtration) promotes the interaction between the active phase and the pores surface. There are two different methods of impregnation: the wet impregnation and the incipient wetness

impregnation.[43] In the first case, the volume of solution containing the inorganic precursor is much more than the total pore volume of the mesoporous silica, whereas in the second case, the amount of solution is equal to the pore volume. The expedient of the last case is essentially made to avoid the deposition of metal precursor outside of the pores, and the consequent formation of microcrystal after the thermal treatment. After the wet or dry impregnation process, the impregnated support material needs to be dried in order to allow the precursor compound to be converted into a more suitable chemical phase. Although the drying of an impregnated support material appears to be very simple, it should be noted that the conditions during drying can adversely influence the distribution of the precursor over the support material. As a result of these flows, the precursor material is entrained through the pores, which can lead to inhomogeneous distribution after drying. To prevent redistribution of the precursor during drying special measures have to be taken, *e.g.* by carefully controlling the drying rate of the impregnated bodies. After drying the precursor of the active phase is usually converted into the desired phase, *e.g.* by calcination, yielding a compound in the oxidized state. A subsequent reduction treatment can be used to convert the active phase into metallic state.

Recently, a new impregnation strategy called **two solvents**, has attracted particular interest,[44,45] due to the capacity to guarantee a better dispersion of the active phase.[46] Essentially, silica powder is dispersed in a hydrophobic solvent (*n*-hexane, cyclohexane, *n*-pentane), and a volume equal to the silica pore volume of the metal precursor aqueous solution is added consequently. The following evaporation of the hydrophobic solution leads to the impregnated materials that, after drying and thermal treatment processes, shows better dispersion of the active phase with respect to other methods.[47] In order to explained this result, an interesting paper has been published by Denoyel and co-workers,[46] in which the better result are justified considering that the hydrophobic solvent caused a pushing of the water against the silica wall, causing a rehydroxylation of the surface, intended as an increase in the number of geminal and hydrogen-bonded silanol groups (Figure 3.6). This phenomenon causes an increase of the hydrophilicity of the surface, that could favour the interaction with the metal oxide precursor.

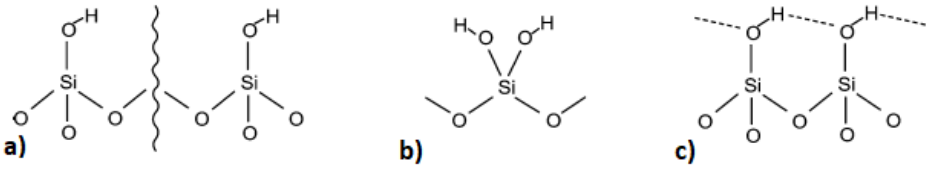

Figure 3.6 Proposed silanol groups at the silica surface: (a) isolated silanols, (b) geminal silanols and (c) hydrogen-bonded silanols.

3.6.4 Requirements of the nanocomposites for H_2S removal at mid-temperature

Besides the general sorbent requirements described in the paragraph 3.2, further characteristic have to be shown by the mesostructured support of the **nanocomposites**:

- Inactiveness toward the raw syngas;
- Low-cost and low toxicity;
- High thermal stability of the porous structure.

Moreover, in order to efficiently disperse the active phase into the pores and avoid plugging phenomena, further characteristics are needed:

- High surface area;
- Large pore volume;
- Monomodal and narrow pore size distribution.

Here, it is reported a schematic representation of the main features needed for an efficient and regenerable sorbent for H_2S at mid-temperature (Figure 3.7).

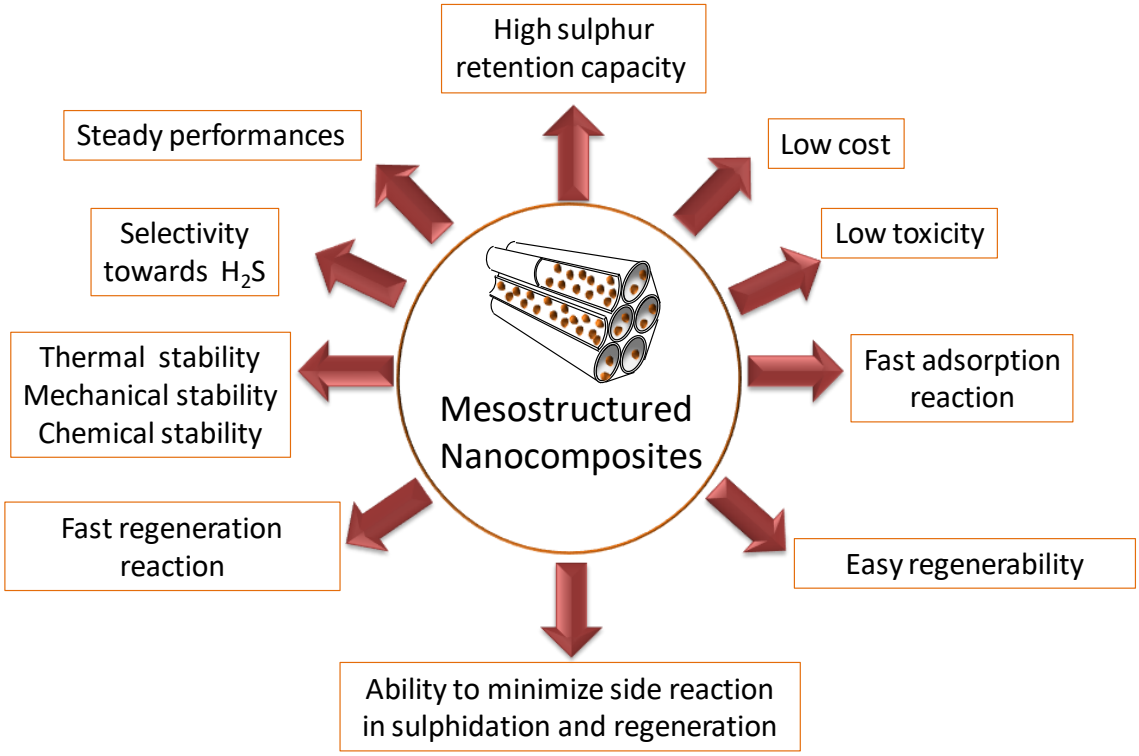

Figure 3.7 Schematic illustration of the requirements of an ideal composite for mid-temperature H_2S removal

References

1 X. Ma, X. Wang and C. Song, *J. Am. Chem. Soc.*, 2009, **131**, 5777–5783.

2 W. F. Elseviers and H. Verelst, *Fuel*, 1999, **78**, 601–612.

3 S. Cheah, D. L. Carpenter and K. A. Magrini-Bair, *Energy and Fuels*, 2009, **23**, 5291–5307.

4 A. Samokhvalov and B. J. Tatarchuk, *Phys. Chem. Chem. Phys.*, 2011, **13**, 3197–209.

5 L. Li, T. H. Sun, C. H. Shu and H. B. Zhang, *J. Hazard. Mater.*, 2016, **311**, 142–150.

6 S. Cheah, D. L. Carpenter and K. A. Magrini-Bair, *Energy and Fuels*, 2009, **23**, 5291–5307.

7 P. R. Westmoreland and D. P. Harrison, *Environ. Sci.*, 1976, **10**, 659–661.

8 M. S. Shah, M. Tsapatsis and J. I. Siepmann, *Chem. Rev.*, 2017, **117**, 9755–9803.

9 J. Bin Chung and J. S. Chung, *Chem. Eng. Sci.*, 2005, **60**, 1515–1523.

10 J. Skrzypski, I. Bezverkhyy, O. Heintz and J. Bellat, *Ind. Eng. Chem. Res.*, 2011, **50**, 5714–5722.

11 D. A. Bell, B. F. Towler and M. Fan, in *Coal Gasification and Its Applications*, Elsevier,

2011, pp. 1–15.

12 Julianne M. Klara Senior, *Technology*, 2007, **1**, 51–297.

13 J. A. Rodriguez, S. Chaturvedi, M. Kuhn and J. Hrbek, *J. Phys. Chem. B*, 1998, **102**, 5511–5519.

14 J. A. Rodriguez, T. Jirsak and S. Chaturvedi, *J. Chem. Phys.*, 1999, **111**, 8077–8087.

15 P. F. M. T. van Nisselrooya and J. A. Lagasb, *Catal. Today*, 1993, **16**, 263–271.

16 K.Polychronopoulou, F.Cabello Galisteo, M.López Granados, J.L.G.Fierro, T.Bakas and A.M.Efstathiou, *J. Catal.*, 2005, **236**, 205–220.

17 J. A. Rodriguez and A. Maiti, *J. Phys. Chem. B*, 2000, **104**, 3630–3638.

18 J. Song, X. Niu, L. Ling and B. Wang, *Fuel Process. Technol.*, 2013, **115**, 26–33.

19 M. Casarin, C. Maccato and A. Vittadini, *Surf. Sci.*, 1997, **377**–**379**, 587–591.

20 R. Zhang, H. Liu, J. Li, L. Ling and B. Wang, *Appl. Surf. Sci.*, 2012, **258**, 9932–9943.

21 M. Knudsen, *Ann. Phys.*, 1909, **333**, 75–130.

22 M. Knudsen, *Ann. Phys.*, 1915, **351**, 641–656.

23 M. T. H. R. Ben-Slimane, *Energy Fuels*, 1995, **9**, 372–378.

24 N. O. Ikenaga, Y. Ohgaito, H. Matsushima and T. Suzuki, *Fuel*, 2004, **83**, 661–669.

25 L. R. Pahalagedara, A. S. Poyraz, W. Song, C. Kuo, M. N. Pahalagedara, Y. Meng and S. L. Suib, *Chem. Mater.*, 2014, **26**, 6613–6621.

26 K. Jothimurugesan and S. K. Gangwal, *Ind. Eng. Chem. Res.*, 1998, **37**, 1929–1933.

27 M. Mureddu, I. Ferino, A. Musinu, A. Ardu, E. Rombi, M. G. Cutrufello, P. Deiana, M. Fantauzzi and C. Cannas, *J. Mater. Chem. A*, 2014, **2**, 19396–19406.

28 S. C. Tseng, S. S. Tamhankar and C. Y. Wen, *Chem. Eng. Sci.*, 1981, **36**, 1287–1294.

29 A. Davydov, K. T. Chuang and A. R. Sanger, *J. Phys. Chem. B*, 1998, **102**, 4745–4752.

30 K. J. Cantrell, S. B. Yabusaki, M. H. Engelhard, A. V Mitroshkov and E. C. Thornton, 2003, **37**, 2192–2199.

31 G. Huang, E. He, Z. Wang, H. Fan, J. Shangguan, E. Croiset and Z. Chen, *Ind. Eng. Chem. Res.*, 2015, **54**, 8469–8478.

32 X. Wang, T. Sun, J. Yang, L. Zhao and J. Jia, *Chem. Eng. J.*, 2008, **142**, 48–55.

33 A. Davydov, K. T. Chuang and A. R. Sanger, 1998, **5647**, 4745–4752.

34 R. Walker, A. D. Steele and T. D. B. Morgan, *Surf. Coatings Technol.*, 1988, **34**, 163–175.

35 D. Amara, J. Grinblat and S. Margel, *J. Mater. Chem.*, 2010, **20**, 1899.

36 M. S. Shah, M. Tsapatsis and J. I. Siepmann, *Chem. Rev.*, 2017, **117**, 9755–9803.

37 M. Mureddu, I. Ferino, E. Rombi, M. G. Cutrufello, P. Deiana, A. Ardu, A. Musinu, G. Piccaluga and C. Cannas, *Fuel*, 2012, **102**, 691–700.

38 M. Hussain, N. Abbas, D. Fino and N. Russo, *Chem. Eng. J.*, 2012, **188**, 222–232.

39 X. Wang, J. Jia, L. Zhao and T. Sun, *Water. Air. Soil Pollut.*, 2008, **193**, 247–257.

40 M. Mureddu, I. Ferino, E. Rombi, M. G. Cutrufello, P. Deiana, A. Ardu, A. Musinu, G. Piccaluga and C. Cannas, *Fuel*, 2012, **102**, 691–700.

41 Z. B. Huang, B. S. Liu, X. H. Wang, X. Y. Tang and R. Amin, *Ind. Eng. Chem. Res.*, 2015, **54**, 11268–11276.

42 L. Li, T. H. Sun, C. H. Shu and H. B. Zhang, *J. Hazard. Mater.*, 2016, **311**, 142–150.

43 D. Gu and F. Schüth, *Chem. Soc. Rev.*, 2014, **43**, 313–344.

44 M. Imperor-Clerc, D. Bazin, M. D. Appay, P. Beaunier and A. Davidson, *Chem. Mater.*, 2004, **16**, 1813–1821.

45 I. Lopes, N. El Hassan, H. Guerba, G. Wallez and A. Davidson, *Chem. Mater.*, 2006, **18**, 5826–5828.

46 J. Van Der Meer, I. Bardez-Giboire, C. Mercier, B. Revel, A. Davidson and R. Denoyel, *J. Phys. Chem. C*, 2010, **114**, 3507–3515.

47 M. Mureddu, I. Ferino, E. Rombi, M. G. Cutrufello, P. Deiana, A. Ardu, A. Musinu, G. Piccaluga and C. Cannas, *Fuel*, 2012, **102**, 691–700.

4. Design of siliceous and non-siliceous supports

Abstract

This chapter will discuss the different synthetic routes employed to tailor siliceous and non-siliceous supports. In the first section, the attention will be focused on siliceous materials with the aim of tuning pore structure, pore dimension and particles size, while the second will be devoted to the description of the strategies set up to fabricate mesoporous and mesostructured crystalline anatase.

4.1 Introduction

Taking into account the requirements needed to develop efficient sorbents for H_2S removal, two different mesostructured materials, silica and titania, have been chosen to host the Fe_2O_3 active phase. Although active phase plays the main role in the final performance of such sorbents, it is clear the strategic role of the nature and the textural properties of the support in the H_2S diffusion kinetics within the pores during sulphidation-regeneration cycles and in the dispersion of the active phase within the pores.

Firstly, both silica and titania do not show any ability to react with H_2S, which is an essential prerequisite to retain their porous structure. Secondly, for both materials, the literature proposes different approaches to obtain them in form of mesostructures. Moreover, for siliceous materials, the deep knowledge and the ability to control the sol-gel reactions involved offer the opportunity to modify surface area, pore structure, pores size and wall thickness. Recent efforts in fine tuning the features of **mesostructured siliceous materials** have opened the way to the design of highly thermally stable supports for highly efficient and regenerable catalysts and sorbents. Indeed, ZnO-SBA15[1] and Fe_2O_3-SBA15[2] nanocomposites have been found to be highly efficient and regenerable sorbents, due to the effective dispersion of active phase within the mesochannels of the hexagonally ordered porous structure. Starting from this promising result, this work aims to improve the performance of the silica support by maximizing the dispersion capacity and to offer alternative supports to those proposed in the literature to date.

4.2 Design of siliceous supports

Since the pioneering work of the Mobil scientists,[3] continuous efforts have been made to develop suitable synthetic pathways able to tailor textural and morphological properties of silica, making these materials promising candidates in a wide variety of applications.[4] Motivated by this fact, and aware that the "physical chemistry of organized matter" relies on the successful combination of sol-gel chemistry and self-assembly procedures,[4] different synthetic routes have been designed, with the ambition to be able to control and predict textural and morphological properties of the synthesized materials. In the next paragraphs, only the more interesting results will be presented and discussed. Effects of different synthetic parameters (as reagents or hydrothermal treatment) have been tested and studied to control both textural parameters as surface area, pore structure, pore diameter and silica wall dimension, as well as morphology, dimension, and size distribution of the particles from the micrometric to the nanometric scale.

4.2.1 Improvement of the surface area

Maximization of surface area should, in principle, improve H_2S-retention performance, due to a better dispersion of the active phase into the support. In this context, within the mesoporous range, a reduction in pore diameter and in wall thickness may represent a suitable way to improve the textural properties of the support. As extensively reported in the literature, conventional SBA-15 silica is characterized by a surface area in the range 600-1000 m^2g^{-1}, pores diameter in the range 4-30 nm, and silica walls in the range 3-6 nm with hexagonal porous structure (space group *P6mm*).[5] Considering these facts, a remarkable reduction in these values and the consequential increase in surface area can be achieved by generating another typology of silica, named MCM41S. This type of silica shows pore diameter of about 2-3 nm and wall thickness of almost 2 nm. Differences in pore diameter and wall thickness are principally ascribed to the different templating agent employed in the syntheses. Indeed, in the case of MCM41S, a cationic surfactant is used (usually cetyltrimethylammonium bromide, $C_{16}H_{33}N(CH_3)_3\ Br^-$, CTAB) to generate the supramolecular template and pore size dimension is strictly related to the length of the carbon chain. Therefore, different typologies of cationic surfactants, featuring different carbon chain length, have been tested to control the pore dimension (C_8-C_{18}).[4] For SBA-15, the cationic surfactant is substituted with Pluronic® P123, triblock copolymer (polyethylene oxide-polypropylene oxide-polyethylene oxide $PEO_{20}PPO_{70}PEO_{20}$ Average Molar Weight (AMW) = 5800 g mol^{-1}). Both pore size and silica walls can be tailored by changing the dimension of the hydrophilic (PEO) and hydrophobic (PPO) polymer chains.[4]

Another approach to maximize the surface area may be the creation of a tri-dimensional porous structure (3-D) in place of a bi-dimensional (2-D) one. Moreover, a 3-D structure could assure improved accessibility to the dispersed active phase into the mesochannels. Silica cubic pore structures (*Ia3d*) are commonly obtained by using a CTAB/TEOS ratio > 1 in both aqueous or hydro-ethanolic media.[6–8] Alternatively, Pluronic® F127 can be added as co-template to CTAB in hydro-ethanolic media, keeping the CTAB/TEOS ratio in the range typical of the hexagonal porous structure synthesis. Moreover, only in one case, silica with cubic pore structure with space group *Pm3n* was obtained by the proper use of ethyl acetate in aqueous media employing 3-aminopropyl triethoxysilane (APTES) in addition to TEOS.[9]

4.2.1.1 Design of micrometric hexagonal (*P6mm*) and cubic (*Ia3m*) mesostructured silica particles

Figure 4.1 depicts the schematic representation of the different synthetic routes set up to obtain micrometric SBA15 (*P6mm*), MCM41 (*P6mm*) and MCM48 (*Ia3d*) mesostructured silica supports. Comparing the two synthetic approaches of SBA15 and MCM41, it can be pointed out that, besides the use of different templates agents (Pluronic *vs.* CTAB), SBA15 synthesis is performed in acidic solution, while in the case of the MCM41 a basic environment is required. This can be explained considering the different types of interaction between the template and the inorganic framework for the mesophase formation: in the case of MCM41 electrostatic interactions are thought to be the driving force, while in the case of SBA15 H-bonding is suggested to be responsible of the porous order.[4] Another difference is the further step of the hydrothermal treatment, typically used for SBA15 to remove the high amount of micropores in the silica walls.[4] In the case of MCM41, different synthetic routes have been proposed with[3,8] and without the additional hydrothermal step.[6,10]

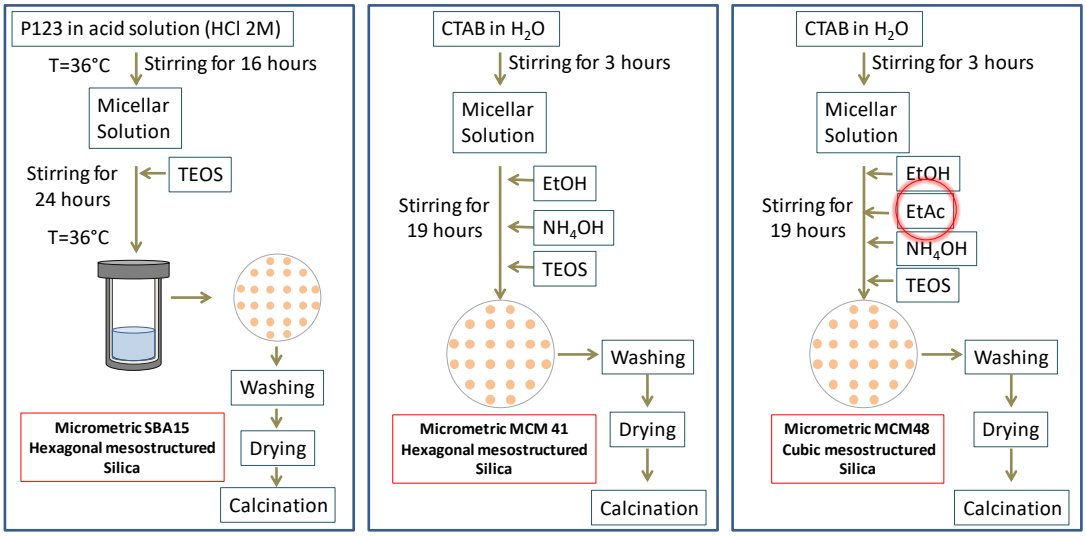

Figure 4.1 Schematic illustration of the synthetic route performed to obtain micrometric SBA15, MCM41 and MCM48 silica supports

Comparing MCM41 and MCM48, it is clear that the unique difference is in the use of a certain amount of ethyl acetate.

SBA15 mesostructured silica has been prepared according to the procedure reported by Zhao *et al*.[5] Typically, a solution of surfactant was prepared by vigorous stirring for 16 hours the mixture of 4 g of Pluronic P123, 30 g of distilled water and 120 g of HCl (2M) in a ethylene glycol bath maintained at 36 °C, until a clear solution was obtained. Then, 9 g of tetraethyl orthosilicate (TEOS) was added dropwise and vigorously stirred for 24 hours at 36 °C, allowing the hydroxylation and condensation reactions to occur. The resulting milky suspension was transferred into a teflon-lined autoclave and heated statically at 100 °C for 24 hours. The resulting white precipitate was recovered by filtration, washed with large amounts of warm distilled water and then dried at 35 °C for 24 hours. The final product was calcined under air atmosphere at 550 °C for 6 hours (heating rate 5°C min^{-1}) to remove the organic template and any impurity.

Micrometric MCM41 silica particles were synthesized by dissolving 1 g of hexadecyltrimetylammonium bromide (CTAB) in 200 mL of distilled water and keeping the resulting solution under stirring at 300 rpm for 3 hours at room temperature. Then, 87.4 mL of ethanol and 21 mL of ammonium hydroxide were added in the solution; after 20 min, stirring speed was increased to 600 rpm before adding 3.79 mL of TEOS. Transparent starting solution became white opalescent and the resulting dispersion was kept for 19 hours under mild stirring (300 rpm). Finally, the solid was separated from the solution by centrifugation and washed three times with 20 mL of 1:1 v/v mixture of ethanol and water. The solid was dried

overnight at 80 °C and then calcined at 550 °C for 4 hours (heating rate, 5°C min^{-1}) to remove the organic template.

In order to obtain micrometric silica with a cubic pore structure, the synthetic strategy used for micrometric hexagonal silica was modified by adding 3.79 mL of ethyl acetate soon after the addition of ethanol while keeping all the other parameters unchanged. The obtained particles were dried over night at 80 °C and calcined a 550 °C for 4 hours (heating 5 °C min^{-1}) to decompose the organic template.

Sample	H_2O (mL)	HCl (mL)	P123 (g)	CTAB (g)	EtOH (mL)	NH_4OH (mL)	EtAc (mL)	TEOS (mL)	Yield (%)
SBA15	150	19.87	4.00	-	-	-	-	8.50	64
MCM41	-	-	1.01	87.4	21	-	-	3.79	90
MCM48	200	-	-	1.01	87.4	21	3.85	3.79	73

Table 4.1 Synthesis details of the samples SBA15, MCM41 and MCM48 supports

4.2.1.2 Characterization of micrometric hexagonal (*P6mm*) and cubic (*Ia3m*) mesostructured silica particles

Characterization of the supports has been performed through a multi-technique approach based on the combined used of low angle X-ray diffraction (LA-XRD) to verify the mesoporous structure, transmission electron microscopy (TEM) to detect both the porous order as well as the morphology of the particles and N_2-physisorption to study the textural properties (surface area, pores volume and pore size distribution). Figure 4.2a, e, and i depicts the LA-XRD patterns of the SBA15, MCM41 and MCM48 supports. All the samples show the presence of different reflexes, indicating a long-range ordering. *d*-spacing and cell parameter have been calculated and reported in Table 4.2. Taking into account the reflection positions and intensities, a hexagonal pore structure with space group *P6mm* has been assigned to SBA15 and MCM41 samples, and a cubic pore structure with space group *Ia3d* has been detected for MCM48. For MCM41 and MCM48, the comparison of the LA-XRD patterns before and after the calcination at 550 °C proves that the pore structure is well retained, in spite of the slight shift of the reflections toward higher angles which is symptomatic of an expected contraction in the value of the cell parameter due to the removal of the template.

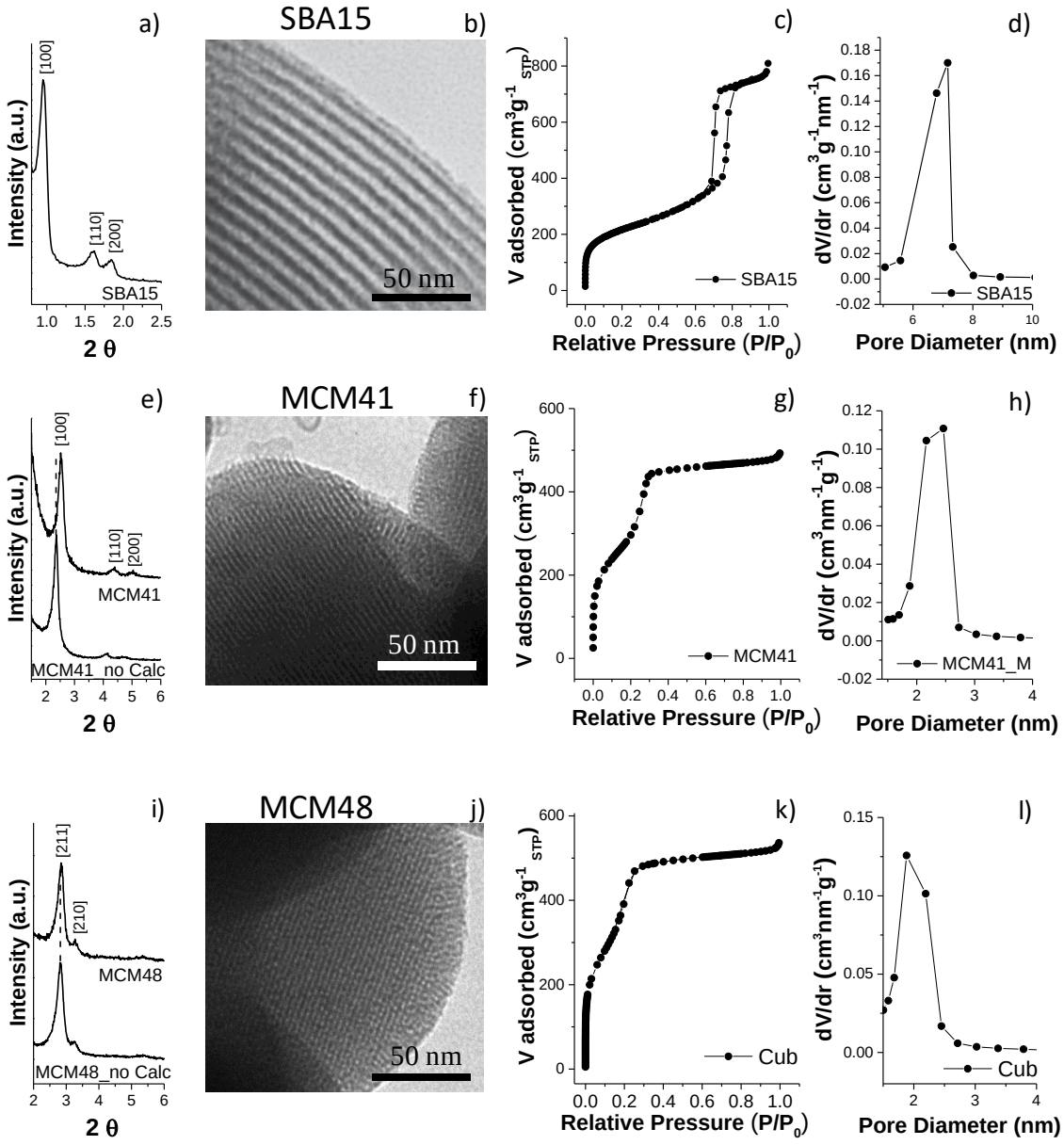

Figure 4.2 LA-XRD, field TEM images, N_2 adsorption-desorption isotherms and pore size distributions of the SBA15 (a, b, c, d) MCM41 (e, f, g, h) MCM48 (i, j, k, l) samples

Figure 4.2b, f, j reports representative TEM images of the samples. Micrometric particles, with well-ordered pore structure have been observed for all samples. It has also been possible to roughly estimate pore size and wall thickness, that in the case of SBA15 are 6-7 nm and 3-4 nm respectively, while in the other two cases are both of about 2 nm.

Figure 4.2c, g, k and Figure 4.2d, h, l report the N_2 adsorption-desorption isotherms and the related pore size distribution (PSD) calculated by BJH method on the desorption branch. MCM41 and MCM48 supports exhibit characteristic IVB type behaviour according to IUPAC classification:[11] beyond a microporous contribution, the presence of a mesoporous one is clearly indicated by the existence of a well-defined step in the 0.2-0.3 P/P_0 range as a

consequence of capillary condensation. SBA15 N_2-physisorption curve shows a characteristic IVA isotherm with capillary condensation at about 0.7 P/P_0, featuring a hysteresis loop.[11] BET surface areas, calculated in the range 0.05-0.3 P/P_0 for SBA15 sample and 0.05-0.17 P/P_0 for MCM41 and MCM48 (given the occurrence of capillary condensation in a different range of P/P_0 in MCM41 samples) have been reported in Table 4.2, along with pore volume values, calculated at 0.99 P/P_0. As expected, the reduction in pore diameter, causes a remarkable increase in surface area from 763 m^2g^{-1} (for SBA15) to 1063 m^2g^{-1} (for MCM41). The creation of 3-D pores structure (cubic *Ia3d*) together with the reduction in pore diameter values lead to a further increase in the surface area up to 1336 m^2g^{-1}.

Figure 4.2d, h, l reports the pore size distribution curves (PSD) of these samples. As expected, the SBA15 shows pore diameter of 7 nm, while MCM41 and MCM48 of about 2nm. The dimensions of wall thickness, calculated considering the cell parameters and the pore diameters, are reported in Table 4.2. As expected, SBA15 features a value of wall thickness of 4.2 nm, while a remarkable reduction in its value has been found in MCM41 (1.7 nm) and MCM48 (1.4 nm) samples.

Sample	$S_{BET}(m^2g^{-1})$	$V_p\ (cm^3g^{-1})$	$D_{pore}(nm)$	$w_t(nm)$	d_{100}	a_0
SBA15	763	1.1	7.1	4.2	9.3	11.3
MCM41	1063	0.76	2.2	1.7	3.5	4.0
MCM48	1336	0.83	2.1	1.4	3.1	7.7

Table 4.2 Textural features obtained by N_2-physisortion data for SBA15, MCM41 and MCM48 samples. S_{BET}=surface area, V_p= pore volume; D_p= pore diameter; wt= wall thickness. Relative standard deviation: %RSD (S_{BET})=2.1%; %RSD(V_p)=1.1%; %RSD(D_p)=1.8%. *d*-Spacing (d_{100}) and lattice parameter (a_0) obtained from the LA-XRD data.

To summarise, it has been proved that suitable use of ethyl acetate induces the formation of a tri-dimensional (*Ia3m*) pore structure. The remarkable increase in surface area values is due to the dual effect of the reduction in pore diameter and wall thickness values. The further increase in surface area derives from pore interconnectivity, typical of a 3-D cubic structure.

4.2.2 Hydrothermal restructuring effect

Hydrothermal treatment, usually performed on SBA15 support to decrease microporous contribution, has been proved to have some effects even in the case of MCM41. Although this hydrothermal effect has been widely used in the synthesis of MCM41,[12,13] just in few cases the effect has been described and explained. According to some authors, the main effects are the increase in pore size, the improvement of mesoporous order, and the higher thermal stability.[14] Sayari and co-workers[14] explained these effects, by considering that the high pressures and temperatures achieved in hydrothermal treatments allow an easier access of

water molecules into the pores causing the consequential solvation of the silicate framework and of the surfactants. This phenomenon leads to an effective swelling of the structure. Being the thermal stability and the mesoporous order of the sorbent key factors in the H_2S performance of the sorbent, the effect of hydrothermal restructuring has been studied.

4.2.2.1 Design of hexagonal (*P6mm*) mesostructured silica particles under hydrothermal restructuring

In order to study the effect of hydrothermal restructuring, the same synthetic route performed to obtain the sample MCM41 was followed and a further hydrothermal treatment, carried out by using an autoclave, was added. In detail, the starting hydro-alcoholic solution containing the surfactant was kept under stirring for three hours, and then EtOH, liquor ammonia, and TEOS were added. After the addition of TEOS, the clear solution became a white colloidal dispersion. After one hour of stirring, the colloidal dispersion was poured inside an autoclave and kept closed for 24 hours at 100°C. The white powder as-obtained was separated by centrifugation and washed three times with a mixture 1:1 in volume of water: ethanol. After a night of drying at 70°C, the product was calcined at 550°C for 4 hours (heating rate of 5°C min^{-1}). Figure 4.3 portrays a schematic representation of the synthetic route followed to synthesize hexagonal micrometric mesostructured silica (MCM41) and hexagonal micrometric mesostructured silica in which hydrothermal treatment was employed (MCM41_Hyd). The synthetic details are reported in Table 4.3.

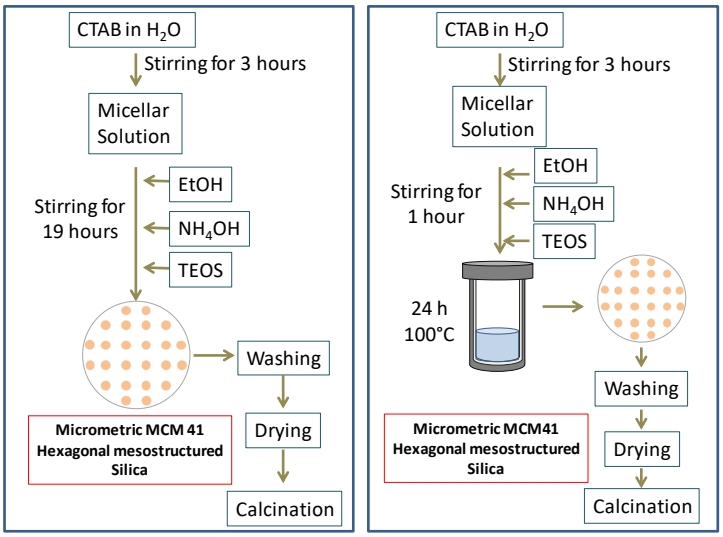

Figure 4.3 Schematic illustration of the synthetic route performed to obtain MCM41 and MCM41_Hyd silica supports

Sample	H_2O (mL)	CTAB (g)	EtOH (mL)	NH_4OH (mL)	TEOS (mL)	Solvothermal treatment (h)	Yield (%)
MCM41	200	1.01	87.4	21	3.79	-	90
MCM41_Hyd	200	1.01	87.4	21	3.79	24	87

Table 4.3 Synthesis detail of the samples MCM41 and MCM41_Hyd

4.2.2.2 Characterization of hexagonal (*P6mm*) mesostructured silica particles under hydrothermal restructuring

The effect of hydrothermal treatment is clearly visible by direct comparison of the corresponding MCM41. The presence in the LA-XRD patterns (Figure 4.4a) of three well-defined reflections can be attributed to a long-range of ordered hexagonal pores (space group *P6mm*). A shift in reflections toward low angles is observed in MCM41_Hyd, suggesting an increase in the value of cell parameter (Figure 4.4a). *d*-spacing calculated for the most intense (100) reflex and cell parameter (a_0) values are reported in Table 4.4.

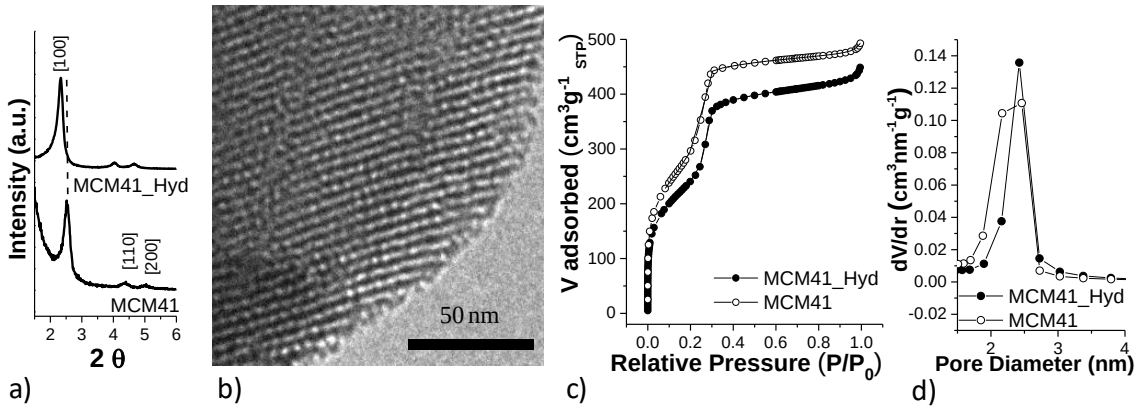

Figure 4.4 LA-XRD of the samples MCM41 and MCM41_Hyd (a). Bright field TEM images of MCM41_Hyd (b). N_2 adsorption-desorption isotherms (c) and pore size distributions (d) of the samples MCM41_Hyd.

Figure 4.4b reports a representative TEM image of the sample MCM41_Hyd, confirming the well-defined porous order in which aligned silica walls are separated by well-defined and uniform pores. Pore dimension and silica wall have been estimated once again to be about 2 nm.

N_2 adsorption-desorption isotherms recorded in the samples MCM41 and MCM41_Hyd are reported in Figure 4.4c. The resulting curves appear very similar and classifiable as IVB type, showing a capillary condensation at 0.3-0.4 P/P_0. It is worth noting that the isotherm of the MCM41 sample reaches a higher value of volume adsorbed than MCM41_Hyd, suggesting a higher total pore volume. Table 4.4 reports the textural parameters of the two supports. As expected, the pore volume of MCM41_Hyd is lower than the value of the MCM41 sample, as well as the surface area results to be lower of about 25%. These results can be explained by

considering pore size distribution (PDS) (Figure 4.4d) and the subsequent wall thickness calculated by correlating pore size with lattice parameter. PSD of MCM41_Hyd is sharper and centred at higher pore diameter values (2.4 nm for MCM41_Hyd and 2.2 nm for MCM41) and the silica walls of the MCM41_Hyd sample support result to be thicker than in the case of MCM41. Therefore, the decrease in pore volume and surface area is related to the increase of pore diameter and to the thickening of silica walls caused by hydrothermal treatment.

Sample	S_{BET} (m^2g^{-1})	V_p (cm^3g^{-1})	D_{pore} (nm)	w_t (nm)	d_{100} (nm)	a_0 (nm)
MCM41	1063	0.76	2.2	1.7	3.5	4.0
MCM41_Hyd	877	0.69	2.4	2.0	3.8	4.4

Table 4.4 Textural features obtained by N_2-physisortion data for MCM41 and MCM41_Hyd samples. S_{BET}=surface area, V_p= pore volume; D_p= pore diameter; W_t = wall thickness. Relative standard deviation: %RSD (S_{BET})=2.1%; %RSD(V_p)=1.1%; %RSD(D_p)=1.8%.*d*-Spacing (d_{100}) and lattice parameter (a_0) obtained from the LA-XRD data.

To summarize, according to our results hydrothermal treatment has caused a significant increase in walls thickness (from 1.7 to 2.0 nm) and an improvement in pores size distribution centred to higher pore diameters (2.4 nm). Furthermore, considering the higher intensity of the two small peaks [110] and [200] in the sample Hex_Hyd after hydrothermal treatment, improvements in mesoporous order might be supposed. However, the increase of pore size and wall thickness causes an inevitable decrease in surface area.

4.2.3 From microparticles to mesostructured silica nanoparticles

Beyond the control of the porous structure, considerable efforts have been made in the last decades into the design of suitable pathways able to improve particle size control and achieve uniform growth of particles down to the nanoscale. In this context, it is known that creating a burst of nuclei and their subsequent growth can produce uniform particles. It is desirable for these two steps to be completely separated because multiple nucleation events lead to a broad size distribution. In addition, aggregation of nanoparticles also affects final size distribution.[15] Many experimental factors control template-silica interactions, silica condensation, silica condensation rate, assembly kinetics and thus nucleation and growth. In 1968, Stöber *et al*. first discovered an effective method for the synthesis of monodispersed silica particles, which involves the hydrolysis and the condensation of tetraalkyl silicates in a mixture of alcohol and water using ammonia as catalyst.[16] Based on a Stöber-like approach, it has been possible to synthesize mesoporous silica nanoparticles of uniform size by modifying the composition of the reaction mixture. Grun *et al*. first modified Stöber synthesis composition by addition of a cationic surfactant to the reaction mixture and obtained the submicrometer-scaled MCM-41 spherical particles.[16] Subsequently, Nooney *et al*. used both

cationic surfactant (CTAB) and neutral surfactant (*n*-dodecylamine) as templates and showed that mesostructured silica nanoparticles, with a wide range of diameters from 65 to 740 nm, can be obtained by simply varying the surfactant/TEOS ratios under dilute conditions.[17] Beyond the Stöber-like approach, other strategies have been developed to decrease particle dimension. Using a steric stabilizer can reduce aggregation propensity among primary particles, inhibiting particle growth. These surface-protecting agents can be either non-ionic triblock copolymer (Pluronic® F127), polymer (PEG) or simple molecules as triethanolamine (TEA). Furthermore, ethyl acetate in aqueous solution was successfully employed by Wiesner and co-workers to reduce dimension of the particles up to the nanoscale range.[18] The role of ethyl acetate is hidden on its hydrolysis which caused the formation of ethanol, necessary to solubilize tetraethylortosilicate (TEOS), and acetic acid which causes a gradually decrease in the pH of the solution. The effect of pH has been already studied by different authors, who found that a lower pH led to smaller-sized mesoporous silica nanoparticles.[17]

4.2.3.1 Design of sub-micrometric and nanometric hexagonal (*P6mm*) mesostructured silica

Among the synthetic strategies proposed in the literature to obtain mesostructure sub-micrometric and nanometric silica particles, the Wiesner's approach was chosen because of its simplicity and the use of water as a unique solvent. Then, temperature and concentration were monitored to verify their possible effects. Figure 4.5 portrays the synthetic routes followed to synthesize sub-micrometric and nanometric hexagonal silica particles. Typically, an aqueous solution containing a certain amount of CTAB (see Table 4.5) was stirred (300 rpm) for 3 hours, then ammonium hydroxide and ethyl acetate were subsequently added. After 5 minutes, stirring speed was increased to 600 rpm, and TEOS was quickly added. The resulting opalescent dispersion was kept under mild stirring (300 rpm) for 3 hours. Separation, washing, drying, and calcination were performed as reported for the MCM41 sample. Synthetic details are reported in Table 4.5.

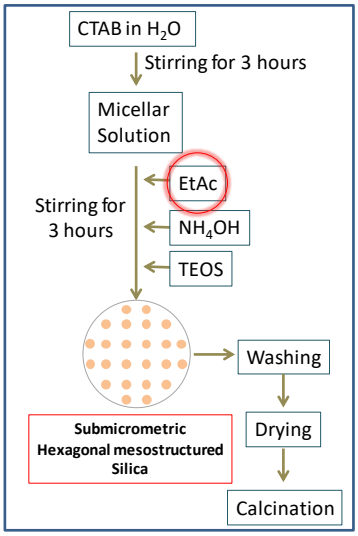

Figure 4.5 Schematic illustration of the synthetic route performed to obtain sub micrometric and nanometric hexagonal mesostructured silica particles

Sample	Temperature (°C)	H_2O (mL)	CTAB (g)	NH_4OH (mL)	EtAc (mL)	TEOS (mL)	Yield (%)
Hex_Nano_30_1	30	600	0.6	18	**3**	3	47
Hex_Nano_30_2	30	600	0.6	18	1.5	3	50
Hex_Nano_40	**40**	600	0.6	18	1.5	3	62
Hex_SubMicro	30	600	2.4	72	6	12	73

Table 4.5 Synthesis details of the samples Hex_Nano_30_1, Hex_Nano_30_2, Hex_Nano_40 and Hex_SubMicro

4.2.3.2 Characterization of sub-micrometric and nanometric hexagonal (*P6mm*) mesostructured silica

Besides the usual characterization (LA-XRD, TEM, and N_2-physisoprtion), particles size and particles size distribution were also determined by dynamic light scattering (DLS), given the stability of sub-micrometric and nanometric silica particles in water.

Figure 4.6 reports the LA-XRD patterns of the calcined nanometric (Hex_Nano_30_1, Hex_Nano_30_2, Hex_Nano_40) and sub-micrometric (Hex_SubMicro) samples. All the samples show three reflections confirming the long-range order typical of a hexagonal pore structure (space group *P6mm*). *d*-spacing (d_{100}) and cell parameter (a_0) have been calculated and reported in Table 4.7.

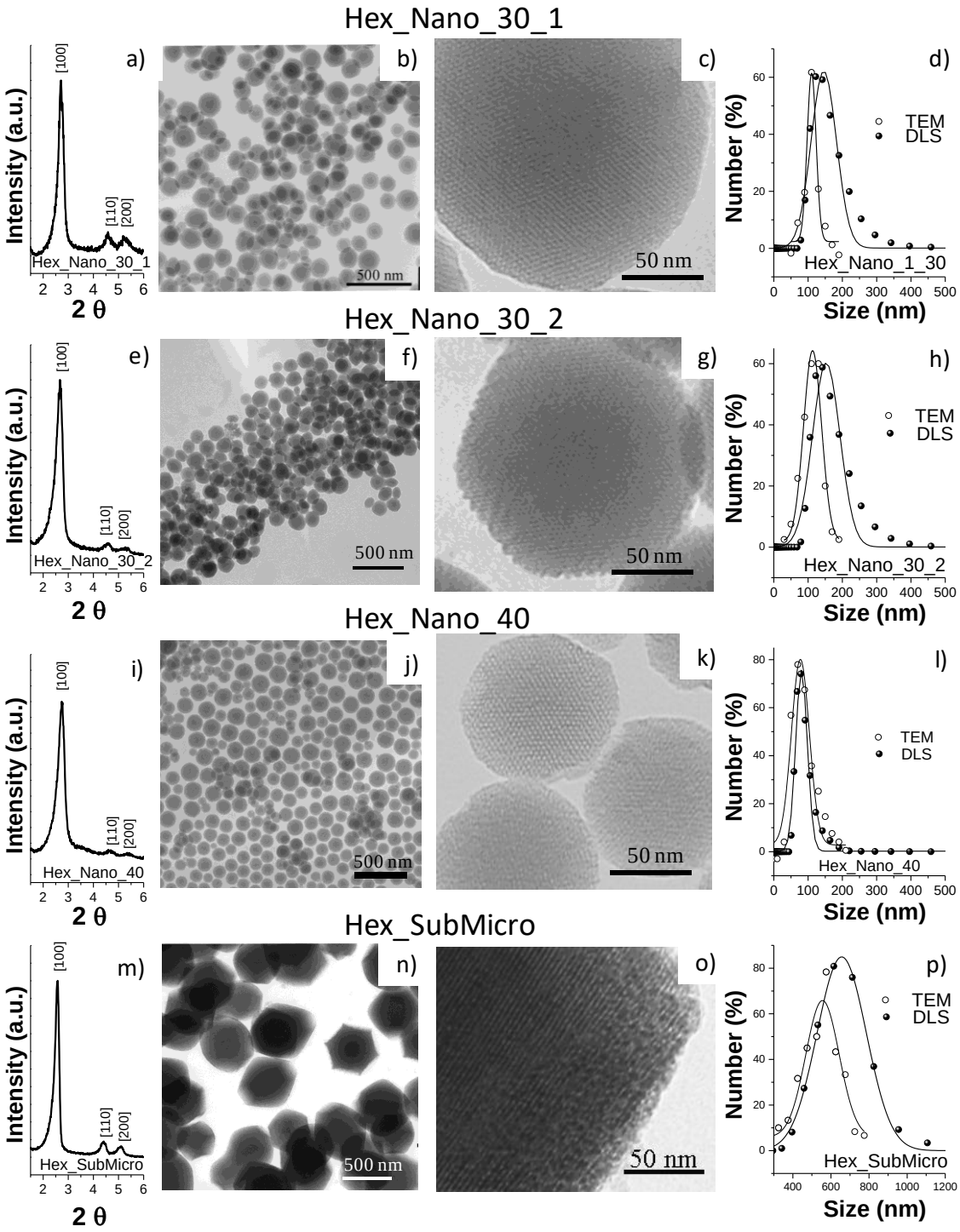

Figure 4.6 LA-XRD patterns of the samples, bright field images at different magnification and hydrodynamic particles size distribution of Hex_Nano_30_1 (a, b, c, d), Hex_Nano_30_2 (e, f, g, h), Hex_Nano_40 (i, j, k, l) and HexSubMicro (m, n, o, p)

TEM and DLS analyses allow to study the effect of different experimental conditions on particle size. Table 4.6 lists the average particles sizes, their related standard deviations, and the dispersity values obtained with TEM and DLS. The results obtained by TEM and DLS are in good agreement with hydrodynamic diameter always higher than the particles diameter, as

expected. It can be observed that effective formation of nanoparticles is achieved following the Wiesner's strategy (Hex_Nano_30_1), mainly due to the use of ethyl acetate in aqueous solution (Figure 4.6a). TEM images show spherical particles of about 110 nm with a slight tendency to hexagonal shape. The high degree of pore order is confirmed by high magnification TEM image (Figure 4.6b), that highlights the retention of the porous structure even on the surface of the nanoparticles, with average pore size and wall thickness of about 2 nm. Reduction in the amount of used ethyl acetate does not seem to exert any effect on particle dimension (Hex_Nano_30_2), being both TEM and DLS particle size distributions of the two samples centred at very similar values (see Table 4.6). TEM images confirm the similarities both in size and shape (Figure 4.6f). Increasing temperature, from 30 °C to 40 °C (Hex_Nano_40), has led to very interesting results due to a remarkable reduction in particle size (from around 150 nm to 82 nm), a narrowing in particle size distribution (from *Đ*~30 to *Đ*~20%) as well as to an increase in reaction yield from 47% to 62%. TEM images show spherical particles and high porous order in the whole particle (Figure 4.6k). Moreover, the effect of the increase in concentration of the reactants, 4 times higher than in the reference synthesis (Hex_Nano_30_1), causes an expected increase in particle dimension (Hex_SubMicro) from about 150 nm to about 660 nm, maintaining dispersity constant (about 30%) along with a good reaction yield (73%). TEM analysis highlights the presence of hexagonal shaped particles with well-defined porous structure (Figure 4.6 o).

Sample	particles size TEM (nm)	Standard Deviation TEM (nm)	Đ (%)	particles size DLS (nm)	Standard Deviation DLS (nm)	Đ (%)
Hex_Nano_30_1	112	28	25	150	45	30
Hex_Nano_30_1	111	25	22	158	50	32
Hex_Nano_40	76	24	31	82	16	20
Hex_SubMicro	607	110	18	664	195	29

Table 4.6 Particles size determined by TEM images and DLS , corespesponding standard deviation and dispersity Đ (%) of the samples Hex_Nano_30_1, Hex_Nano_30_2, Hex_Nano_40 and Hex_SubMicro

Figure 4.7a, b reports the N_2 adsorption-desorption isotherms and the pore size distribution of the three nanometric samples Hex_Nano_30_1, Hex_Nano_30_2 and Hex_Nano_40, while Figure 4.7c, d depicts the comparison between the N_2 adsorption-desorption isotherms and the pore size distributions of the samples Hex_SubMicro and Hex_Nano_30_1. All the samples show characteristic IVB type behaviour with a well-defined step in the 0.2-0.3 P/P_0 range as a consequence of capillary condensation. Moreover, a further condensation step at above 0.90 P/P_0, ascribable to interparticle voids, was found in the case of the nanometric samples, which

indirectly reflects the small particles size. Pore size distribution (Figure 4.7b and Figure 4.7d), calculated from the desorption branch (BJH method), are centred at 2-2.5 nm and confirmed by TEM imaging. The textural parameters of the different samples are listed in Table 4.7.

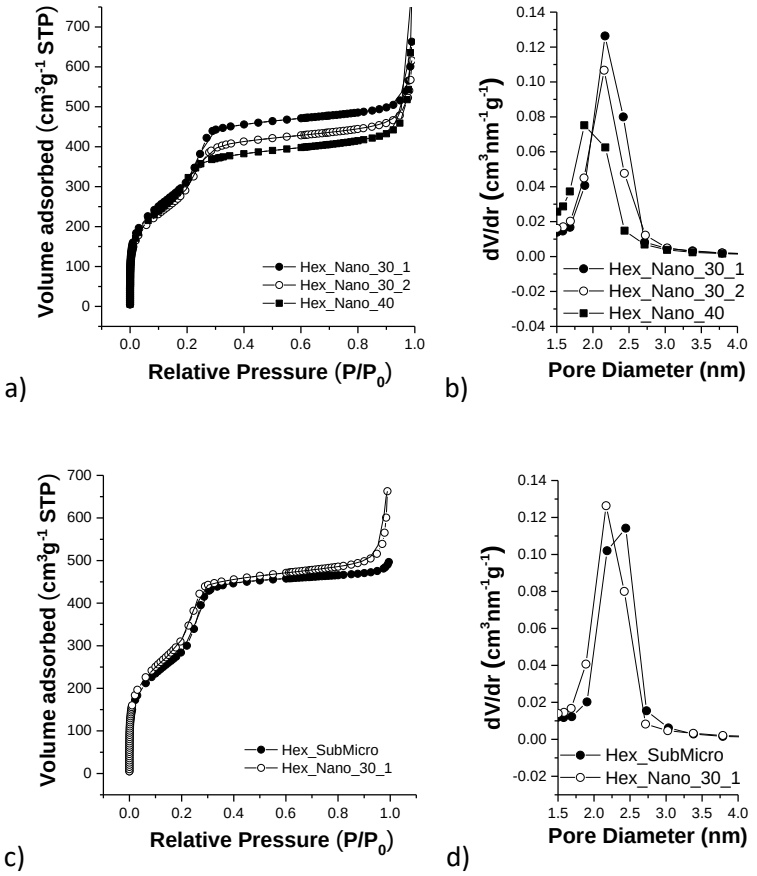

Figure 4.7 N_2 adsorption-desorption isotherms and pore size distributions of the nanometric samples Hex_Nano30_2 and Hex_Nano_40 (a, b) and the sub micrometric Hex_SubMicro and nanometric Hex_Nano_30_1 (c, d).

Sample	particles size TEM (nm)	S_{BET} (m^2g^{-1})	V_p (cm^3g^{-1})	D_{pore} (nm)	w_t (nm)	d_{100} (nm)	a_0 (nm)
Hex_Nano_30_1	112	1215	0.78	2.2	1.6	3.25	3.8
Hex_Nano_30_2	111	1248	0.80	2.2	1.7	3.31	3.8
Hex_Nano_40	76	1233	0.81	2.1	1.6	3.22	3.7
Hex_SubMicro	607	1139	0.77	2.3	1.7	3.43	4.0

Table 4.7 Textural features obtained by N_2-physisortion data for Hex_Nano_30_1, Hex_Nano_30_2, Hex_Nano_40 and Hex_SubMicro samples. S_{BET}=surface area, V_p= pore volume; D_p= pore diameter; w_t= wall thickness. Relative standard deviation: %RSD (S_{BET})=2.1%; %RSD(V_p)=1.1%; %RSD(D_p)=1.8%. *d*-Spacing (d_{100}) and lattice parameter (a_0) obtained from the LA-XRD data

4.2.3.3 Design of sub-micrometric and nanometric cubic (*Ia3d*) mesostructured silica

To obtain sub-micrometric and nanometric cubic mesostructured silica, Pluronic® F127 was used as co-template with CTAB.[19] Pluronic F127 has a dual role: on one hand the co-template allows to obtain bicontinuos porous structure, on the other it works as a growth inhibitor with which sub-micrometric and nanometric particles can be obtained. Typically, the proper amount of Pluronic F127 is added in the CTAB aqueous solution and kept under stirring (300 rpm) for three hours. The subsequence steps were carried out following the procedure described in paragraph 3.2 for MCM41 sample. Based on the same synthetic route of the Cub_1 sample, time reaction has been increased threefold. Table 4.8 reports the synthesis details and Figure 4.8 a schematic illustration of the synthetic routes.

Sample	Temperature (°C)	H_2O (mL)	CTAB (g)	F127 (g)	EtOH (mL)	NH_4OH (mL)	TEOS (mL)	Time (h)	Yield (%)
Cub_1	30	200	1	6.45	87.4	21	3.79	19	57
Cub_2	30	200	1	6.45	87.4	21	3.79	57	65

Table 4.8 Synthesis details of the samples Cub_1 and Cub_2

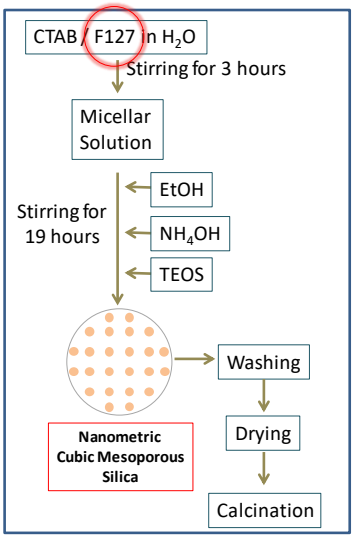

Figure 4.8 Schematic illustration of the synthetic route performed to obtain micrometric hexagonal mesostructured silica particles and nanometric cubic mesostructured silica particles

The addition of the Pluronic F127 to the procedure used for hexagonal micrometric particles causes an evident reduction in reaction yield from 90% to 50%. This finding can be explained by considering that part of the silica particles tends to be so stable in the reaction solution that centrifugation is not sufficient to separate them from the washing solution. TEM analysis performed on the washing solution confirms this finding, showing small nanoparticles of about

10-30 nm (Figure 4.9a, b, c) accompanied by larger spherical particles which seem to be hollow (see Figure 4.9c). These features may justify their high stability in the washing solution.

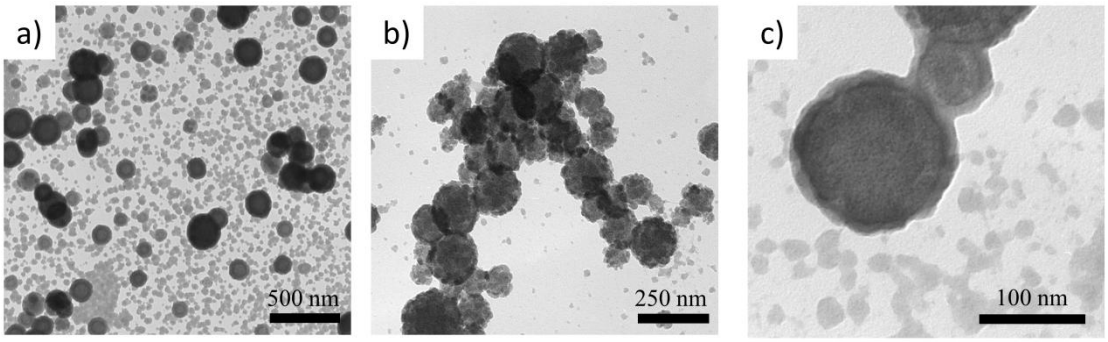

Figure 4.9 Bright field images at different magnification of the Cub_Nano_1 washing solution

An increase in reaction time from 19 hours to 57 hours (three times more) causes an improvement of yield (from 57 % to 65 %), probably due to the growth of the particles.

4.2.3.4 Characterization of sub-micrometric and nanometric cubic (*Ia3d*) mesostructured silica

LA-XRD patterns confirm the presence of a well-defined cubic porous structure (*Ia3d*), as confirmed by the spectra in Figure 4.10d, h (Cub_1 and Cub_2)

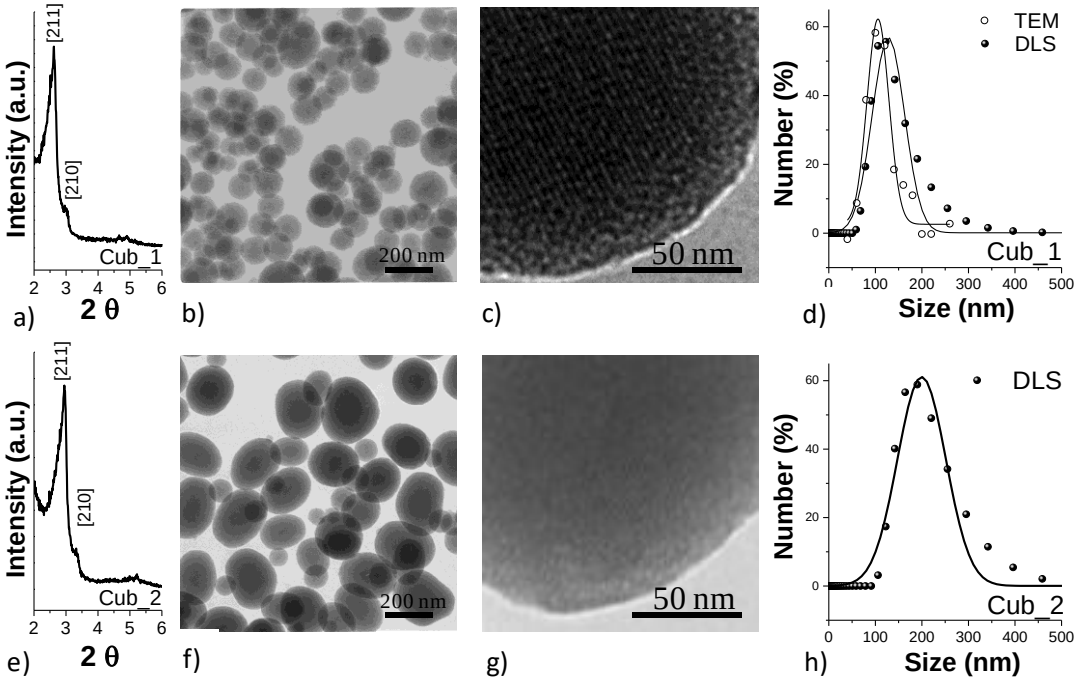

Figure 4.10 LA-XRD, bright field images at different magnification, TEM and hydrodynamic particles size distribution of Cub_ 1(a, b, c, d) and Cub_ 2 (e, f, g, h)

TEM images of Cub_1 shows the presence of spherical nanoparticles centred at about 108 nm with a dispersity value of about 25 %. (Figure 4.10c). The effect of addition of Pluronic® F127 causes an expected reduction in the dimension of the particles (Figure 4.10e). DLS measurements confirm the formation of particles reduced in size, consistent with TEM data. The obtained results and the corresponding standard deviations are reported in Table 4.9. High magnification images has allowed to confirm the presence of well-ordered porous structure, that seems to be lost in proximity of the surface of the particles, probably due to the interaction between the block copolymer with the silanol groups silica, as suggested by some authors[20] and schematically represented in Figure 4.11.

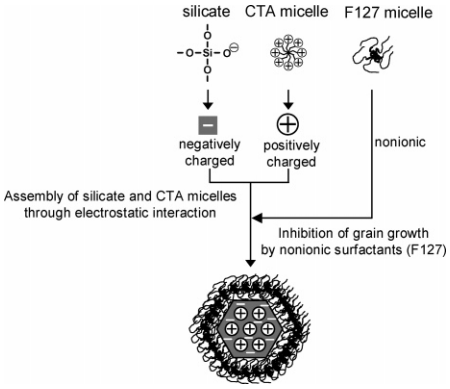

Figure 4.11 Schematic representation of the function of the two surfactant for assembly of the mesostructure. Reprinted with permission from ([20]). Copyright (2006) American Chemical Society

Some of these effects are observed in the TEM images of the sample Cub_2, in which reaction time was increased up to 57 hours. Together with spherical particles of about 100 nm (a similar value was also found also for the sample Cub_1), it is possible to observe bigger elongated particles with narrower diameter of about 200 nm and larger diameter 250 nm (Figure 4.12a). Therefore, it seems that, by increasing time, some of the particles start to grow assuming an anisometric shape. High magnification TEM image (Figure 4.10g) shows a high level of porous order spread all over the particles.

Sample	particles size TEM (nm)	Standard Deviation TEM (nm)	Đ (%)	particles size DLS (nm)	Standard Deviation DLS (nm)	Đ (%)
Cub_1	108	24	22	134	49	36
Cub_2	161	60	37	205	66	32

Table 4.9 Diameter and related standard deviation of different samples estimated by manual counting from TEM images and DLS.

Figure 4.12b and 12c reports the nitrogen adsorption-desorption isotherms and the pore size distribution (PSD), for Cub_1 and Cub_2. For both samples, as expected, IVB type isotherm behaviour was observed.

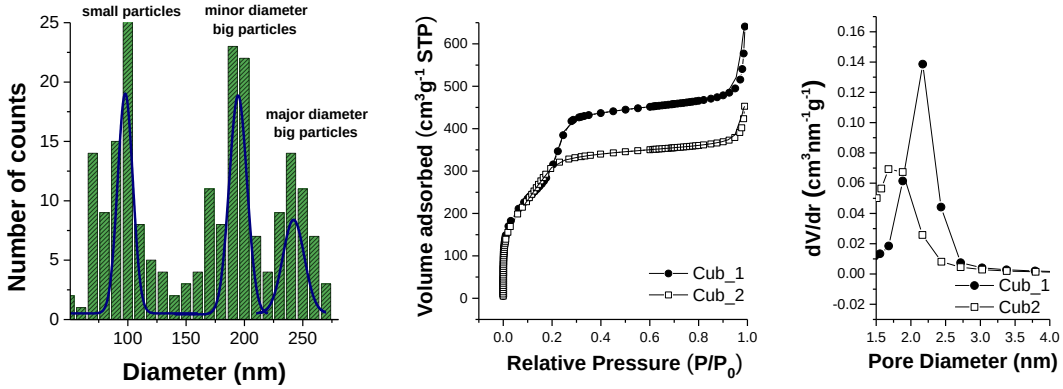

Figure 4.12 Particles size distribution obtained by manual counting on TEM images of the sample Cub_2(a) N_2 adsorption-desorption isotherms (b) and pore size distributions (c) of the Cub_1 and Cub_2 samples

Textural parameters are reported in Table 4.10. In spite of the difference in the morphology, similar values of surface area and wall thickness were observed. The most important difference are found in D_{pore} and PDS. Increasing reaction time induced a reduction (in) pore size and a broadening of PSD (Figure 4.12c).

Sample	S_{BET} (m^2g^{-1})	V_p (cm^3g^{-1})	D_{pore} (nm)	w_t (nm)	d_{100} (nm)	a_0 (nm)
Cub_1	1088	0.73	2.2	1.5	3.3	8.2
Cub_2	1195	0.58	1.8	1.5	3.0	7.3

Table 4.10 Textural features obtained by N_2-physisortion data for Cub_1 and Cub_2 samples. S_{BET} = surface area, V_p= pore volume; D_p= pore diameter; w_t= wall thickness. Relative standard deviation: %RSD (S_{BET})=2.1%; %RSD(V_p)=1.1%; %RSD(D_p)=1.8%.*d*-Spacing (d_{100}) and lattice parameter (a_0) obtained from LA-XRD diffraction data

The effect of F127 can be better understood when these results are compared with those obtained in the micrometric hexagonal structure, which differs from the other two synthetic strategies simply by the addition of the copolymer (Figure 4.8). The consequences of the addiction of F127 can be summarize as followed:

- Changing of the pore structure from hexagonal to cubic retaining similar surface areas (Table 4.11).
- Remarkable reduction in particles size from micrometric to nanometric scale
- Partial loss of the pore structure approaching the surface of the particles. (Figure 4.13c)

- Decrease in wall thickness, while preserving the same pore dimension (Figure 4.13c and Table 4.11)

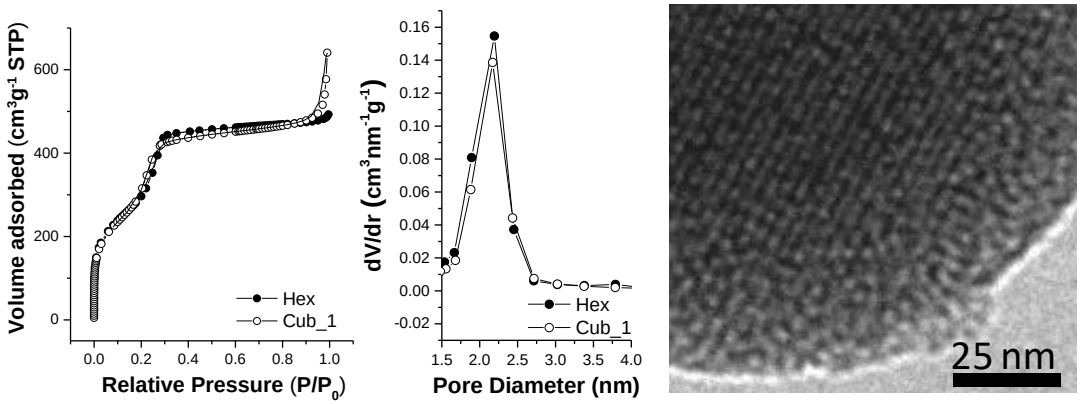

Figure 4.13 N_2 adsorption-desorption isotherms (a) and pore size distributions (b) of the samples MCM41 and Cub_1. TEM image showing the particles surface of the sample Cub_1

Sample	S_{BET} (m^2g^{-1})	V_p (cm^3g^{-1})	D_{pore} (nm)	w_t (nm)	d_{100} (nm)	a_0 (nm)
MCM41	1063	0.76	2.3	1.7	3.5	4.0
Cub_1	1088	0.73	2.2	1.5	3.3	8.2

Table 4.11 Textural features obtained by N_2-physisortion data for the MCM41 and Cub_1 samples. S_{BET} = surface area, V_p= pore volume; D_p= pore diameter; w_t= wall thickness. Relative standard deviation: %RSD (S_{BET})=2.1%; %RSD(V_p)=1.1%; %RSD(D_p)=1.8%.*d*-Spacing (d_{100}) and lattice parameter (a_0) obtained from the LA-XRD data

4.3 Design of non-siliceous mesostructured titania supports

Since the discovery of ordered mesoporous siliceous materials, great efforts have been made to replicate the fascinating results obtained for siliceous materials in the field of non-siliceous metal oxides. The development of new synthetic strategies, as evaporation-induced self-assembly (EISA), in combination with new robust block copolymers, represented the starting point to set up new approaches to fabricate mesostructured non-siliceous metal oxide.[21] Different synthetic routes have been proposed in the last two decades with the aim to obtain ordered mesoporous TiO_2 with highly crystalline framework.[22–25] Among them, the great majority, based on the use of commercial template (CTAB and Pluronic® P123), lead to mesostructured titania which starts to collapse when approaching crystallization temperature. To overcome this issue, two main strategies have been recently proposed: the Combined Assembly of Soft and Hard template method (CASH)[26], with the intrinsic necessity to use laboratory made copolymers with sp^2-hybridized carbon and the acid carbonization method, in which the use of a commercial Pluronic® comes with the use of sulphuric acid.[27] Being aware that the porous ordered of the metal oxide and its thermal stability are strictly related to the

selected block copolymers, we have decided to explore this field, starting from the use of the a commercial tri-block Pluronic® copolymer using the acid carbonization method and then moving to the use of CASH method with unconventional laboratory made block copolymers (PEO-b-Lignin and PEO-b-PVP) (see Figure 4.14).

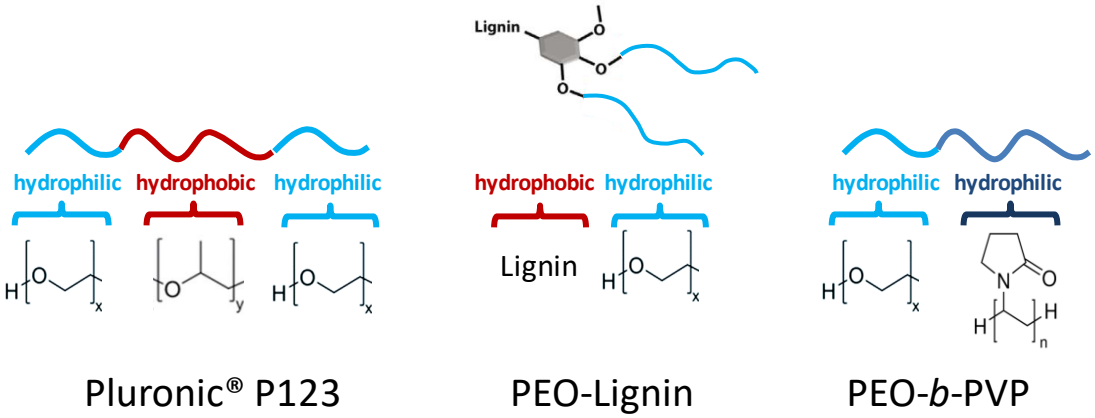

Figure 4.14 Representation of the three block copolymers used to synthesize mesostructured crystalline titania. Adapted from Lignin-based polymeric surfactants for emulsion polymerization, 112, Bernhard V.K.J. Schmidt, Valerio Molinari, Davide Esposito, Klaus Tauer, Markus Antonietti, 418, 426. Copyright (2017), with permission from Elsevier

4.3.1 Synthesis of mesoporous TiO_2 with a commercial tri-block copolymer (Pluronic® P123)

Following the acid carbonization approach proposed by Zhao,[27] 0.5 g of Pluronic® P123 ($PEO_{20}PPO_{70}PEO_{20}$ AMW=5800) was dissolved in 15 g of absolute ethanol (EtOH), 0.7 g of HCl 37 wt% and 0.23 g of H_2SO_4 44 wt% under vigorous magnetic stirring, and heated at 40°C for 3 hours. Then, 1.5 g of titanium isopropoxide (TIPO) was added and left for further 20 hours at the same temperature. The corresponding sol was poured into a Petri dish and evaporated for two days at 40 °C in air under 50-60 % relative humidity, and the resultant film was aged at 100°C for further two days. The product thus obtained was firstly treated at different temperature (350, 450, 500°C, heating rate 1°C min^{-1}) under N_2 atmosphere for 3 hours, and subsequently calcined at different temperature, from 360°C to 450 °C (heating rate 2°C min^{-1}) under air for 3 hours (see Figure 4.15). It is worth mentioning that the sample shows a black colour after nitrogen thermal treatment, suggesting the formation of the amorphous carbon scaffold. Conversly, after calcination, it features a light yellow colour.

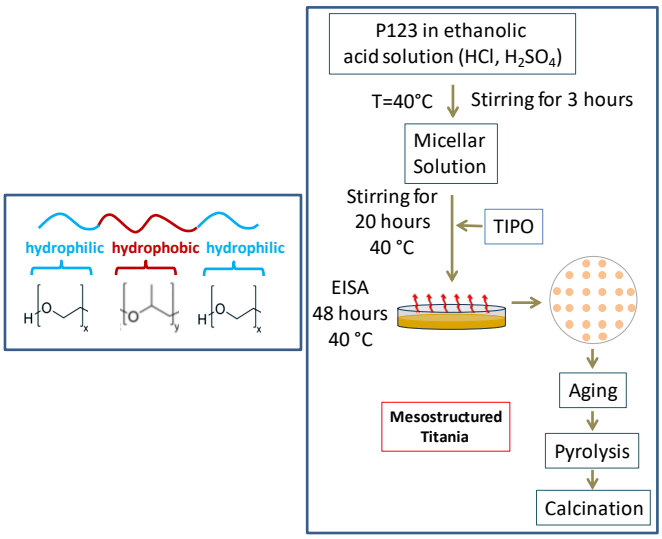

Figure 4.15 Schematic illustration of the synthetic route performed to obtain mesostructured titania by Pluronic P123

4.3.2 Characterization of mesoporous TiO_2 obtained with a commercial tri-block copolymer (Pluronic® P123)

A multi-technique approach based on the use of low angle X-ray diffraction (LA-XRD), transmission electron microscopy (TEM), wide angle X-ray diffraction (WA-XRD), and N_2-physisorption have been carried out on the sample after pyrolysis and calcination. In order to study the porous structure stability at different temperatures, different nitrogen treatments have been tested and the features of the porous structure have been monitored with LA-XRD.

Figure 4.16a reports LA-XRD patterns recorded on different portions of the sample treated under a N_2 flow at 350 °C, 450 °C and 550 °C (TiO_2_$350N_2$, TiO_2_$450N_2$ and TiO_2_$550N_2$, respectively) with heating rate 1°C min^{-1}. TiO_2_$350N_2$, TiO_2_$450N_2$ patterns show the presence of an intense reflex centred at 1.02° (2θ), clearly indicating the presence of ordered pores, that can be indexed and ascribed, according to the literature,[27] to a hexagonal structure with space group *p6mm*. A very broad reflex has been detected on TiO_2_$550N_2$, suggesting an almost complete collapse of porous structure.

WA-XRD patterns (Figure 4.16 b) point out the crystallization of titania in the form of nanostructured anatase starting from the treatment at 350°C in nitrogen, and a gradual evolution toward highly crystalline anatase with an increase in the temperature. Among these three samples, the TiO_2_$450N_2$ were selected for a further characterization due to the retention of the porous structure, as well as the good degree of crystallinity in the sample.

Figure 4.16 c, d report representative TEM images of the sample TiO_2_$450N_2$ in which is possible to confirm the presence of the long-range ordered porous structure, made up of pores of almost 6 nm and titania walls of almost 4 nm.

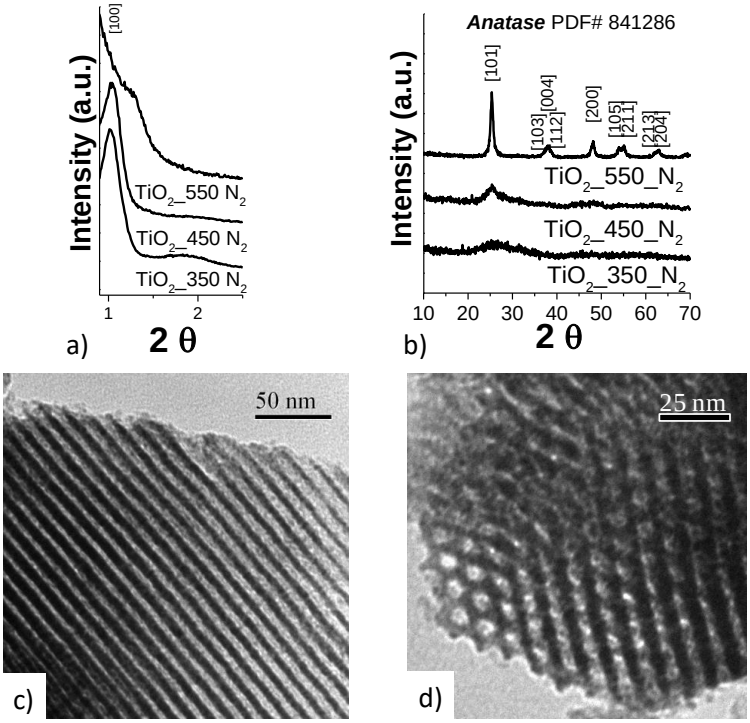

Figure 4.16 LA-XRD and WA-XRD patters patterns of TiO_2 samples after different pyrolysis (a, b), TEM images at different magnifications of the sample TiO_2_$450N_2$ (c, d)

After pyrolysis at 450 °C, the sample was treated at different calcination temperatures, 360 °C, 400 °C and 450 °C, (TiO_2_$450N_2$_$360O_2$, TiO_2_$450N_2$_$400O_2$ TiO_2_$450N_2$_$450O_2$) to remove the carbonaceous residues and obtain pure mesostructured anatase. Calcination at 360 °C improves titania crystallinity (Figure 4.17b) and does not induce the collapse of the porous structure (Figure 4.17a), even when a contraction of the cell is clear visible from the shift in the main reflexion toward higher 2θ values. The presence of anatase as a single crystalline phase (space group *I4₁* PDF card N. 084-1286) was detected, and the mean crystalline grain ($<D_{XRD}>$) size, calculated with Scherrer equation on the most intense X-ray peaks ([101] [200] [105]), was estimated to be 4.3 ± 0.5 nm. treatments at higher temperature worsened textural properties up to the complete collapse of the porous structure at 450 °C (TiO_2_$450N_2$_$450O_2$).

The Representative TEM image in Figure 4.17c confirms the retention of the porous order after the calcination step in the whole analyzed portion of the sample. N_2 adsorption-desorption analysis (Figure 4.17d) shows an isotherm, classifiable as IVA type,[11] with a well-defined condensation at around 0.6 P/P_0 and a H1 type hysteresis loop, ascribable to material with a

narrow range of uniform mesopores. Textural parameters are reported in Table 4.12. As expected, high value of surface area and pore volume are observed (273 m^2g^{-1} and 0.3 cm^3g^{-1}, respectively). Pore size distribution (PSD) calculated by BJH method on the desorption branch confirms the presence of a sharp distribution of the pores, centred at 3.9 nm (Figure 4.17e). Wall thickness, calculated by correlating of cell parameter and pore size, result to be centred at 4.8 nm, rather similar to $<D_{XRD}>$ (4.3 nm ± 0.5 nm).

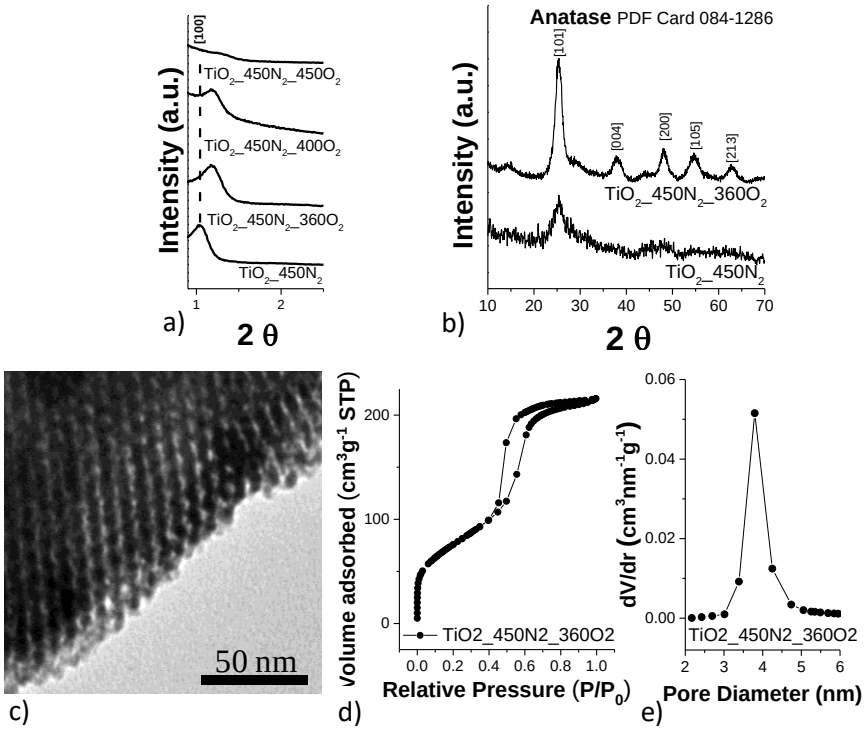

Figure 4.17 LA-XRD pattern and WA-XRD patterns (a, b), TEM image(c), N_2 adsorption-desorption isotherms (d) and pore size distributions (e) of the sample $TiO2\_450N_2\_360O_2$

Sample	S_{BET} (m^2g^{-1})	V_p (cm^3g^{-1})	D_{pore} (nm)	w_t (nm)	d_{100} (nm)	a_0 (nm)
$TiO_2\_450N_2\_360O_2$	274	0.3	3.9	4.8	7.5	8.7

Table 4.12 Textural features obtained by N_2-physisortion data for the $TiO_2\_450N_2\_360O_2$ sample. S_{BET}=surface area, V_p= pore volume; D_p= pore diameter; w_t= wall thickness. Relative standard deviation: %RSD (S_{BET})=2.1%; %RSD(V_p)=1.1%; %RSD(D_p)=1.8%. *d*-Spacing (d_{100}) and lattice parameter (a_0) obtained from the LA-XRD data

In summary, the synthetic pathway based on applying the acid carbonization method permits to obtain crystalline titania, in form of anatase, showing well-defined hexagonal (*p6mm*) porous structure and stability in air up to 360 °C. Since calcination needs a higher temperature (360°C) compared to the H_2S removal test (300 °C), this material can be proposed as support for Fe_2O_3-based sorbent.

4.3.3 Mesoporous TiO_2 by lab-made block copolymers

Laboratory-made block copolymers, usually synthesized through controlled living polymerization methods, such as atom transfer radical polymerization (ATRP), offer, by changing composition and volume fractions of each constituent block the possibility to control the pores size and the walls thickness of the corresponding inorganic framework. For these reasons the methods based on laboratory-made block copolymer represent a potential alternative to those based on commercial block copolymers. However, their utilization is limited by the main drawback deriving from the tedious synthesis of the polymers, which in the final step of the mesostructured metal oxide synthetic route, have to be burn out .

4.3.4 Mesoporous TiO_2 by Lignin-*b*-PEO

The most common laboratory-made amphiphilic block copolymers proposed to the CASH method in order to prepare titania, consist of an hydrophilic block, such as poly(ethylene oxide) (PEO), poly(2-vinylpyridine) (P2PV) or poly(4-vinylpyridine)(P4VP), and an hydrophobic block such as polystyrene (PS), polyisoprene (PI) or polybutadiene (PB) (Figure 4.18).

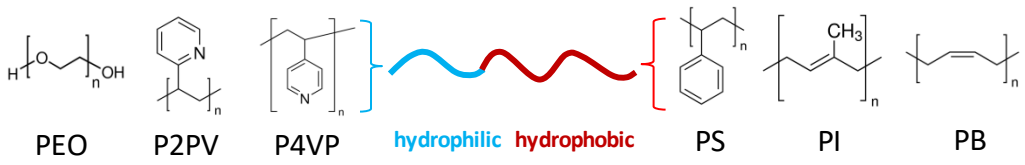

Figure 4.18 Different typologies of hydrophilic and hydrophobic block used to build block copolymers

In this context, lignin can be considered a valid alternative to the hydrophobic block usually employed, due to its high abundance in nature, inexpensiveness, and not too much health-interference.[28] Therefore, the generation of a new block copolymer in which lignin represents the hydrophobic segment, could be the first step toward the design a greener synthetic pathway to obtain siliceous and non-siliceous mesoporous metal oxide. The synthetic route employed to synthesize Lignin-*b*-PEO are reported in the cited article,[28] and is based on lignin-based precursors (Lignin) in the oxayanionic polymerization of ethylene oxide (EO).[28]

4.3.5 Synthesis of mesoporous TiO_2 by Lignin-*b*-PEO amphiphilic copolymer

Among the different attempts performed to create a mesophase with this new polymer by changing the ratio between the reactants, the most promising result is described as follows. Typically, 74 μl of acetic acid (AcAc), 23 μl of hydrochloric acid (HCl), 109 μl of titanium butoxide (TBO) were added in 3 mL of a solution of Lignin-*b*-PEO (50 mg) in tetrahydrofurane (THF) and kept under stirring for 3 hours at 40 °C. The resulting sol, poured into a Petri dish, was evaporated for 48 hours at 40 °C, aged at 80 °C for 12 hours, and submitted to pyrolysis at

450 °C for three hours with heating rate 1 °C min^{-1} (Figure 4.19). After the aging step, a thin brown film was obtained, while the pyrolysis leads the formation of a gray powder.

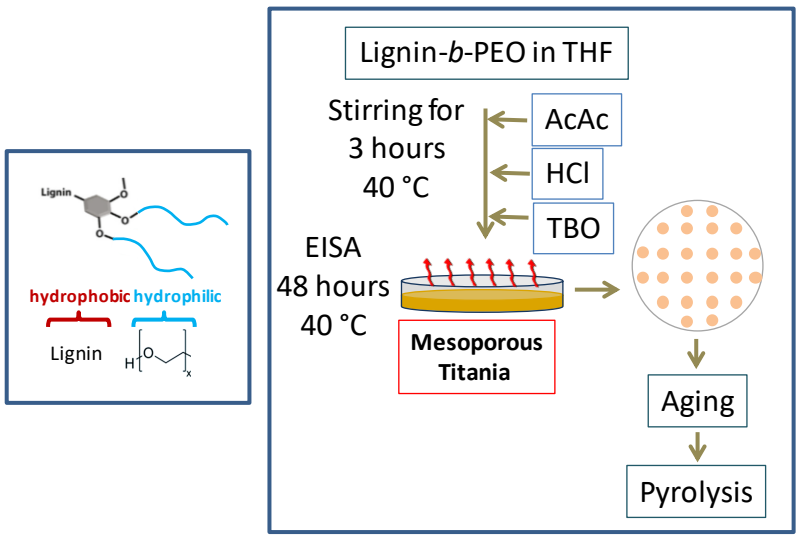

Figure 4.19 Schematic illustration of the synthetic route performed to obtain mesostructured titania by lignin-*b*-PEO block copolymer

4.3.6 Characterization of mesoporous TiO_2 by Lignin-*b*-PEO amphiphilic copolymer

Small angle X-ray scattering (SAXS) analysis on the film formed after aging (Figure 4.20a) evidences a large signal in the range 0.15 - 1 q^{-1}, suggesting the formation of a nanometric pore order with a wide distribution. This can be explained considering the wide molecular weight dispersity of the Lignin-*b*-PEO block copolymer due to the wide dispersity of the lignin fraction (Đ= 2.23). The following nitrogen thermal treatment at 450 °C induced the crystallization of titania in form of nanostructure anatase phase (<D_{XRD}> 9.3± 0.3 nm) (Figure 4.20c), accompanied by a loss of the porous structure (Figure 4.20b). Although porous order is not retained after the final treatment, these preliminary results can be considered promising and more efforts have to be done in the design of the EISA process to render possible the generation of mesostructured non-siliceous metal oxides with greener block copolymers.

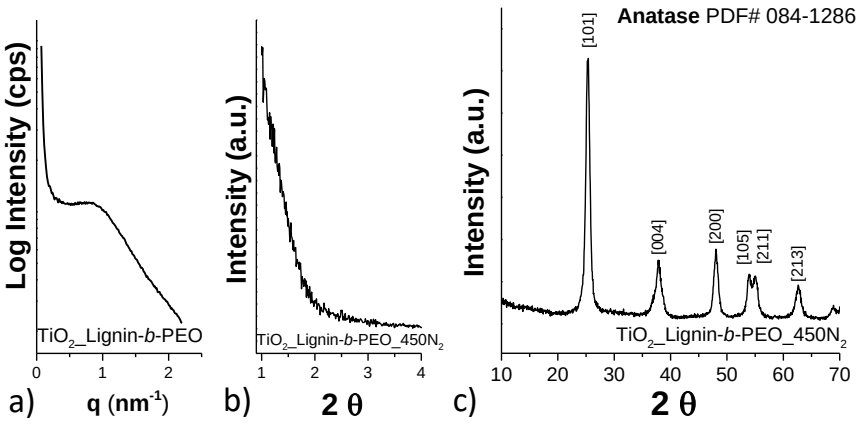

Figure 4.20 SAXS and LA-XRD patterns after aging at 80°C (a) and pyrolysis at 450°C (b) wide angle XRD of the sample after pyrolysis at 450 °C of the sample TiO_2_Lign-*b*-PEO

4.3.7 Mesoporous TiO_2 by double hydrophilic block copolymer (PEO-*b*-PVP)

So far, it has been proven that amphiphilic block copolymers can be used to obtain mesoporous siliceous and non-siliceous metal oxide. Here, the use of laboratory-made double hydrophilic block copolymer (DHBC) is proposed for the first time as alternative to the conventional amphiphilic one. DHBC are made up of two water-soluble blocks of different chemical nature, and in aqueous solution do not show the typical capabilities of an amphiphilic copolymers, such as micelle formation, or lowering of the surface tension.[29] The amphiphilicity can be induced as soon as the molecules come into contact with a proper solvent or a mixture of solvents, or more generally, with a substrate that can preferentially interact with one of the two blocks, generating a superstructure. Alternatively, temperature, ionic strength or pH variation, as well as complexation reactions, can completely reverse the hydrophilicity of a block into hydrophobicity.[29] Taking into consideration these theoretical aspects, titania sol was tentatively used as possible substrate to induce amphiphilitiy in the double hydrophilic copolymer, due to the theoretical formation of unconventional mesophases. Aware of the difficulties, different syntheses have been designed and described as follows.

4.3.8 Synthesis of mesoporous TiO_2 by PEO-*b*-PVP double hydrophilic copolymers

The first step to the design on the mesoporous titania with DHBC is the choice of the two building blocks of the copolymer. Poly(ethylene oxide) (PEO) and poly(N-vinylpyrrolidone) (PVP) were chosen as the two hydrophilic blocks, in which, according to the literature, PVP blocks should show a weak charge due to its protonation.[30] This fact could promote the interaction between the titania sol and the block copolymer.

The synthesis of block copolymer of PEO-*b*-PVP was conducted by using xanthantes as macro RAFT/MADIX chain transfer agents, as described in the cited article.[31] Two PEO-*b*-PVP block

copolymers with different molecular weight ratio (PEO-*b*-PVP 1:1 and PEO-*b*-PVP 1:2) and average molecular weight of 10 000 and 15 000 g mol^{-1} have been synthesized. Table 4.13 reports the molecular weight ratio, average molecular weight, and dispersity (*Đ*) of the two block copolymers.

Name	Molecular weight ratio (PEO : PVP)	$M_{n,\,app,\,SEC}$ ($gmol^{-1}$)	*Đ*
PEO-*b*-PVP_1	1:1	10325	1.17
PEO-*b*-PVP_2	1:2	14996	1.27

Table 4.13 PEO:PVP weight ratio, molecular weight obtain by size exclusion chromatography (SEC) and average weight dispersity (*Đ*) obtained in NMP using PEO calibration.

Thermo-gravimetric analysis (TGA) curves (Figure 4.21b) of the two block copolymers show their high thermal stability, even higher than the commercial P123 (Figure 4.21a). PEO-*b*-PVP polymers start to decompose at 370 °C in a single and sharp step up to 470 °C with a residual carbon of 7 % in weight, proving the potential utilization of these blocks in the synthesis of mesoporous crystalline TiO_2.

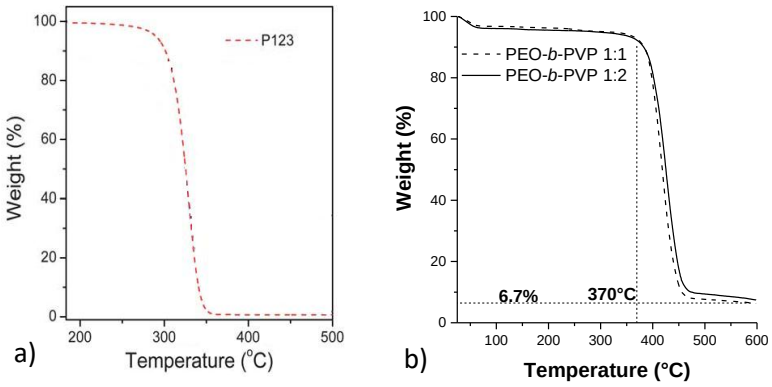

Figure 4.21 TGA of P123 (a) and double hydrophilic block copolymers PEO-*b*-PVP_1 and PEO-*b*-PVP_2 (b)

In a typical synthesis, a proper amount of HCl was added in an ethanolic solution of DHBC and left under magnetic stirring at room temperature for three hours. An apt amount of titanium butoxide (TBO) was then added and the resulting sol kept under mild stirring (300 rpm) for 40 hours at 40°C. The solution was poured in a Petri dish, evaporated at 40°C for 48 hours, and aged at the same temperature for further two days. The yellow film obtained was submitted to pyrolysis at 550°C for 3 hours (heating rate 1°C·min^{-1}) and calcination at 450°C for 2 hours (heating rate 1°C·min^{-1}). Several syntheses have been performed changing various parameters, such as the ratio between titania precursor, block copolymer, HCl, and solvent. Figure 4.22 reports a schematic illustration of the synthetic procedure, whereas Table 4.14 provides the

synthetic details of three most promising synthesis in terms of textural properties and porous order.

Sample	DHBC	EtOH (mL)	DHBC (mg)	HCl (µL)	TBO (µL)
TiO_2_DHBC_1	PEO-*b*-PVP_1	6	50	92	436
TiO_2_DHBC_2	PEO-*b*-PVP_2	6	100	46	218
TiO_2_DHBC_3	PEO-*b*-PVP_2	6	50	92	436

Table 4.14 Synthesis details of the samples TiO_2_DHBC_1, TiO_2_DHBC_2, TiO_2_DHBC_3

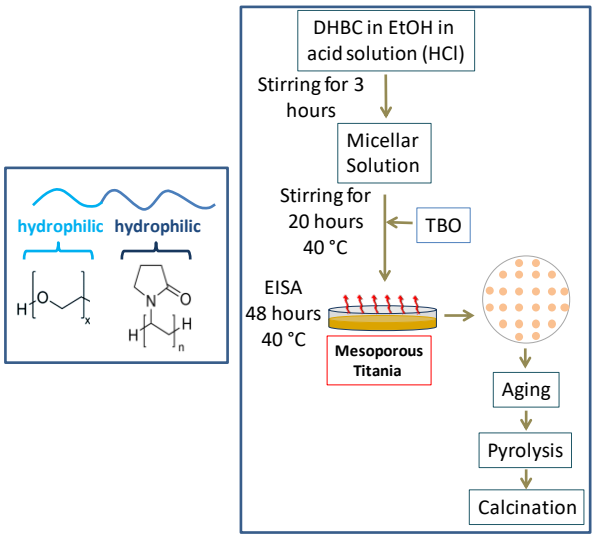

Figure 4.22 Schematic illustration of the synthetic route performed to obtain mesostructured titania by DHBC

4.3.9 Characterization of mesoporous TiO_2 by PEO-*b*-PVP double hydrophilic copolymers

WA-XRD patterns (Figure 4.23a) of the three calcinated samples (TiO_2_DHBC_1, TiO_2_DHBC_2 TiO_2_DHBC_3) show the presence of an unique nanostructured anatase phase (space group $I4_1$ PDF card N. 084-1286), and the obtained $<D_{XRD}>$ values are reported in Table 4.15. The use of DHBC with shorter PVP block (sample TiO_2_DHBC_1) leads to the formation of slightly smaller anatase crystallites (8.1 ± 0.4 nm) than those obtained using PEO-*b*-PVP_2, regardless of the ratio TiO2:PEO-*b*-PVP_2 (8.8 ±0.4 and 9.1 ±0.4). Therefore, it can be hypothesized that crystal dimension might be related to the dimension of the PVP block, suggesting a preferential interaction between the titania sol and the PVP block.

SAXS patterns (Figure 4.23b) of the same three samples (TiO_2_DHBC_1, TiO_2_DHBC_2 and TiO_2_DHBC_3) point out the presence of a nanometric porous order only in the case of the sample TiO_2_DHBC_1, while in the other two cases, only a broad reflex was detected.

N_2 adsorption-desorption isotherms of the three samples are reported in Figure 4.23c. The three isotherms can be classified as IVA type due to the well-defined condensation at around 0.6 P/P0 and the consequential presence of the hysteresis loop, classifiable in the case of TiO_2_DHBC_1 and TiO_2_DHBC_2 sample as H2(a), while in TiO_2_DHBC_3 sample as H5.[11] Therefore, pore blocking *phenomena* in the first two cases cannot be excluded, while both open and partially blocked mesopores can be assumed to be present in the latter case.[11] Surface area and pore size distribution of the three samples are reported in Table 4.15. TiO_2_DHBC_2 shows the highest value of surface area (167 m^2g^{-1}), while for the other two samples similar values of about 100 m^2g^{-1} are observed. The higher value can be explained by considering the higher amount of block copolymer used in this synthesis when compared to the others. Pore size distribution (PSD) was calculated by DFT silica cylindrical model on the adsorption branch (Figure 4.23d), due to the pore blocking *phenomena* on the desorption branch. The average values reported in Table 4.15. The sample TiO_2_DHBC_2 shows a bimodal distribution centred at 6.8 nm and 10.3 nm , while in the other two cases PSD are monomodal and centred at around 6.8 nm and 7.5 nm for TiO_2_DHBC_1 and TiO_2_DHBC_3 samples, respectively. Pore volume results to be 0.16 cm^3g^{-1} in all the samples.

Sample	DHBC	$<D_{XRD}>$	S_{BET} (m^2g^{-1})	V_p (cm^3g^{-1})	D_{pore} (nm)
TiO_2_DHBC_1	PEO-*b*-PVP_1	8.1 ± 0.4	101	0.16	6.8
TiO_2_DHBC_2	PEO-*b*-PVP_2	8.8 ±0.4	167	0.16	5.3
TiO_2_DHBC_3	PEO-*b*-PVP_2	9.1±0.4	97	0.16	7.5

Table 4.15 crystallite size ($<D_{XRD}>$) and textural features obtained by N_2-physisortion data for TiO_2_DHBC_1,v TiO_2_DHBC_2 and TiO_2_DHBC_3. S_{BET}=surface area, V_p= pore volume; D_p= pore diameter. Relative standard deviation: %RSD (S_{BET})=2.1%; %RSD(V_p)=1.1%; %RSD(D_p)=1.8%.

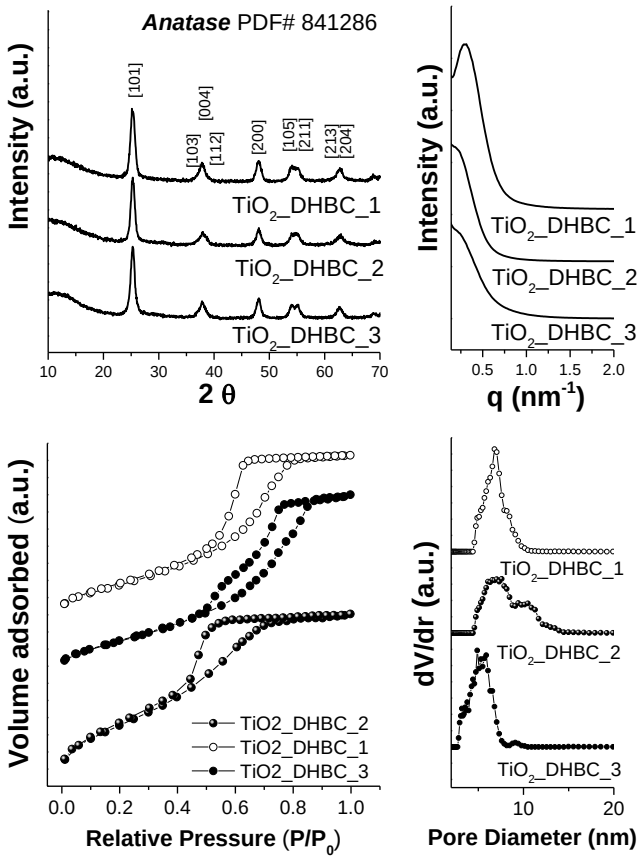

Figure 4.23 WA-XRD patterns(a), SAXS patterns (b), N_2 adsorption-desorption isotherms (c) and pore size distributions (d) of the samples TiO_2_DHBC_1, TiO_2_DHBC_2 and TiO_2_DHBC_3

According to these findings, all the samples can be classified as crystalline and mesoporous. However, just in case of the sample TiO_2_DHBC_1, a porous order was detected by SAXS. To confirm the presence of well define porous order, TEM analysis was performed on this sample (Figure 4.24). It can be observed the presence of non-porous rounded nanoparticles with similar size. Probably, due to the similarity particle size, the corresponding interparticles void formed during the packing of the particles, could justify the narrow PSD and the porous order in the nanometric range.

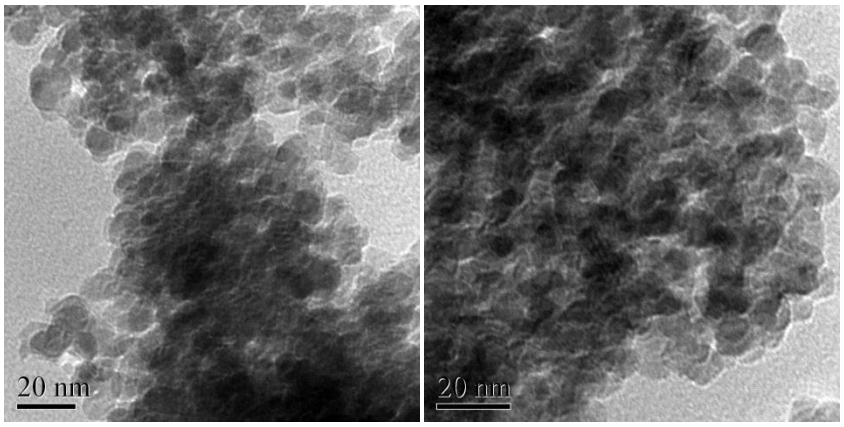

Figure 4.24 Representative TEM images of the sample TiO2_DHCB_1 after pyrolysis at 450 °C and characterization at 500°C

4.4 Selection of the most promising supports for the development of the iron oxide nanocomposites

The selection of the support for the development of the corresponding mesoporous nanocomposites was based on the specific requirements needed in the H_2S removal process at mid-temperature (300 °C).

Among the diverse siliceous and non-siliceous supports developed in this work, inspired by the promising results recently obtained by using SBA-15[2] composites, those reported in Table 4.16 have been selected on the basis of:

1. surface area, pore volume, and mesopore size distribution related to the capability to disperse the active phase and to the accessibility of H_2S;
2. thermal stability of the porous structure during the different sulphidation (300 °C) and regeneration (from 350 °C to 500 °C) cycles;
3. porous order and porous structure, also related to the capability to disperse the active phase and to the accessibility to the H_2S.
4. wall thickness, related to the robustness of the porous structure to improve the lifetime of the sorbent;
5. particle size related to the length of the mesochannels, and as a consequence of the accessibility of H_2S and regeneration gas flow.

support	Surface Area (m^2g^{-1})	Pore volume (cm^3g^{-1})	Pore diameter (nm)	Thermal stability	Porous structure	Space group	Walls thickness (nm)	Support particle size
SBA15	763	1.1	7.1	up to 600 °C	Hexagonal	*P6mm*	4.2	micro
MCM41	1063	0.76	2.3	up to 600 °C	Hexagonal	*P6mm*	1.7	micro
Hex_Nano_30_2	1248	0.80	2.2	up to 600 °C	Hexagonal	*P6mm*	1.7	nano D_{TEM} (110nm) D_{DLS} (147nm)
MCM48	1336	0.83	2.1	up to 600 °C	Cubic	*Ia3m*	1.4	micro
MCM41_Hyd	877	0.69	2.4	up to 600 °C	Hexagonal	*P6mm*	2.0	micro
TiO_2_450N_2_360O_2	274	0.3	3.9	up to 400 °C	Hexagonal	*P6mm*	4.8	micro

Table 4.16 Main features of the selected silica supports for the develop of the correspondents iron oxide-based sorbents.

This selection may lead to a better comprehension of the effect of the different textural properties on the performance of the corresponding Fe_2O_3-based sorbents with the same amount of active phase.

Specifically:

- **micrometric MCM41 (MCM41**) was selected to be compared to SBA15 because it shows the same porous structure (hexagonal, space group *P6mm*) and particle size in the micrometric range.

  In principle, this comparison could allow to study the effect of surface area and pore size on the dispersion of the active phase and the related performances in terms of sulphur retention capacity and regenerability. Another critical aspect that can be studied is connected to the thermal stability of the MCM41S samples, that show, with respect to SBA15, thinner silica walls.
- **Nanometric MCM41 (Hex_Nano_30_2)** was chosen to be compared to micrometric MCM41 to study the effect of the particles size, directly connected with the mesochannels length, and in principle to the accessibility of H_2S and the regeneration gas to the active phase. This comparison can be possible thanks to the similar textural properties (e.g. surface area, pore volume, pore size, porous structure, silica wall thickness) the two supports exhibit.

- **Micrometric hydrothermal treated MCM41 (MCM41_Hyd)** was chosen to be compared to micrometric MCM41 and micrometric SBA15. The comparison with MCM41 permits to study the effect that wall thickness and active phase dispersion produce on supports featuring remarkable different surface area, regardless the pore size and pore size distribution. Instead, the comparison with SBA15 allow to verify the effect of pore size on the final sorbents performances, leaving aside surface area effects.
- **Micrometric MCM48 (MCM48)** was chosen to be compared to micrometric MCM41 to verify the effect of the tridimensional porous structure on the dispersion of the active phase and the related H_2S performance.
- **Micrometric TiO_2 (TiO_2_450N_2_360O_2)** was chosen to be compared to micrometric MCM41_Hyd to study the effect of the different nature of the support on the dispersion of the active phase and the related H_2S performance, being both support the same hexagonal porous structure.

References

1 M. Mureddu, I. Ferino, E. Rombi, M. G. Cutrufello, P. Deiana, A. Ardu, A. Musinu, G. Piccaluga and C. Cannas, *Fuel*, 2012, **102**, 691–700.

2 M. Mureddu, I. Ferino, A. Musinu, A. Ardu, E. Rombi, M. G. Cutrufello, P. Deiana, M. Fantauzzi and C. Cannas, *J. Mater. Chem. A*, 2014, **2**, 19396–19406.

3 J. S. Beck, J. C. Vartuli, W. J. Roth, M. E. Leonowicz, C. T. Kresge, K. D. Schmitt, C. T. W. Chu, D. H. Olson, E. W. Sheppard, S. B. McCullen, J. B. Higgins and J. L. Schlenker, *J. Am. Chem. Soc.*, 1992, **114**, 10834–10843.

4 A. E. C. Palmqvist, *Curr. Opin. Colloid Interface Sci.*, 2003, **8**, 145–155.

5 D. Zhao, Q. H. Dongyuan Zhao, Jianglin Feng and G. D. S. Nicholas Melosh, Glenn H. Fredrickson, Bradley F. Chmelka, *Science (80-.).*, 1998, **279**, 548–552.

6 K. Schumacher, M. Grün and K. . Unger, *Microporous Mesoporous Mater.*, 1999, **27**, 201–206.

7 A. Monnier, F. Schuth, Q. Huo, D. Kumar, D. Margolese, R. S. Maxwell, G. D. Stucky, M. Krishnamurty, P. Petroff, A. Firouzi, M. Janicke and B. F. Chmelka, *Science (80-.).*, 1993, **261**, 1299–1303.

8 J. C. Vartuli, K. D. Schmitt, C. T. Kresge, W. J. Roth, M. E. Leonowicz, S. B. McCullen, S. D. Hellring, J. S. Beck, J. L. Schlenker, D. H. Olson and E. W. Sheppard, *Chem. Mater.*, 1994, **6**, 2317–2326.

9 T. Suteewong, H. Sai, R. Cohen, S. Wang, M. Bradbury, B. Baird, S. M. Gruner and U. Wiesner, *J. Am. Chem. Soc.*, 2011, **133**, 172–175.

10 K. Schumacher, P. I. Ravikovitch, A. Du Chesne, A. V Neimark and K. K. Unger, *Langmuir*, 2000, **16**, 4648–4654.

11 M. Thommes, K. Kaneko, A. V. Neimark, J. P. Olivier, F. Rodriguez-Reinoso, J. Rouquerol and K. S. W. Sing, *Pure Appl. Chem.*, 2015, **87**, 1051–1069.

12 M. Kruk, M. Jaroniec and A. Sayari, *Adsorption*, 2000, **6**, 47–51.

13 P. Van Der Voort, M. Mathieu, F. Mees and E. F. Vansant, *J. Phys. Chem. B*, 1998, **102**, 8847–8851.

14 C. Cara, E. Rombi, A. Musinu, V. Mameli, A. Ardu, M. Sanna Angotzi, L. Atzori, D. Niznansky, H. L. Xin and C. Cannas, *J. Mater. Chem. A*, 2017, **5**, 21688–21698.

15 S.-H. Wu, C.-Y. Mou and H.-P. Lin, *Chem. Soc. Rev.*, 2013, **42**, 3862.

16 W. Stöber, A. Fink and E. Bohn, *J. Colloid Interface Sci.*, 1968, **26**, 62–69.

17 R. I. Nooney, D. Thirunavukkarasu, Y. Chen, R. Josephs and A. E. Ostafin, *Chem. Mater.*, 2002, **14**, 4721–4728.

18 T. Suteewong, H. Sai, J. Lee, M. Bradbury, T. Hyeon, S. M. Gruner and U. Wiesner, *J. Mater. Chem.*, 2010, **20**, 7807.

19 T.-W. Kim, P.-W. Chung and V. S.-Y. Lin, *Chem. Mater.*, 2010, **22**, 5093–5104.

20 K. Ikari, K. Suzuki and H. Imai, *Langmuir*, 2006, **22**, 802–806.

21 D. Gu and F. Schüth, *Chem. Soc. Rev.*, 2014, **43**, 313–344.

22 W. Zhou, F. Sun, K. Pan, G. Tian, B. Jiang, Z. Ren, C. Tian and H. Fu, *Adv. Funct. Mater.*, 2011, **21**, 1922–1930.

23 G. J. D. A. A. Soler-Illia, A. Louis and C. Sanchez, *Chem. Mater.*, 2002, **14**, 750–759.

24 D. Grosso, C. Boissière, B. Smarsly, T. Brezesinski, N. Pinna, P. A. Albouy, H. Amenitsch,

M. Antonietti and C. Sanchez, *Nat. Mater.*, 2004, **3**, 787–792.

25 S. Guldin, M. Stefik, H. Sai, U. Wiesner and U. Steiner, *RSC Adv.*, 2015, **5**, 22499–22502.

26 J. Lee, M. Christopher Orilall, S. C. Warren, M. Kamperman, F. J. DiSalvo and U. Wiesner, *Nat. Mater.*, 2008, **7**, 222–228.

27 R. Zhang, B. Tu and D. Zhao, *Chem. - A Eur. J.*, 2010, **16**, 9977–9981.

28 B. V. K. J. Schmidt, V. Molinari, D. Esposito, K. Tauer and M. Antonietti, *Polymer (Guildf).*, 2017, **112**, 418–426.

29 H. Colfen, H. Cölfen, H. Colfen and H. Cölfen, *Macromol. Rapid Commun.*, 2001, **22**, 219–252.

30 I. a Nyrkova and A. N. Semenov, *Faraday Discuss.*, 2005, **128**, 113–127.

31 J. Willersinn, M. Drechsler, M. Antonietti and B. V. K. J. Schmidt, *Macromolecules*, 2016, **49**, 5331–5341.

5. MCM-41 support for ultrasmall γ-Fe_2O_3 nanoparticles for H_2S removal

Abstract

In this chapter MCM-41 is proposed as possible new mesostructured support to build efficient and regenerable Fe_2O_3 nanocomposites (Fe_2O_3@MCM-41) for mid-temperature H_2S removal. In order to test the suitability of this class of supports a careful comparison of micrometric MCM41 composite (Fe_MCM41) with the analogous in SBA15 (Fe_SBA15) one and a commercial unsupported sorbent has been performed. Furthermore, nanometric MCM-41 sorbent (Fe_MCM41_N) has been prepared to evaluate the possible particles size effect on the H_2S performances.

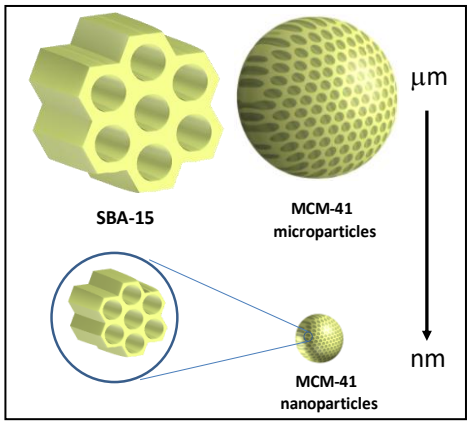

5.1 Introduction

MCM-41, although the very high surface areas, is rarely proposed in applications at mid- and high-temperature[1,2] probably because of the possible collapse of the mesoporous structure, "theoretically *fragile*" owing to its small pore size and small wall thickness. Here, we decided to evaluate the feasibility of its use in repeated sulphidation (at 300 °C) and regeneration (at 500 °C) cycles due to its high potentiality to disperse the active phase. In fact, the reduced pore size (about 2 nm), imposing a physical limit to the growth of the particles, should induce the formation of ultra small iron oxide nanoparticles (< 2 nm), maximising the surface atoms available to interact with H_2S and therefore the sorbent perfomance. In this ideal conditions, the active phase will be completely involved in the reaction, and all the drawbacks described in the *shrinking unreacted core model* (see Chapter 3, paragraph 3.2) should be overcome. In order to assure an efficient and homogenous dispersion of the active phase into the pores as well as avoid plugging *phenomena* we decided to use a low Fe_2O_3 loading equal to 10% w/w. For these reasons, beside the common characterization of the support and corresponding composites by low and wide angle XRD, N_2-physisorption, TEM and DLS, other techniques have to be considered due to difficulties in studyng such diluted systems in form of ultrasmall nanoparticles. With this intent and taking into account that iron oxides phases show a great

variety of magnetic behaviours (ferrimagnetism, antiferromagnetism, superparamgnetism) we selected an *ad hoc* structural techinque as ^{57}Fe Mössbauer Spectroscopy that has been used in combination with DC magnetometry.

5.2 Sorbents preparation

Two different MCM-41 supports have been selected on the basis of the textural properties and particles dimension (see Chapter 4, paragraph 4) in order to prepare the corresponding composites and compare their H_2S removal capacity with that of SBA-15-based one. Table 5.1 reports the main features of the selected supports.

Support	Surface Area (m^2g^{-1})	Pore volume (cm^3g^{-1})	Pore diameter (nm)	Thermal stability	Porous structure	Space group	Walls thickness (nm)	Support particle size
SBA15	763	1.1	7.1	up to 600 °C	Hexagonal	*P6mm*	4.2	micro
MCM41	1063	0.76	2.3	up to 600°C	Hexagonal	*P6mm*	1.7	micro
Hex_Nano_30_2	1248	0.80	2.2	up to 600°C	Hexagonal	*P6mm*	1.7	nano D_{TEM} (110nm) D_{DLS} (147nm)

Table 5.1 Main features of the selected silica supports for the development of the correspondents iron oxide-based sorbents

As described elsewhere (Chapter 3 paragraph 3.5.3), considering the advantages of the Two-Solvents (TS) impregnation approach, this method has been chosen to obtain the iron oxide nanocomposites. Figure 5.1 reports a schematic illustration of the impregnation procedure for the synthesis of the nanocomposites.

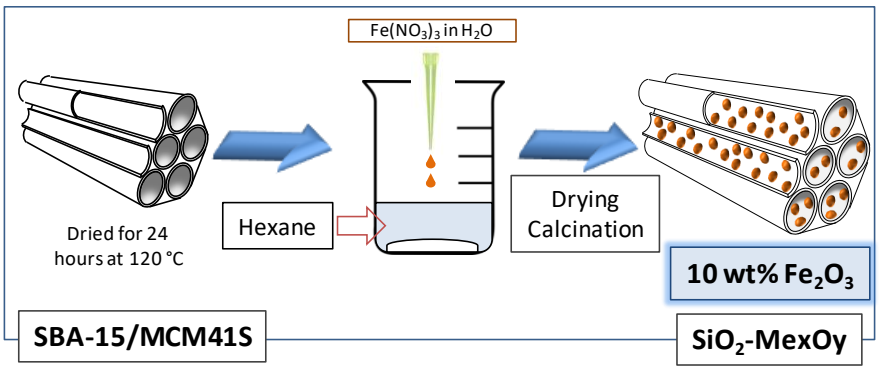

Figure 5.1 Schematic representation of the two solvents impregnation route used to prepare the mesostructured nanocomposites.

In a typical two solvents impregnation route, a drying step at 120 °C is carried out for one day to remove water from the silica pores. Then, the silica powder is dispersed in an apolar solvent (hexane) and kept under stirring for almost two hours at room temperature and a suitable

amount of metal oxide aqueous precursor ($Fe(NO_3)_3 \cdot 9H_2O$), calculated on the basis of the total pore volume and the desired iron oxide loading (10% w/w), is added drop-wise. After two hours, the dispersion is heated at 80 °C in a hot-plate until complete evaporation of the hexane, and then kept in an oven at 80 °C overnight. Finally, the product is calcined in static air at 500 °C (heating rate, 2 °C min^{-1}) for two hours in order to decompose the iron nitrate and obtain the corresponding metal oxide. Table 5.2 lists the conditions and amount of precursors used during the syntheses.

Sample	Support	Support amount (mg)	Support Pore volume (cm^3g^{-1})	Volume aqueous solution (μL)	$[Fe(NO_3)_3]$ in water	Fe_2O_3 (w/w) %
Fe_MCM41_M	MCM41	0.19	0.76	167	1.5	9.6
Fe_MCM41_N	Hex_Nano_30_2	0.20	0.80	177	1.5	9.6
SBA15	SBA15	0.10	1.10	125	1.1	10.0

Table 5.2 Experimental conditions for the two-solvents impregnation route

5.3 Sorbents characterization

Figure 5.2a shows the WA-XRD patterns of the bare SBA-15 and MCM-41 support (SBA15, MCM41_M and MCM41_N) and the corresponding Fe_2O_3 micrometric and nanometric composites with 10% w/w of Fe_2O_3. (Fe_MCM41_M, Fe_MCM41_N, Fe_SBA15). Besides the typical halo of amorphous silica at about 22°, the presence of two broad and low-intensity reflections at about 35° and 62° indicates the formation of a highly-dispersed iron oxide, probably in the form of ultrasmall nanoparticles. Among the different iron oxide phases maghemite (γ-Fe_2O_3) and hematite (α-Fe_2O_3) are the most probable, due to the calcination process in air. However, the position of the two reflections ascribable to the active phase seems to better match with those of the maghemite phase (PDF card #039-1346).[3] It is clear that, due to the partial overlapping of the silica broad band with the main reflection of the active phase, to the low content and the reduced particle size (< 2 nm) WA-XRD cannot univocally discriminate the crystallographic phase.

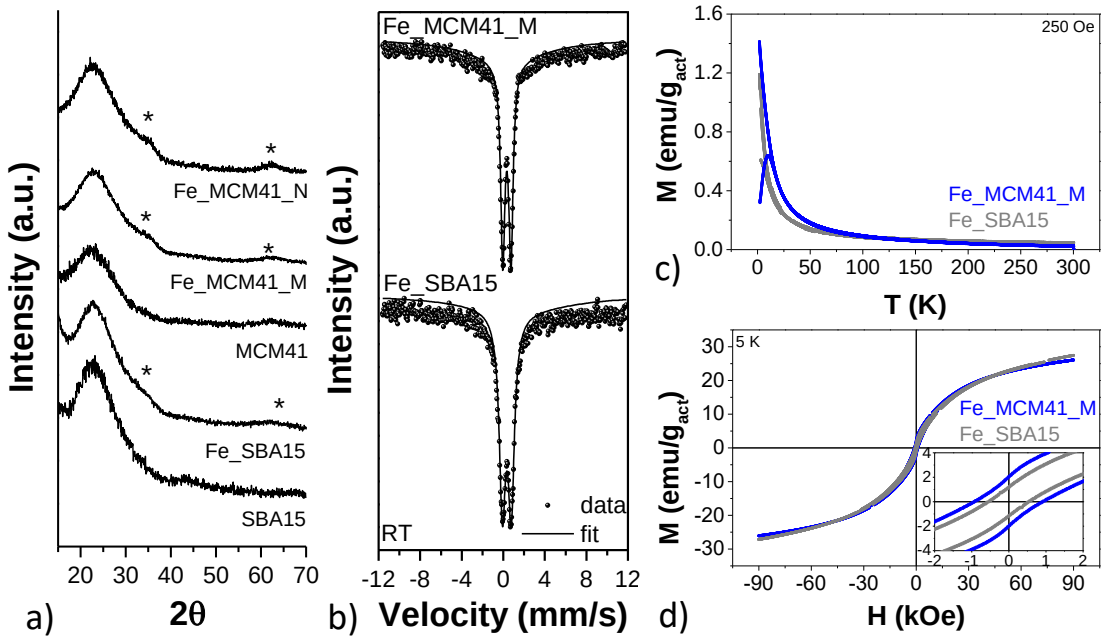

Figure 5.2 WA-XRD patterns of bare SBA15 and MCM41 and different iron oxide based composites (Fe_SBA15; Fe_MCM41_M and Fe_MCM41_N) (a), ^{57}Fe Mössbauer spectra of Fe_SBA15 and Fe_MCM41_M (b), field dependence (c), and temperature dependence of the magnetisation for the samples Fe_MCM41_M and Fe_SBA15 (d).

Aware that the sulphidation performances are strictly related to the iron oxide crystalline phase (Chapter 3, paragraph 3.4.1), more afford has been done to ascertain the actual presence of maghemite. To this end, room temperature ^{57}Fe Mössbauer Spectroscopy has been performed (Figure 5.2b) on Fe_SBA15 and Fe_MCM41_M composites. For both samples the spectra consist of a doublet showing isomer shift of 0.34 ± 0.01 mm s^{-1}, that confirms the formation of very small maghemite nanoparticles.[4–6] Moreover, FWHM has been found equal to 0.49 ± 0.01 mm s^{-1} and 0.74 ± 0.01 mm s^{-1} for Fe_MCM41_M and Fe_SBA15, respectively. This difference suggests different particles size or particle size distributions in the two samples. In order to get further details on the active phase, the magnetic behaviour has been studied by temperature (*M vs. T*) and magnetic field (*M vs. H*) dependences of the magnetisation (Figure 5.2c and d). The temperature dependence of the magnetization has been recorded by means of the zero field cooled-field cooled (ZFC-FC) protocols.

The curves appear overlapped at high temperature while they start to diverge at low temperature (< 25 K). Below this temperature (T_{irr}), the curves of the two samples show some differences: those of the Fe_MCM41_M clearly exhibit a maximum in the ZFC curves at about 10 K (T_{max}) while for the Fe_SBA15 sample the whole trend seems to be shifted toward lower temperature, with an uncompleted exhibition of the maximum in the experimental range. Such behaviour is characteristic for magnetic monodomain nanoparticles. Assuming the

presence of negligible interparticle interactions, the T_{max} can be considered directly related to the average volume of the particles, while T_{irr} is related to the biggest ones.[7,8] Therefore $(T_{irr} - T_{max})$ values can provide a qualitative measure of the volume size distribution.[8]

Being the T_{max} and T_{irr} equal to 10 K and 14 K for the Fe_MCM41_M sample, the difference of 4 K suggests a very sharp particle size distribution. In the case of the Fe_SBA15, due to the absence of a defined maximum in the ZFC curve, it is not possible to extract information about the particles size distribution. However, the ZFC trend suggest a T_{max} close to 2 K indicating an average particles size smaller than the Fe_MCM41_M composite. These findings are in agreement with the different Mössbauer FWHM values, and suggest this parameter to be inversely related to the average particles size. The *M vs. H* curves at 5 K for both samples show a S-shaped hysteretic behaviour typical for ferro-ferrimagnetic phases, which tends to reach the saturation at about 27 emu/g (M_{9T}). Coercivity field values have been found equal to ~ 0.5 kOe and ~ 0.9 kOe for Fe_SBA15 and Fe_MCM41_M, respectively. Being the M_{9T} similar for both samples, the different coercivity and T_{max} confirm once again the different particles size in the two composites. Therefore, all the collected Mössbauer and magnetic data contribute to strengthen the idea that came to light from the WA-XRD data of the presence of maghemite (ferrimagnetic phase) in form of ultrasmall nanoparticles. Actually, the reassessment of the WA-XRD data evidences more pronounced reflexes in the case of MCM41 composite with respect to the SBA15, suggesting a higher crystallinity. Unexpectedly, these results suggest that the dimension of the maghemite nanoparticles are inversely correlated with the surface area and the pore diameter of the hosting support. Due to the complexity of such diluted nanostructured materials, the surface area and the pores diameter are just two of the factors that could affect the dispersion, nucleation and growth of the active phase within the pores. Other parameters such as the porous volume, hydrophilicity/wettability of the surface, and the pores surface curvature[9] could influence the particle size and the crystallinity of the active phase. In our synthetic conditions, during the two-solvent incipient impregnation process, the volume of the aqueous solution containing the iron oxide precursor has to be equal to the pores volume of the support (see paragraph 5.2). Therefore, the concentration of the solutions has been increased with decreasing porous volume in order to build up composites with the same iron oxide loading. In the case of SBA15, less concentrate solution has been used, due to the higher pores volume with respect to the MCM41_M (Table 5.2). In conclusion, it is reasonable to hypothesize that the higher the concentration of the iron oxide precursor solution the bigger the particles.

Figure 5.3a, b, c reports the LA-XRD patterns of the calcined supports and the corresponding composites. All samples are characterized by the presence of three reflection (100), (110), and (200) indicating a 2D long-range order typical for a hexagonal pore structure (*P6mm*). Table 5.3 reports *d*-spacing (d_{100}) and cell parameters (a_0). The nanocomposites retain the mesostructure, even if a slight shift of the reflections toward higher angles is detected, indicating a slight shrinkage of the pore structure.

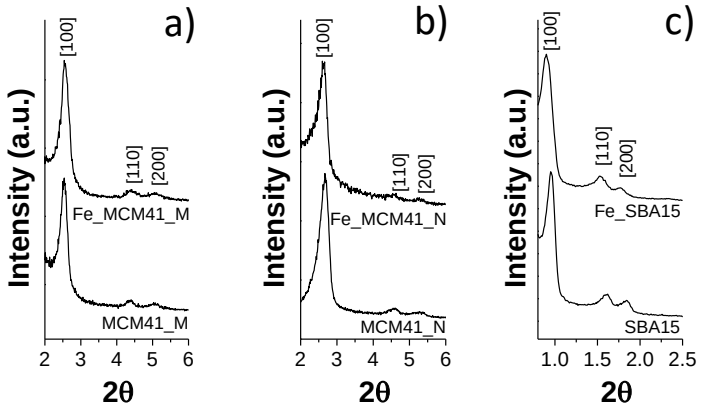

Figure 5.3 LA-XRD patterns of bare and loaded samples for micrometric MCM41(a), nanometric MCM41 (b) and micrometric SBA15 (c)

In order to get information about the dispersion of the active phase within the support, STEM-EDX mapping of Fe has been carried out (Figure 5.4a, d, g). For all samples, Fe is homogeneously spread into/onto the support and no evidence of isolated iron oxide particles outside or over the host is revealed in agreement with WA-XRD, ^{57}Fe Mössbauer and magnetic data. Figure 5.4b, c, e, f, h, i report the nitrogen adsorption-desorption isotherms and the pore size distribution (PSD) of both the supports and the relative composites. The textural parameters of the different samples are summarized in Table 5.3.

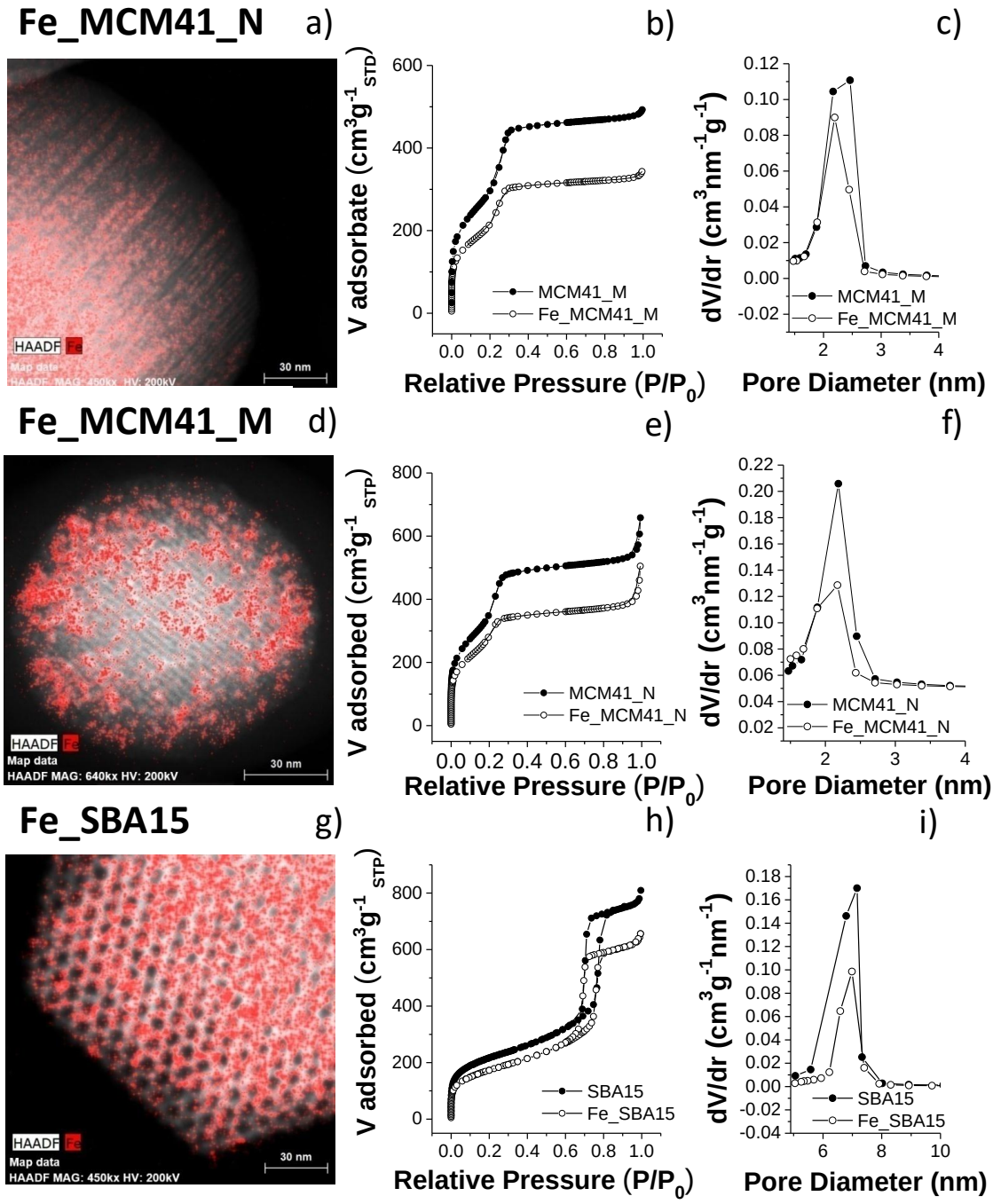

Figure 5.4 EDX-STEM images of the composites Fe_MCM41_M (a) Fe_MCM41_N (d).and Fe_SBA15 (g). N_2 adsorption–desorption isotherms and pore size distributions of the bare and composites of micrometric MCM41 (b, c), nanometric MCM41 (e, f) and micrometric SBA15 (h, i)

The MCM-41 composites (Fe_MCM41_M and Fe_MCM41_N) as well as the supports (MCM41_M and MCM41_N) exhibit characteristic IVB type behaviour according to the IUPAC classification.[10] The incorporation of the active phase leads, as expected, to a reduction in the surface area values (Table 5.3) owing to a remarkable decrease in the extent of mesopore adsorption. Pore size distribution (PSD) curves, calculated from the desorption branch (BJH

method), confirm these findings, with the PSD being centred at similar values for both the supports and the relative composites, although with lower intensity for the latter.

Sample	S_{BET} (m^2g^{-1})	V_p (cm^3g^{-1})	D_{pore} (nm)	w_t (nm)	d_{100} (nm)	a_0 (nm)
MCM41_M	1063	0.76	2.3	1.7	3.49	4.0
Fe_MCM41_M	768	0.53	2.2	1.6	3.47	4.0
MCM41_N	1248	0.80	2.2	1.7	3.37	3.9
Fe_MCM41_N	1007	0.58	2.2	1.7	3.33	3.9
SBA15	763	1.10	7.1	4.2	9.29	11.3
Fe_SBA15	601	1.01	6.9	4.5	9.91	11.4

Table 5.3 Textural features obtained by N_2 physisorption data for the supports and the corresponding composites. The last two columns list the d-spacing (d_{100}) and lattice parameter (a_0) obtained from LA-XRD diffraction data S_{BET}=Surface area; V_p=Pore volume; D_p=pore diameter. Relative standard deviation: %RSD(S_{BET})=2.1; %RSD(V_p)=1.1%; %RSD(D_p)=1.8%.

5.4 Sulphidation and regeneration processes

5.4.1 Sulphidation runs

Three sulphidation cycles at 300°C have been carried out for each sorbent to investigate the performances under a reactant gas containing only H_2S (15 200 ppm) in helium (inlet flow, 20cm^3 min^{-1}) in order to render the system as simple as possible and focus on the reactions between H_2S and the iron active phase. Figure 5.5 reports the breakthrough curves upon three sulphidation-regeneration cycles of the three composites and Katalko$_{JM}$ 32-5, a commercial unsupported ZnO sorbent considered as reference.

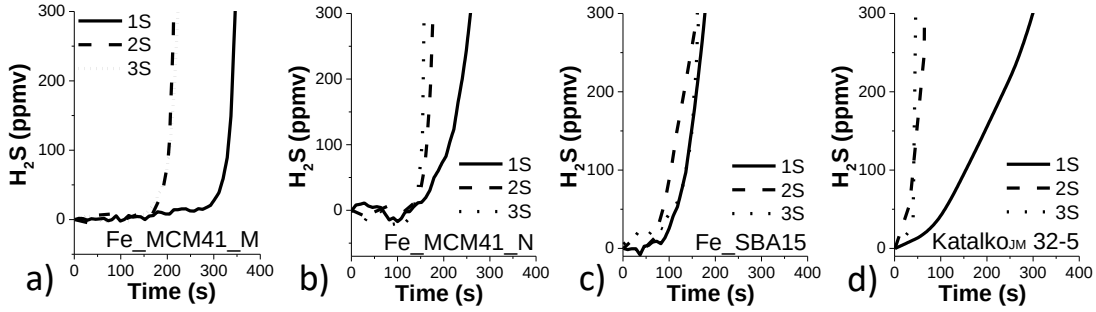

Figure 5.5 H_2S breakthrough curves upon three sulphidation–regeneration cycles (1S = first sulphidation, 2S = second sulphidation; 3S = third sulphidation) for the sample Fe_MCM41_M (a), Fe_MCM41_N (b), Fe_SBA15 (c) and KatalkoJM 32-5 (d)

The breakthrough time (B_t) at 100 ppm of H_2S in the outlet gas and the corresponding sulphur retention capacity (SRC), calculated according to the equation reported in appendix, are reported in Table 5.4.

Sample	B_t (s)	SRC ($mg_S\ g_{sorbent}^{-1}$)
Fe_ MCM41_M	295	38
Fe_ MCM41_M_R1	169	22
Fe_ MCM41_M_R2	169	22
Fe_ MCM41_N	187	25
Fe_ MCM41_N_R1	163	18
Fe_ MCM41_N_R2	153	17
Fe_SBA15	125	16
Fe_SBA15_R1	112	15
Fe_SBA15_R2	125	16
Katalco$_{JM}$ 32-5	122	16
Katalco$_{JM}$ 32-5_R1	10	1
Katalco$_{JM}$ 32-5_R2	13	2

Table 5.4 Breakthrough time (B_t) and sulphur retention capacity (SRC) of fresh and regenerated iron oxide-based sorbents over repeated sulphidation-regeneration cycles. R1=refers to the first regeneration. R2 refers to the second regeneration. The error in each SRC value can be estimated to ±2 $mg_S\ g_{sorbent}^{-1}$

In the first sulphidation run, the micrometric Fe_MCM41_M sorbent shows the best sorption capacity (SRC = 38$m_{gS}\ g_{sorbent}^{-1}$), *i.e.* 1.5 times higher than that of nanometric Fe_MCM41_N and 2.5 times higher than that of both Fe_SBA15 and commercial Katalco$_{JM}$ 32-5. Fe_MCM41_M keeps the best performances (22 $m_{gS}\ g_{sorbent}^{-1}$) also in the successive sulphidation cycles even if a remarkable decrease of SRC is observed. Such extent of reduction is significantly higher than that observed for nanometric Fe_MCM41_N sorbent. By contrast, the Fe_SBA15 sorbent does not show any difference of the SRC value between the first and the successive sulphidation runs (16 $m_{gS}\ g_{sorbent}^{-1}$). The worse performances are exhibited by the commercial sorbent, whose SRC value, after the first sorption run, decreases to almost zero considering the experimental error.

The sulphidation process has been monitored by quadrupole mass spectroscopy, which is proved to be an extremely useful technique to reveal the formation of different gas species forming during the different sulphidation and regeneration runs. In Figure 5.6 the first sulphidation run for each composite is reported.

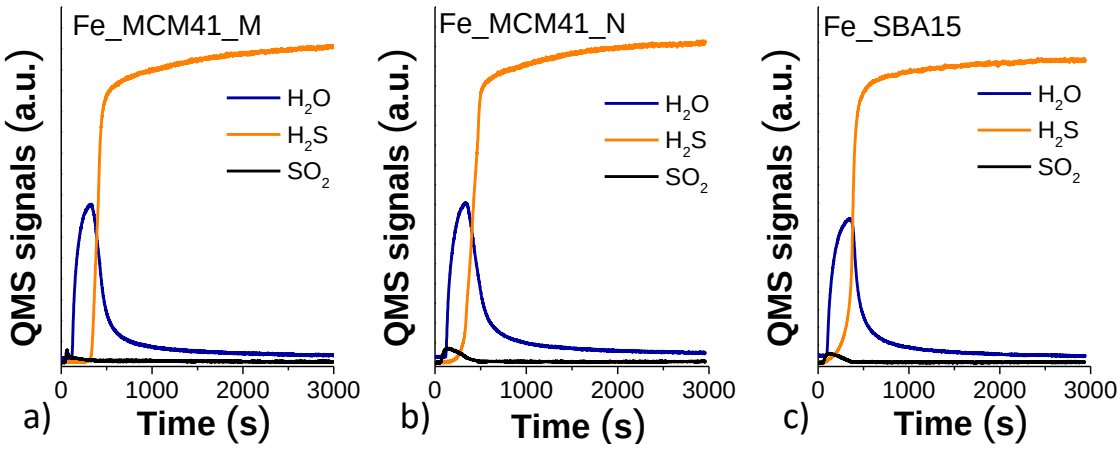

Figure 5.6 H_2S, SO_2 and H_2O QMS profiles during the first sulphidation of the sample Fe_MCM41_M (a), Fe_MCM41_N (b) and Fe_SBA15 (c)

The removal of H_2S is accompanied by the formation of a great amount of H_2O and a small quantity of SO_2 according to the substitution reaction (equation 5.1) reported in the following. Fe_2S_3 is known to be a thermodynamically unstable phase that easily converts to pyrite (FeS_2)[3] and Fe_3S_4[11,12] (equation 5.2) or pyrite, pyrrhotite (FeS_x) and sulphur[13] (equation 5.3, where α, β, γ are the relative molar amounts). The release of a small amount of SO_2 is probable, due to the redox reaction of H_2S that leads to the formation of FeO (equation 5.4)[14] that further react with H_2S forming FeS (equation 5.5). Therefore, in the selected operating conditions, the sulphidation process is governed by the substitution reaction.

$$Fe_2O_3 + 3H_2S \rightarrow Fe_2S_3 + 3H_2O \qquad \textit{equation 5.1}$$

$$2\,Fe_2S_3 \rightarrow FeS_2 + Fe_3S_4 \qquad \textit{equation 5.2}$$

$$Fe_2S_3 \rightarrow \alpha\,FeS_2 + \beta FeS_x + \gamma S \qquad \textit{equation 5.3}$$

$$3\,Fe_2O_3 + H_2S \rightarrow 6\,FeO + SO_2 + H_2O \qquad \textit{equation 5.4}$$

$$FeO + H_2S \rightarrow FeS + H_2O \qquad \textit{equation 5.5}$$

The sulphided sorbents have been characterized by WA-XRD to understand the possible reactions. In all the cases (Figure 5.7a), the sulphided sorbents show only the broad band of amorphous silica and no evidence of any other phase. Previous studies carried out in the same experimental conditions and setup[15] tested a commercial nanostructured maghemite. The results pointed out the formation of two sulphides species (pyrite, pyrrhotite), suggesting the reaction reported in equation 5.3 and the presence of unreacted maghemite. The presence of

this latter phase can be justified considering that pure metal oxide, although nanostructured, suffer of the drawbacks well described by the shrinking unreacted core model.

As an example, Figure 5.7b andc report STEM-EDX mapping of Fe and S carried out on the sulphided Fe_SBA15 composites after three repeated sulphidation runs (Fe_SBA15_S3). Iron and sulphur result to be homogeneously spread all over the sample suggesting a wide involvement of the active phase in the sulphidation reaction.

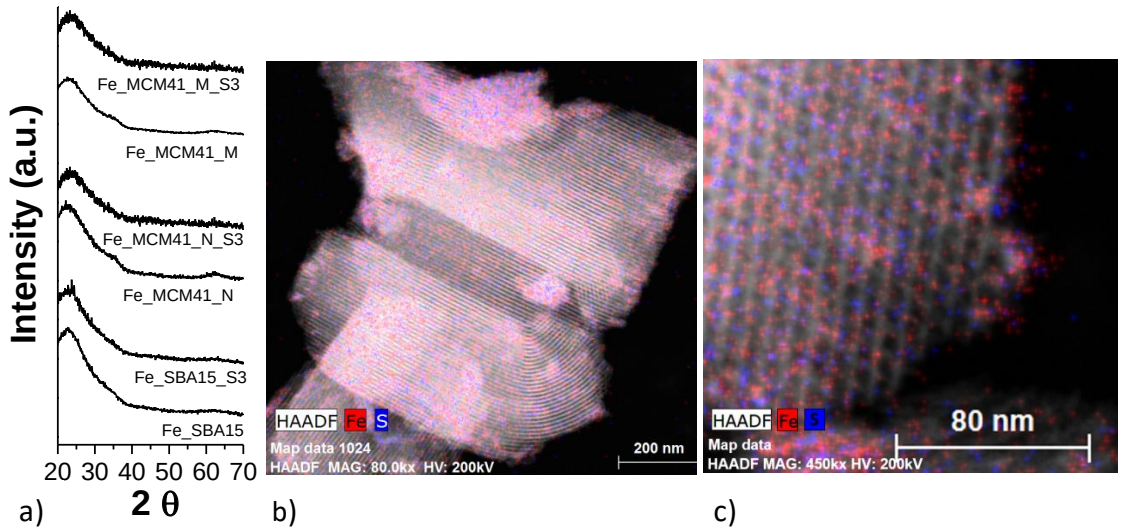

Figure 5.7 WA-XRD of the fresh, (Fe_SBA15, Fe_MCM41_M and Fe_MCM41_N) and three time sulphided sorbents (Fe_SBA15_S3, Fe_MCM41_N_S3 and Fe_MCM41_M_S3). EDX-STEM images of the composites Fe_SBA15_S3.

In order to justify the worsening of the performance after the first sulphidation, the possibility of a non-complete regeneration has been investigated by CHNS measurements. The result evidences the presence of 1.4 wt% of sulphur in the regenerated sample and justifies the decrease in the SRC value as mainly due to the presence of residual iron sulphides. However, it cannot be excluded that the active phase, when submitted to the regeneration process, undergoes changes in surface properties or crystallinity, as suggested in the literature.[3]

5.4.2 Regeneration runs

The regeneration process was performed at 500°C (heating rate of 10°C min^{-1}) by flowing air (20 cm^3g^{-1}), and monitoring the outlet gas by both a thermal conductivity detector (TCD) and a quadrupole mass spectrometer (QMS). The first regeneration run for each sorbent is reported in Figure 5.8. Similar regeneration profiles have been obtained for the other two regeneration runs.

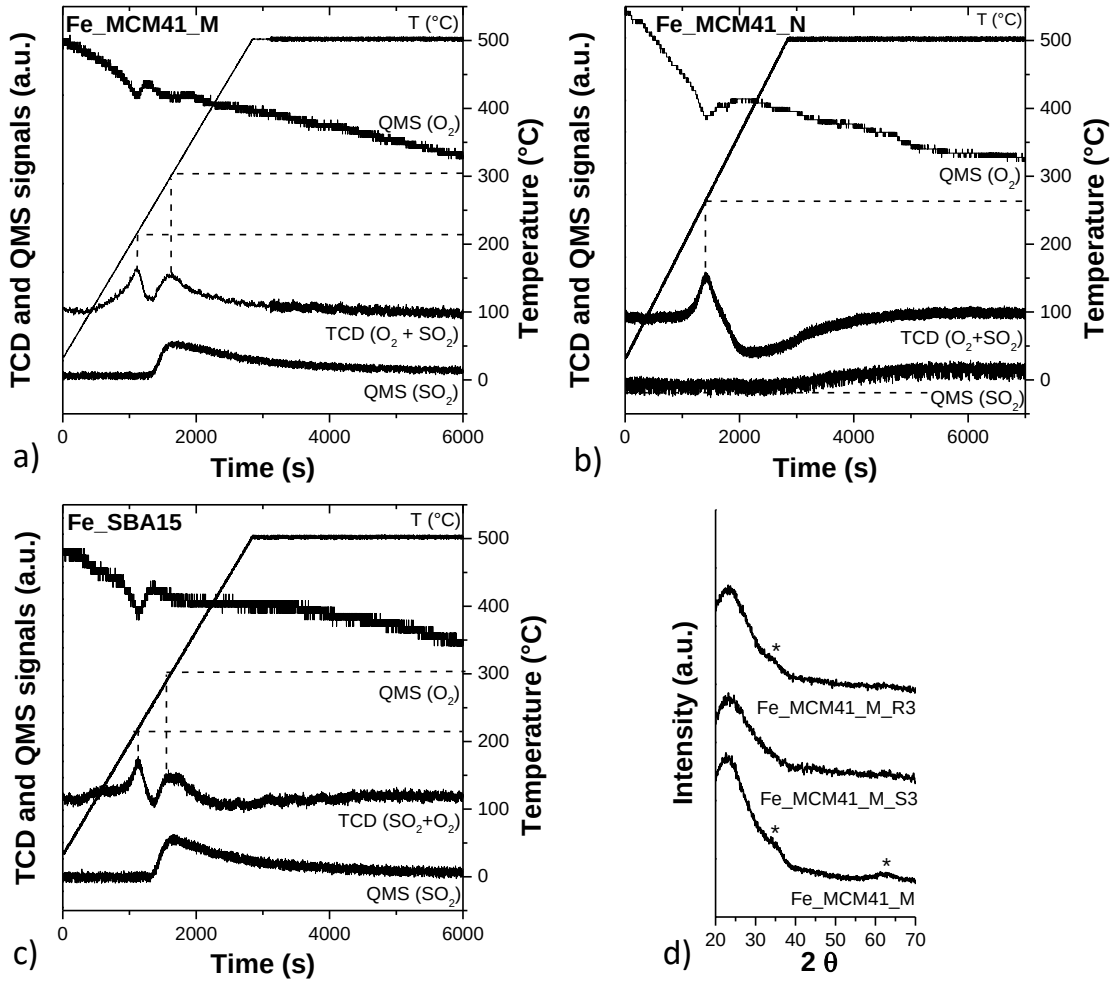

Figure 5.8 Thermal conductivity detector TCD profile and SO_2 and O_2 Quadrupole Mass Spectrometer (QMS) signals of Fe_MCM41_M (a), Fe_MCM41_N (b) and Fe_SBA15 (c). WA-XRD of the fresh Fe_MCM41_M, three times sulphidated (Fe_MCM41_M_S3) and three times regenerated (Fe_MCM41_M_R3).

TCD profiles are characterized by the presence of two main peaks: in the case of the sample Fe_MCM41_M and Fe_SBA15 sorbents the first peak, corresponding to the O_2 consumption (upper curve, QMS (O_2)), is centred at about 210 °C, and the second one at about 300°C is related to SO_2 release, as confirmed by the QMS (bottom curve). In the case of Fe_MCM41_N sorbent, the first peak is shifted toward higher temperature (260°C), while the second one is shifted and broader suggesting a slow release of SO_2 up to 500°C.

The regeneration behaviour is in agreement with the reported reactions for the different iron sulphides with oxygen, as expressed by equations 5.6,[16] 5.7 and 5.8.[17]

$$4FeS_2 + 11O_2 \rightarrow 2\,Fe_2O_3 + 8\,SO_2 \qquad \textit{equation 5.6}$$

$$Fe_3S_4 + 2O_2 \rightarrow 2\,Fe_3O_4 + 4S \qquad \textit{equation 5.7}$$

$$FeS_x + xO_2 \rightarrow Fe_2O_3 + xSO_2 \qquad \textit{equation 5.8}$$

The reduced phase (FeS) could instead lead to the formation of sulphur:[18]

$$4\,FeS + 3O_2 \rightarrow 2\,Fe_2O_3 + \frac{1}{2}\,S_8 \qquad \textit{equation 5.9}$$

As in the case of the sulphided systems, due to the low content of the active phase (10 % w/w), and to the ultrasmall size of the particles, wide angle XRD analysis is not able to give incontrovertible information about the crystallographic phases formed during the sulphidation-regeneration processes (Figure 5.8) and to confirm the proposed reaction scheme for H_2S removal. With this aim, it is planned to perform more careful characterization by XPS, ^{57}Fe Mössbauer spectroscopy and DC magnetometry.

5.5 Regenerated sorbents characterization

In order to verify the stability after repeated sulphidation-regeneration cycles, N_2-physisorption and low-angle XRD measurements have been performed on the MCM41 composites after the third regeneration step (Fe_MCM41_M_R3 and Fe_MCM41_N_R3) and the results have been compared with those of the fresh sorbents (Figure 5.9).

LA-XRD analyses indicate that the micrometric Fe_MCM41_M sample retains the hexagonal pore structure (Figure 5.9a). Surface area, pore volume, and pore size distribution are also preserved, confirming the high stability of this sorbent (see Table 5.5). Conversely, a partial structural collapse as well as a worsening of the textural properties are observed for the nanometric sorbent (Figure 5.9d), the latter ascribable to the decrease of both micro and mesopores contributions that lead to an almost completely microporous structure.

In order to better understand the actual reasons behind the behaviour of the nanometric sorbent, by considering that the sorbents have been tested three months later than their textural characterization, further measurements (LA-XRD and N_2-physisorption) have been repeated on a portion of the same sample not sulphided after three months aging (aged).

The comparison between the textural properties of the fresh (as-prepared, Fe_MCM41_N) and aged (Fe_MCM41_N_aged) nanometric sorbents pointed out the reorganization of the porous structure with the consequent loss of mesoporosity.[19] During the aging time, the water present in the air can react with the silica surface hydrolyzing the Si-O-Si bonds and forming silanols groups.

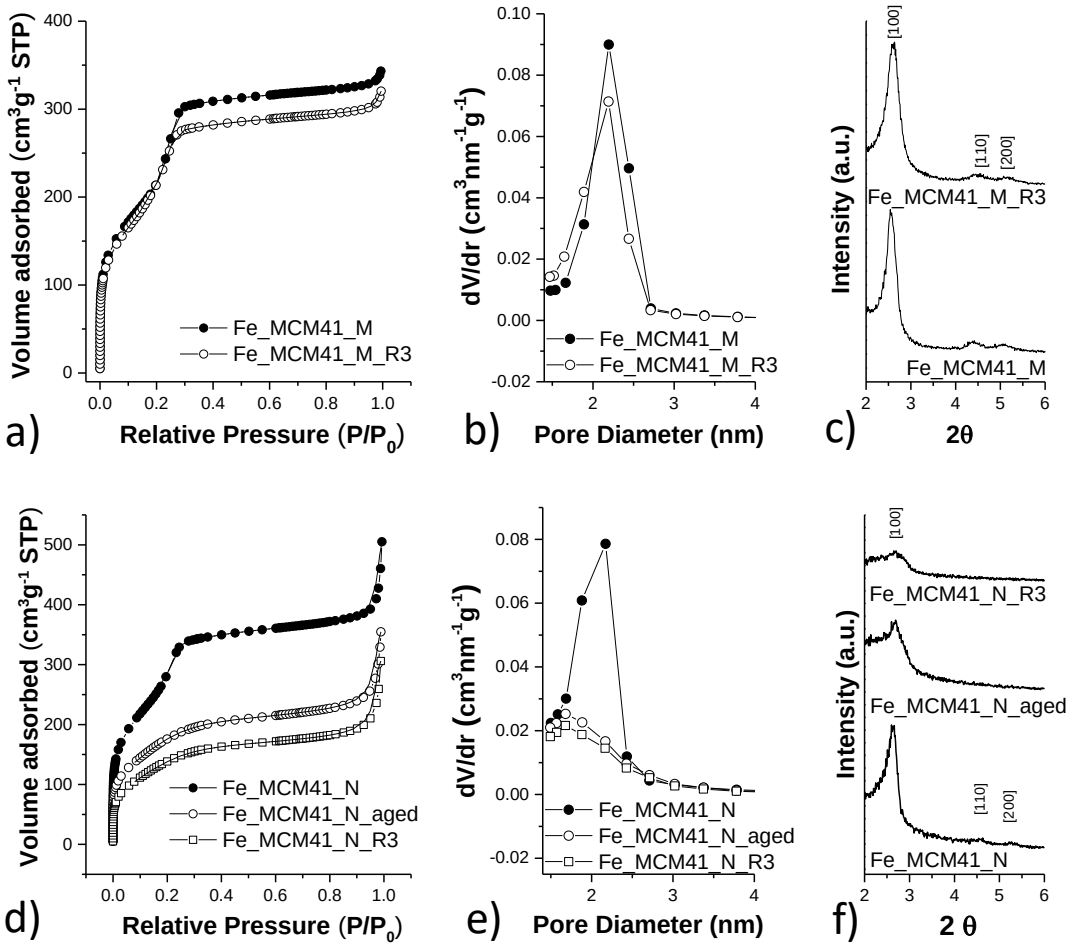

Figure 5.9. Nitrogen adsorption-desorption isotherms, pore size distributions and LA-XRD patterns of: Fe_MCM41_M and Fe_MCM41_M_R3 (a, b, c); Fe_MCM41_N, Fe_MCM41_N_R3 and Fe_MCM41_N_aged (d, e, f)

Sample	S_{BET} (m^2g^{-1})	V_p (cm^3g^{-1})	D_{pore} (nm)	w_t (nm)	d_{100} (nm)	a_0 (nm)
Fe_MCM41_M	768	0.53	2.2	1.6	3.47	4.0
Fe_MCM41_M_R3	771	0.49	2.2	1.7	3.41	3.9
Fe_MCM41_N	1007	0.58	2.2	1.7	3.33	3.9
Fe_MCM41_N_aged	651	0.37	1.7	2.2	3.28	3.8
Fe_MCM41_N_R3	496	0.29	1.7	2.0	3.26	3.7

Table 5.5 Textural features obtained by N_2-physisorption data for fresh composites and three time sulphidated. The last two columns list d-spacing (d_{100}) and lattice parameter (a_0) obtained from the LA-XRD patterns

In order to estimate the remaining contribution of micro- and mesoporous volumes after aging and three repeated Fe_MCM41_N samples, *t-plot* method has been applied for the MCM41_M composites (Fe_MCM41_M; Fe_MCM41_M_aged and Fe_MCM41_M_R3). The determination of the average thickness *t*(P) of the film adsorbed on the flat reference surface as a function of the pressure P has been performed following the Gaterneau approch.[20] In the case of the materials containing micropores, none of the linear regime is getting through the origin of the *t*-plot, and the intercept of the linear fit in the low-pressure range is classically taken as the microporous volume.[20] In this case, *t-plot* graph reported in Figure 5.10 permits to clarify

which typology of pores collapsed. The capillary condensation that take place at about 0.4 nm in the fresh sorbent is completely absent in the Fe_MCM41_N_aged and Fe_MCM41_N_R3 composites, causing a remarkable decrease of the pores volume (Table 5.6) pointing out the complete collapse of the mesoporous structure. Furthermore, no variation of the microporous volume is detected.

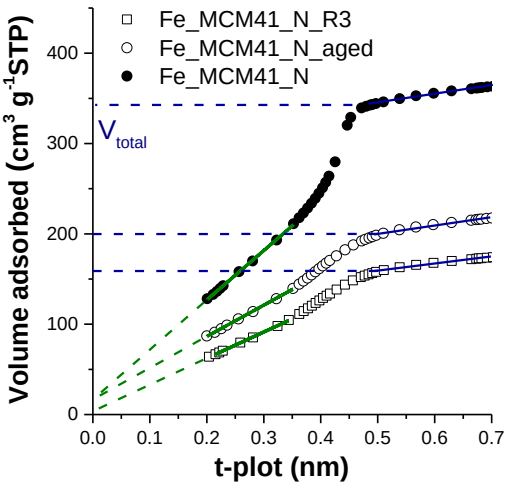

Figure 5.10 *t-plot* graph of the samples Fe_MCM41_N; Fe_MCM41_N_aged and Fe_MCM41_N_R3. The intercept of the dashed blue line with the y-axis provides an estimate of the total porous volume, while the intercept of the green line provides an estimate of the microporous volume

Sample	$V_{tot\ t\text{-}plot}$ (cm^3g^{-1})	$V_{micro\ t\text{-}plot}$ (cm^3g^{-1})
Fe_MCM41_M	0.62	0.01
Fe_MCM41_M_aged	0.39	0.01
Fe_MCM41_M_R3	0.32	0

Table 5.6 Total porous volume and microporous volume estimated by t-plot graph of the sample Fe_MCM41_N; Fe_MCM41_N_aged and Fe_MCM41_N_R3

5.6 Discussion

This work proves that, MCM-41, rarely used in mid- and high temperture applications, can be proposed for the preparation of efficient and highly regenerable sorbents for H_2S removal at mid-temperature as an alternative support to the most common SBA-15 and other porous amorphous alumina and silica. The high surface area and the reduced pore size (2 nm) with narrow pore size distribution, together with the relative low iron oxide content, allow to disperse homogeneously the active phase in form of ultrasmall maghemite nanoparticles, assuring the ideal conditions for its complete reaction with H_2S. Furthermore, being the nanocomposites regenerable at temperatures near to the sulphidation temperature (300 °C), maghemite has proved to be a promising active phase for the development of a new generation of solid sorbents for processes based on IGCC systems, also due to its low cost and

low-toxicity.[21] In fact, at the same conditions, in terms of sulphidation (300 °C) and regeneration (500 °C) temperatures, Fe_MCM41_M sorbent in form of micrometric particles, althogh it is claimed to show a *theoretically fragile* structure, retain its textural properties as the most robust SBA-15 counterpart and shows the best performance. However, when prepared in form of nanoparticles, the corresponding nanocomposite (Fe_MCM41_N) shows a gradual worsening of the performances due to the partial collapse of the porous structure (Table 5.5).

With the aim of understanding the effect of the pore size and the corresponding surface area, a comparison of the SRC values between the two micrometric sorbents (Fe_MCM41_M and Fe_SBA15) (Figure 5.11a) with the same hexagonal porous structure (*p6mm*) and iron oxide content (10% w/w) has been carried out. The characterization evidences that, besides pore size and the surface area, the crystallinity of the active phase has a important role in improving the H_2S performance. On the one hand, being the kinetic diameter of H_2S and N_2 very similar,[22] the surface area calculated by N_2-physisorption should be considered the effective surface accessible to H_2S molecules.[23] Going from micrometric SBA-15 to micrometric MCM-41, an increase of 28%-30% in the surface area has been observed for both the bare supports (SBA15 MCM41_M, see Table 1) and the corresponding composites (Fe_SBA15 and Fe_MCM41_M). As a consequence, the SRC value for Fe_MCM41_M is always higher than that for Fe_SBA15, and from the second sulphidation step it stabilizes at a value 35% higher than that of Fe_SBA15. However, other authors[24] for ZnO-based sorbents found a better performance for the SBA15-based sorbents than for the MCM-41 ones. This can be justified taking into account that on the final performances, the different impregnation strategy, the different active phase, as well as its different dispersion in the mesochannels can have an important role. In fact, it is known that due to the high affinity of zinc cations for silanol groups, in some cases thin layer of amorphous zinc oxide phase is formed,[25,26,3] while small iron oxide nanoparticles are instead formed from iron (III) salts using the same impregnation strategy.[3]

One the other hand, the active phase features, besides those of the support, have to be considered. In particular, the combined use of WA-XRD diffraction, ^{57}Fe Mössbauer and DC magnetometry has allowed to identify the crystallographic phase, the dimension of the particles/ crystallinity and permit to understand how they influence the H_2S performance of the sorbents. Indeed, the composite with the best performance is the one with the highest crystallinity. This result is in agreement with another study on ZnO-SBA15 showing an improvement of the performance with an increase of the crystallinity.[27]

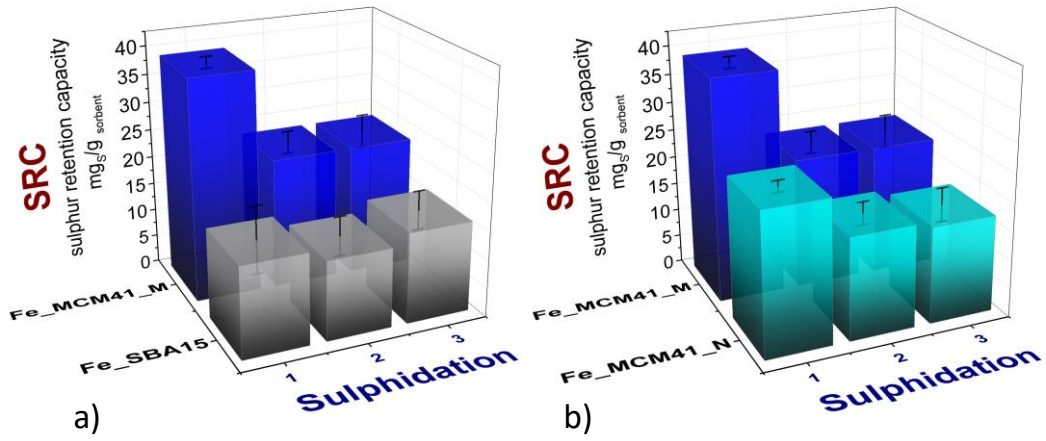

Figure 5.11 Comparison of SRC values of (a) micrometric sorbents: FeSBA15 versus FeMCM41_M and (b) micrometric and nanometric MCM41 Fe_MCM41_M and Fe_ MCM41_N sorbents

With the intent to study the effect of the silica particle size on the accessibility of the active phase, a further comparison of the SRC values between micrometric and nanometric MCM-41 based sorbents is attempted (Figure 5.11b). In order to reduce the support particle size, in the case of the MCM41_N support, as growth inhibitor ethyl acetate is used during the synthesis. The reduction of the particle size down to the nanoscale has as direct effect on the reduction in the pore length, thus facilitating, at least in principle, the H_2S accessibility to the iron oxide active phase. Moreover, the nanometric composite (Fe_MCM41_N) showed a surface area (1007 $m^2 g^{-1}$) 30 % higher than that of the micrometric MCM-41 composite (768 $m^2 g^{-1}$). By considering the key role of the surface area and the reduced length of the pores, nanometric systems would be considered ideal sorbents for improving the sulphur retention capacity. However, in all sulphidation cycles, the nanometric sorbent showed a worse performance than micrometric one (Figure 5.11b). The comparison between the N_2-isotherms and the LA-XRD data recorded soon after its preparation (as-prepared), after three months of aging (aged) and after the third regeneration process (R3) (see Figure 5.9) has allowed to understand the reason. The remarkable reduction of the surface area from 1007 $m^2 g^{-1}$ to 651 $m^2 g^{-1}$ (35% of reduction) can be justified by the possible gradual closing of the pores over time due to the reaction with water present in the air. Other authors evidenced similar effects for MCM-41 in contact with air[28] or when dispersed in water.[29,30] A further worsening of the textural properties in terms of the surface area (decrease down to 496 $m^2 g^{-1}$) is clearly due to the repeated sulphidation-regeneration cycles, probably caused by water formed during the reaction between the active phase and H_2S during the sulphidation process (*equation 3.1.1*). These results pointed out that the surface area is just one of the parameter that has to be controlled and maximized. The stability of the support porous structure over time, which is

strictly related to the accessibility of the active phase, is another important aspect that have to be considered and carefully checked for a proper design of an efficient and regenerable sorbent.

5.7 Conclusion

Mesostructured γ-Fe_2O_3@MCM-41 nanocomposites have been proved to be promising sorbents for H_2S removal at mid-temperature due to the high surface area and the homogenous dispersion of ultrasmall particles of maghemite within the small mesochannels. The comparison with the analogous silica-based sorbent (Fe_SBA15) and with a commercial sorbent evidences the superior performance, with a sulphur retention capacity that reaches the highest value for the micrometric MCM41-based sorbent (38 $mg_S\ g_{sorbent}^{-1}$, compared to 25 $mg_S\ g_{sorbent}^{-1}$ and 16 $mg_S\ g_{sorbent}^{-1}$ for the Fe_MCM41_N and Fe_SBA15 composites, respectively). The optimization of surface area by reducing the pore size and wall thickness with respect to SBA15 has found to be a remarkable aspect for the improvement of the sulphur retention capacity. However, it is clear that the crystallinity of the active phase is crucial because influence directly the reactivity toward H_2S. The comparison of the efficiency of the micrometric and nanometric MCM41-based sorbents in removing H_2S has highlighted that other factors, as the retention of the porous structure during their storing and use, must be taken into account. The repeated sulphidation-regeneration cycles showed that, after a first decrease in the SRC value between the first and the second sulphidation steps, the H_2S sorption capacity of the γ-Fe_2O_3@MCM-41 composites is preserved, suggesting their potential application as sorbents in mid-temperature processes. The proposal of this class of materials as alternative sorbents for highly efficient IGCC plants is also supported by the results of their regeneration, which was observed to occur at about 300 °C, temperature at which the sulphidation step is performed. Furthermore, the synthetic strategy of the composites is simple, reproducible, and does not involve purification steps, thus allowing it to be easily scaled-up.

References

1 C. Wu, Y. Kong, F. Gao, Y. Wu, Y. Lu, J. Wang and L. Dong, *Microporous Mesoporous Mater.*, 2008, **113**, 163–170.

2 G. K. Chuah, X. Hu, P. Zhan and S. Jaenicke, *J. Mol. Catal. A Chem.*, 2002, **181**, 25–31.

3 M. Mureddu, I. Ferino, A. Musinu, A. Ardu, E. Rombi, M. G. Cutrufello, P. Deiana, M. Fantauzzi and C. Cannas, *J. Mater. Chem. A*, 2014, **2**, 19396–19406.

4 E. M. and J. H. Johnston, *Mossbauer Spectroscopy Applied to Inorganic Chemistry*, New York, 1987.

5 R. C. and U. Schwertmann, *The Iron Oxides: Structure, Properties, Reactions, Occurences and Uses, Second Edition*, 2004.

6 C. Cara, A. Musinu, V. Mameli, A. Ardu, D. Niznansky, J. Bursik, M. A. Scorciapino, G. Manzo and C. Cannas, *Cryst. Growth Des.*, 2015, **15**, 2364–2372.

7 M. F. Hansen and S. Mørup, *J. Magn. Magn. Mater.*, 1999, **203**, 214–216.

8 C. Cannas, A. Musinu, A. Ardu, F. Orrù, D. Peddis, M. Casu, R. Sanna, F. Angius, G. Diaz and G. Piccaluga, *Chem. Mater.*, 2010, **22**, 3353–3361.

9 A. Anedda, C. M. Carbonaro, F. Clemente, R. Corpino, P. C. Ricci, D. Fisica and U. Cagliari, *J. Phys. Chem. B*, 2003, **107**, 13661–13664.

10 M. Thommes, K. Kaneko, A. V. Neimark, J. P. Olivier, F. Rodriguez-Reinoso, J. Rouquerol and K. S. W. Sing, *Pure Appl. Chem.*, 2015, **87**, 1051–1069.

11 A. Davydov, K. T. Chuang and A. R. Sanger, *J. Phys. Chem. B*, 1998, **102**, 4745–4752.

12 G. Huang, E. He, Z. Wang, H. Fan, J. Shangguan, E. Croiset and Z. Chen, *Ind. Eng. Chem. Res.*, 2015, **54**, 8469–8478.

13 P. G. Stansberry, J.-P. Wann, W. R. Stewart, J. Yang, J. W. Zondlo, A. H. Stiller and D. B. Dadyburjor, *Fuel*, 1993, **72**, 793–796.

14 Y. H. Lin, Y. C. Chen and H. Chu, *Chemosphere*, 2015, **121**, 62–67.

15 M. Mureddu, I. Ferino, E. Rombi, M. G. Cutrufello, P. Deiana, A. Ardu, A. Musinu, G. Piccaluga and C. Cannas, *Fuel*, 2012, **102**, 691–700.

16 R. Walker, A. D. Steele and T. D. B. Morgan, *Surf. Coatings Technol.*, 1988, **34**, 163–175.

17 S. Boursiquot, M. Mullet, M. Abdelmoula, J.-M. Génin and J.-J. Ehrhardt, *Phys. Chem. Miner.*, 2001, **28**, 600–611.

18 K. J. Cantrell, S. B. Yabusaki, M. H. Engelhard, A. V. Mitroshkov and E. C. Thornton, *Environ. Sci. Technol.*, 2003, **37**, 2192–2199.

19 J. Yu, J.-L. Shi, L.-Z. Wang, M.-L. Ruan and D.-S. Yan, *Mater. Lett.*, 2001, **48**, 112–116.

20 A. Galarneau, F. Villemot, J. Rodriguez, F. Fajula and B. Coasne, *Langmuir*, 2014, **30**, 13266–13274.

21 A. Hervault and N. T. K. Thanh, *Nanoscale*, 2014, **6**, 11553–11573.

22 D. W. Breck, *Zeolite Molecular Sieves: Structure, Chemistry and Use*, New York, John Wiley., 1974.

23 M. Jahandar Lashaki, M. Fayaz, S. Niknaddaf and Z. Hashisho, *J. Hazard. Mater.*, 2012, **241**–**242**, 154–163.

24 M. Hussain, N. Abbas, D. Fino and N. Russo, *Chem. Eng. J.*, 2012, **188**, 222–232.

25 C. Cannas, M. Casu, A. Lai, A. Musinu and G. Piccaluga, *J. Mater. Chem.*, 1999, **9**, 1765–1769.

26 M. Mureddu, I. Ferino, E. Rombi, M. G. Cutrufello, P. Deiana, A. Ardu, A. Musinu, G. Piccaluga and C. Cannas, *Fuel*, 2012, **102**, 691–700.

27 M. Mureddu, I. Ferino, E. Rombi, M. G. Cutrufello, P. Deiana, A. Ardu, A. Musinu, G. Piccaluga and C. Cannas, *Fuel*, 2012, **102**, 691–700.

28 L. Y. Chen, S. Jaenicke and G. K. Chuah, *Microporous Mater.*, 1997, **12**, 323–330.

29 C. M. Carbonaro, F. Orrù, P. C. Ricci, A. Ardu, R. Corpino, D. Chiriu, F. Angius, A. Mura and C. Cannas, *Microporous Mesoporous Mater.*, 2016, **225**, 432–439.

30 J. Trébosc, J. W. Wiench, S. Huh, V. S.-Y. Lin and M. Pruski, *J. Am. Chem. Soc.*, 2005, **127**, 3057–3068.

6. Effect of the different MCM41S porous structure and wall thickness on H_2S removal capacity

Abstract

In this chapter, the effect of the support pore structure (hexagonal and cubic) and of the wall thickness of the mesochannels have been evaluated aimed to achieve more and more efficient and regenerable iron oxide-based sorbents for H_2S at mid-temperature.

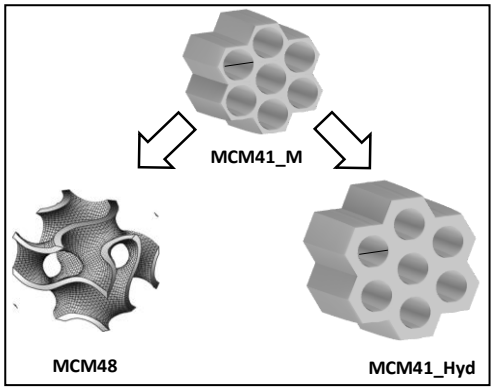

6.1 Introduction

The previous chapter points out as the best H_2S removal performance is achieved by the micrometric MCM41-based nanocomposites (Fe_MCM41_M). Starting from this promising result and focusing on MCM41S class of mesostructured supports, two further aspects have been evaluated with the aim of improving the sorbent's performance:

-the interconnection of the ordered mesopores by proposing MCM48 with 3D cubic structure (*Ia3d*) that in principle should improve the kinetic diffusion of H_2S molecules favouring the interaction with the active phase;

- the mesochannel wall thickness of MCM41 with hexagonal pore structure (*p6mm)*. Thicker silica walls should significantly improve the thermal stability during the repeated sulphidation and regeneration cycles.

With these purposes, we set up simple synthetic strategies capable to produce hexagonal and cubic pore structures without the use of Pluronics. Micrometric MCM48 support (MCM48) and micrometric MCM41 with thicker walls of the mesochannels (MCM41_Hyd) than MCM41_M, have been obtained following a simple Pluronics-free synthetic strategy and the performances of the corresponding nanocomposites have been correlated with the different textural properties.

6.2 Sorbent preparation

Two-Solvents impregnation method was selected to synthetize the corresponding composites with a 10% w/w of iron oxide active phase following the procedure describes elsewhere (Chapter 5, paragraph 2) . Table 6.1 reports the experimental details.

Sample	Support	Support amount (mg)	Support Pore volume (cm^3g^{-1})	Volume aqueous solution (µL)	$[Fe(NO_3)_3]$ in water	Fe_2O_3 (%w/w)
Fe_MCM41*	MCM41	0.19	0.76	167	1.5	9.6
Fe-MCM41_Hyd	MCM41_Hyd	0.20	0.69	138	1.99	9.8
Fe_MCM48	MCM48	0.11	0.83	97	1.48	9.6

Table 6.1 Experimental conditions for the Two-solvents impregnation route used to prepare Fe_MCM41S composites

6.3 Sorbent characterization

Figure 6.1a reports low-angle XRD of the composites (Fe_MCM41_Hyd, Fe_MCM48) and the corresponding supports (MCM41_Hyd, MCM48). In both composites, the support mesostructure is well retained after the impregnation and calcination procedures. The corresponding *d*-spacing (d_{100} and d_{211} for hexagonal and cubic structures, respectively) and cell parameters (a_0) have been calculated for each sorbent and reported in Table 6.2.

Figure 6.1b reports wide angle patterns of the bare MCM-41 (MCM41_Hyd) and MCM-48 (MCMC48) supports, and corresponding Fe_MCM41_Hyd and Fe_MCM48 nanocomposites. The typical broad reflection of the amorphous silica at about 22° is present in all the patterns, while two weak and broad additional reflexes at about 35° and 62°, corresponding to the Fe_2O_3 phase, are detected for the composites. These findings indicate that the reduced dimension of the pore intrinsically inhibits the growth of the crystalline phase, and indirectly proof that the iron oxide is efficiently dispersed into the pore structure. Considering the position of the two signals, as in the cases of Fe_SBA15 and Fe_MCM41_M composites (chapter 5), maghemite is the most probable phase, showing the most intense reflection at around 36° (PDF card #039-1346).[1,2]

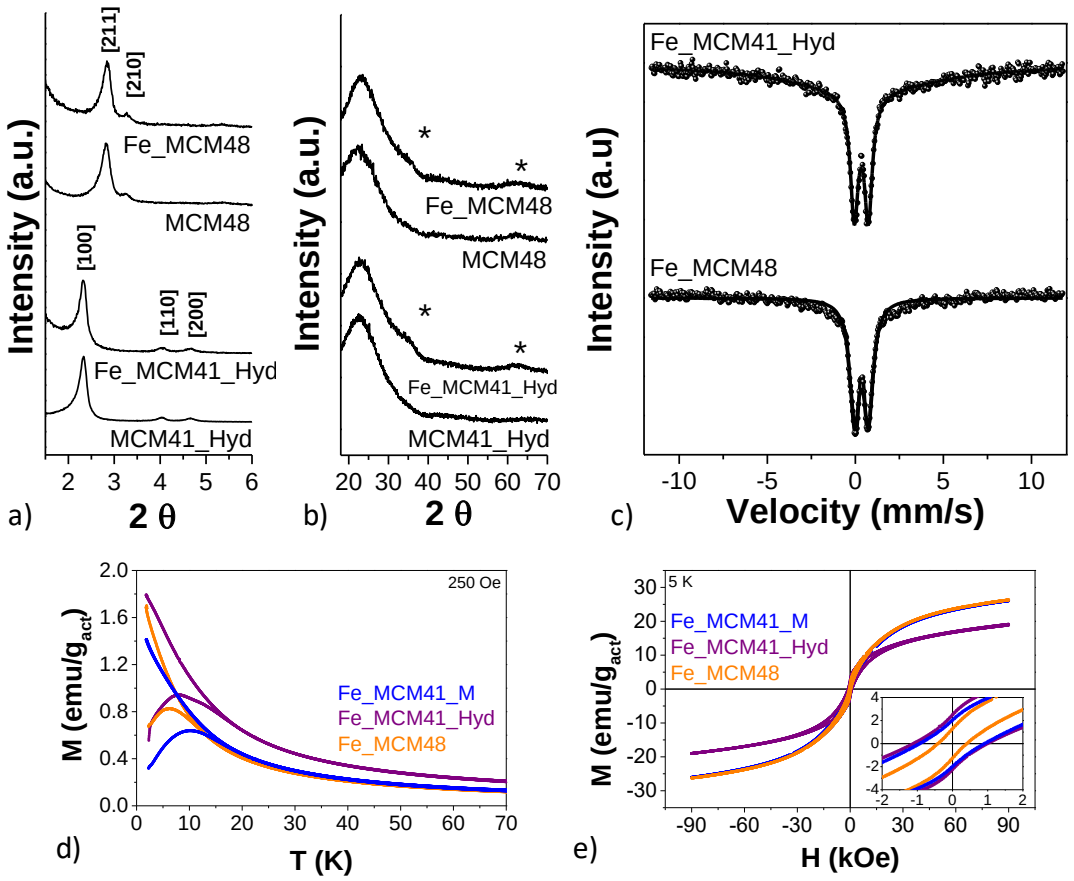

Figure 6.1 LA-XRD of bare supports and corresponding composites (a) WA-XRD patterns of bare Hex and Cub and different iron oxide based composites (Fe_MCM41_Hyd and Fe_MCM48 (b) and ^{57}Fe Mössbauer spectra of Fe_MCM41_Hyd and Fe_MCM48 (c) field dependence (d), and temperature dependence of the magnetisation for the sample Fe_MCM41_M, Fe_MCM41_Hyd and Fe_MCM48 (e)

Also in this case, room temperature (RT) ^{57}Fe Mössbauer Spectroscopy and DC-magnetometry point out that the active phase is in formed of ultrasmall maghemite nanoparticles, as already hypothesized for the Fe_SBA15 and Fe_MCM41_M sorbents (Figure 6.1c). Indeed, the Mössbauer data recorded on the Fe_MCM41_Hyd sample show a doublet with 0.34 ± 0.01 mm s^{-1} and 0.54 ± 0.01 mm s^{-1} for isomer shift and FWHM, respectively, close to the values found for the sample Fe_MCM41_M (IS of 0.34 ± 0.01 mm s^{-1} and FWHM of 0.49 ± 0.01 mm s^{-1}). The temperature and magnetic field dependences of the magnetization are also similar: similar shape and broadening of the peak in the ZFC curve centered at about 8 K and hysteretic behaviour with a coercivity value at about 1 kOe. Slight differences are found for the Fe_MCM48 composite that shows the same Mössbauer isomer shift value but a higher FWHM value (0.65 ± 0.01 mm s^{-1}). The latter together with the magnetic data, as the lower temperature of the ZFC maximum (6 K) and the smaller coercivity (about 0,4 KOe) suggest the presence of slightly smaller maghemite particles in comparison with the others MCM41

(MCM41, MCM41_Hyd) sorbents and the narrower peak in the ZFC curve indicates a narrower particle size distribution.

Figure 6.2a, d reports representative TEM images of the composites Fe_MCM41_Hyd and Fe_MCM48, respectively. Micrometric particles are observed for each composite, and, in agreement with LA-XRD and N2-physisorption data, the presence of a well ordered porous structure with pores dimension in the 2-3 nm range is confirmed.

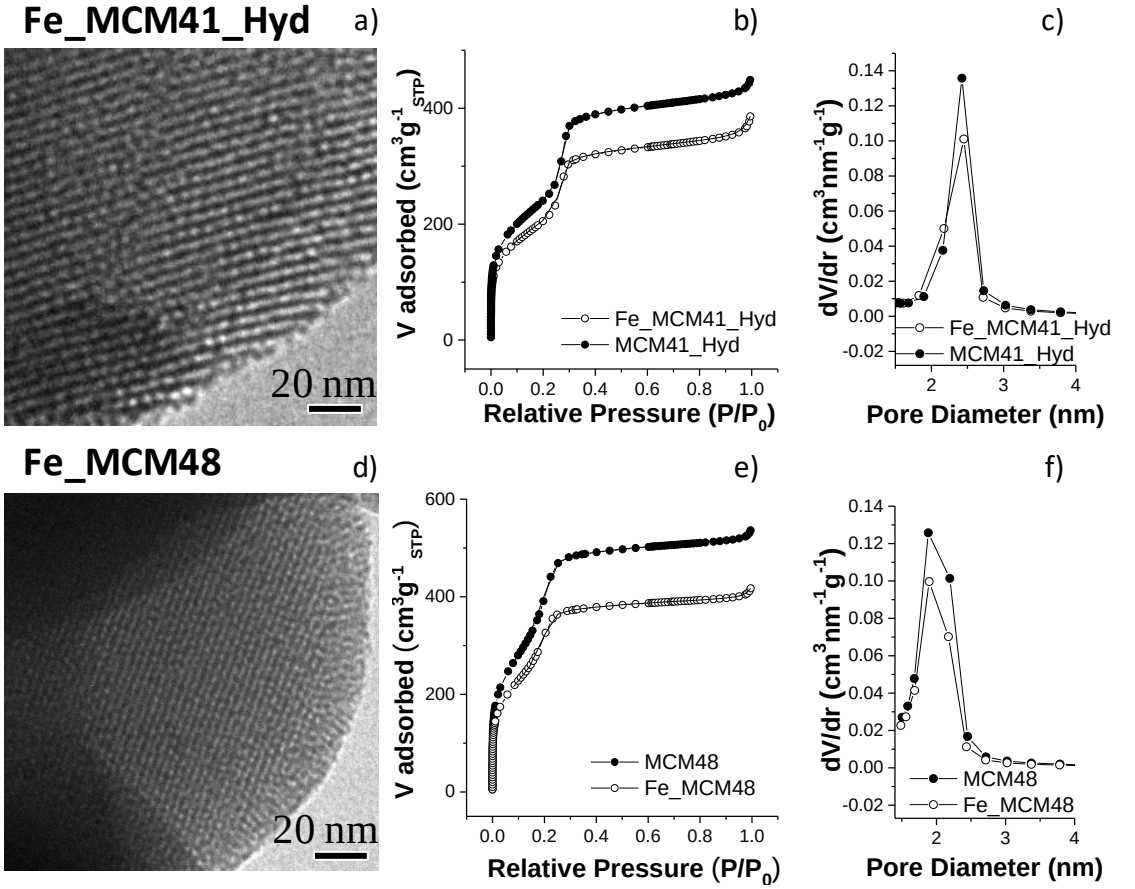

Figure 6.2 Bright field TEM image of Fe_MCM41 _Hyd (a) and Fe_MCM48 (d)**.** N_2 adsorption-desorption isotherms and pore size distributions of the composites Fe_MCM41_Hyd (b, c), Fe_MCM48 (e, f) and of their corresponding bare supports.

Figure 6.2b-e reports the nitrogen adsorption-desorption isotherms of both MCM41_Hyd and MCM48 supports and of the relative composites. The textural parameters of the different samples are listed in Table 6.2. The composites (Fe_MCM41_Hyd and MCM48_Cub) retain the same characteristic IVB type isotherm behaviour of their corresponding supports:[3] besides the microporous contribution, the presence of mesopores is clearly indicated by the existence of a well-defined step in the 0.2-0.4 P/P_0 range as a consequence of the capillary condensation. However, the functionalization of the support, although does not influence the pore

dimension, leads to an expected reduction in the surface area values, as well as the pore volume (Table 6.2) mainly due to a significant decrease in the extent of mesopores adsorption.

Sample	S_{BET} (m^2g^{-1})	V_p (cm^3g^{-1})	D_{pore} (nm)	w_t (nm)	d_{100} (MCM 41) or d_{211}(MCM 48) (nm)	a_0 (nm)
MCM41_M*	1063	0.76	2.2	1.7	3.5	4.0
MCM41_Hyd	877	0.69	2.4	2.0	3.8	4.4
Fe_MCM41_Hyd	744	0.60	2.4	2.0	3.8	4.4
MCM48	1336	0.83	2.1	1.4	3.1	7.7
Fe_MCM48	911	0.65	2.1	1.4	3.1	7.6

Table 6.2 Textural features obtained by N_2-physisorption data for the supports and the corresponding composites. S_{BET}=Surface area; V_p=Pore volume; D_p=pore diameter; $V_{tot\ t\text{-}plot}$: total volume calculated by *t-plot* graphs; $V_{micro\ t\text{-}plot}$: microporous volume calculated by *t-plot* graphs. Relative standard deviation: %RSD(S_{BET})=2.1%; %RSD(V_p)=1.1%; %RSD(D_p)=1.8%. d-spacing (d_{100} and d_{211} for hexagonal and cubic structure, respectively) and lattice parameter (a_0) obtained from the LA-XRD data *for comparison, textural values of MCM41_M have been reported

6.4 Sulphidation and regeneration processes

6.4.1 Sulphidation runs

For each sorbent, three sulphidation runs have been carried out (breakthrought curve in Figure 6.3) and the corresponding B_t and SRC values are reported in Table 3. In order to study the effect of the different textural properties (wall thickness and porous structure) the sorbent with hexagonal pore structures sumitted to a hydrothermal treatment (Fe_MCM41_Hyd) and the one with cubic pore structure (Fe_MCM48) have been compared with the Fe_MCM41 sorbent. (Table 6.3).

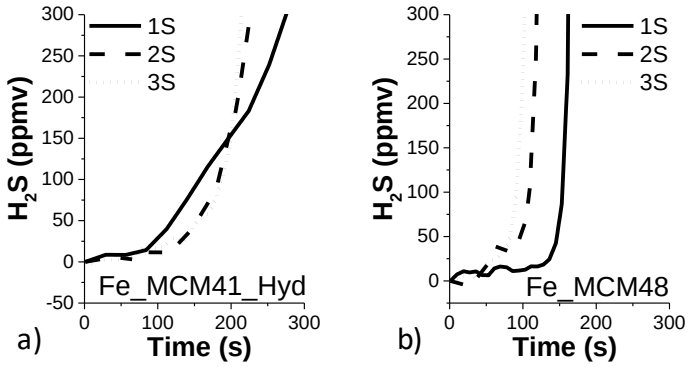

Figure 6.3 H_2S breakthrough curves for three sulphidation–regeneration cycles (1S = first sulphidation, 2S = second sulphidation; 3S = third sulphidation) for the sample Fe_MCM41_Hyd (a), Fe_MCM48 (b)

Sample	Sulphidation run	B_t (s)	SRC ($mg_S\ g_{sorbent}^{-1}$)
Fe_MCM41_M*	1st	295	38*
Fe_MCM41_M _R1	2nd	169	22*
Fe_MCM41_M _R2	3rd	169	22*
Fe_MCM41_Hyd	1st	123	17
Fe_MCM41_Hyd_R1	2nd	161	21
Fe_MCM41_Hyd_R2	3rd	160	21
Fe_MCM48	1st	128	17
Fe_MCM48_R1	2nd	98	13
Fe_MCM48_R2	3rd	84	11

Table 6.3 Breakthrough time (Bt) and sulphur retention capacity (SRC) of fresh and regenerated iron oxide-based sorbents. R1 and R2 refer to the first regeneration and the second regeneration, respectively. The error in SRC value is estimated to be ± 2 mgS $g_{sorbent}^{-1}$

The composite Fe_MCM41_Hyd, shows that SRC value of the first sulphidation run (17 $mg_s sorbent^{-1}$) is slightly lower than those obtained for the other two cycles (21 $mg_s sorbent^{-1}$). Although the composite Fe_MCM48 shows a similar SRC value for the first sulphidation a gradual worsening of the performance is observed during the successive two sulphidatation (13 $mg_s sorbent^{-1}$ and 11 $mg_s sorbent^{-1}$). Taking into account the average value of the last two SRC values of each sorbent, Fe_MCM41_Hyd composite shows SRC value very similar to that of the Fe_MCM41 and almost double than the Fe_MCM48.

6.4.2 Regeneration runs

The regeneration process, carried out at 500°C in air, as described in Chapter 5, paragraph 4.2, has been monitored by both a thermal conductivity detector (TCD) and a quadrupole mass spectrometer (QMS). A similar behaviour has been revealed for all the regeneration runs, therefore here, as an example, only the first one is reported for each sorbent in Figure 6.4.

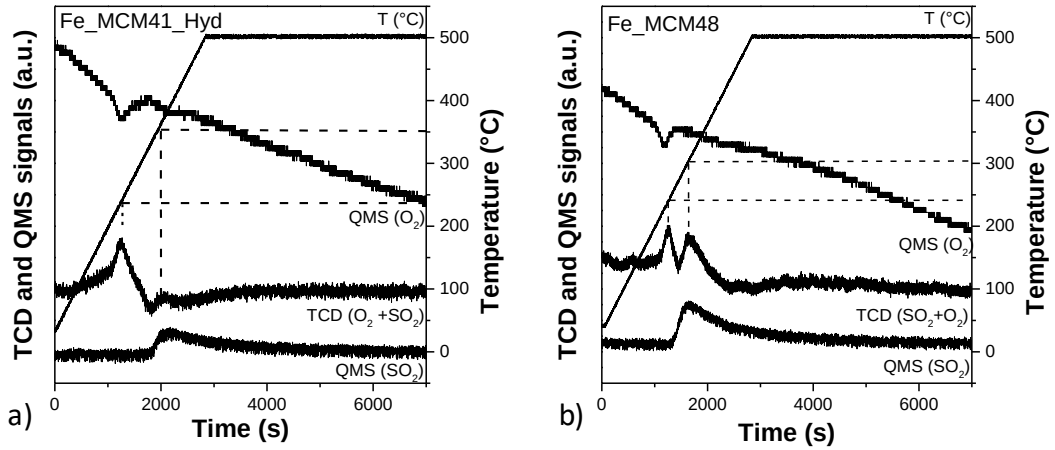

Figure 6.4 TCD profile and SO_2 and O_2 Quadrupole Mass Spectrometer (QMS) signals of Fe_MCM41_Hyd (a) and Fe_MCM48 (b) during the first regeneration run.

The TCD profiles of the two sorbents are characterized by the presence of a first main peak centred at about 250 °C, corresponding to the O_2 consumption (upper curve, QMS (O_2)), and a second one due to a release of SO_2, as confirmed by the QMS (SO_2) bottom curve at about 300°C for Fe_MCM48 and 350°C for Fe_MCM41_Hyd, respectively.

6.5 Regenerated sorbents characterization

The textural properties of the three times sulphidated-regenerated sorbents (Fe_MCM41_Hyd_R3 and Fe_MCM48_R3) have been verified by N_2-physisorption and LA-XRD measurements and the results have been compared with those of the fresh sorbents (Figure 6.5and Table 6.4). The retention of the porous structure on the Fe_MCM41_Hyd_R3 is confirmed by the pore size distribution (Figure 6.5c) and LA-XRD patterns (Figure 6.5a), in which the presence of three reflexes is still well evidenced. However, a slight decrease of around 20% of the surface area and pore volume have been observed, as reported in Table 6.4. *t-plot* graph (Figure 6.6a) evidences a decrease of the total volume ($V_{tot\ t\text{-}plot}$, see Table 3) accompanied by an constant microporous volume, demonstrating a reduction on the mesoporous contribution.

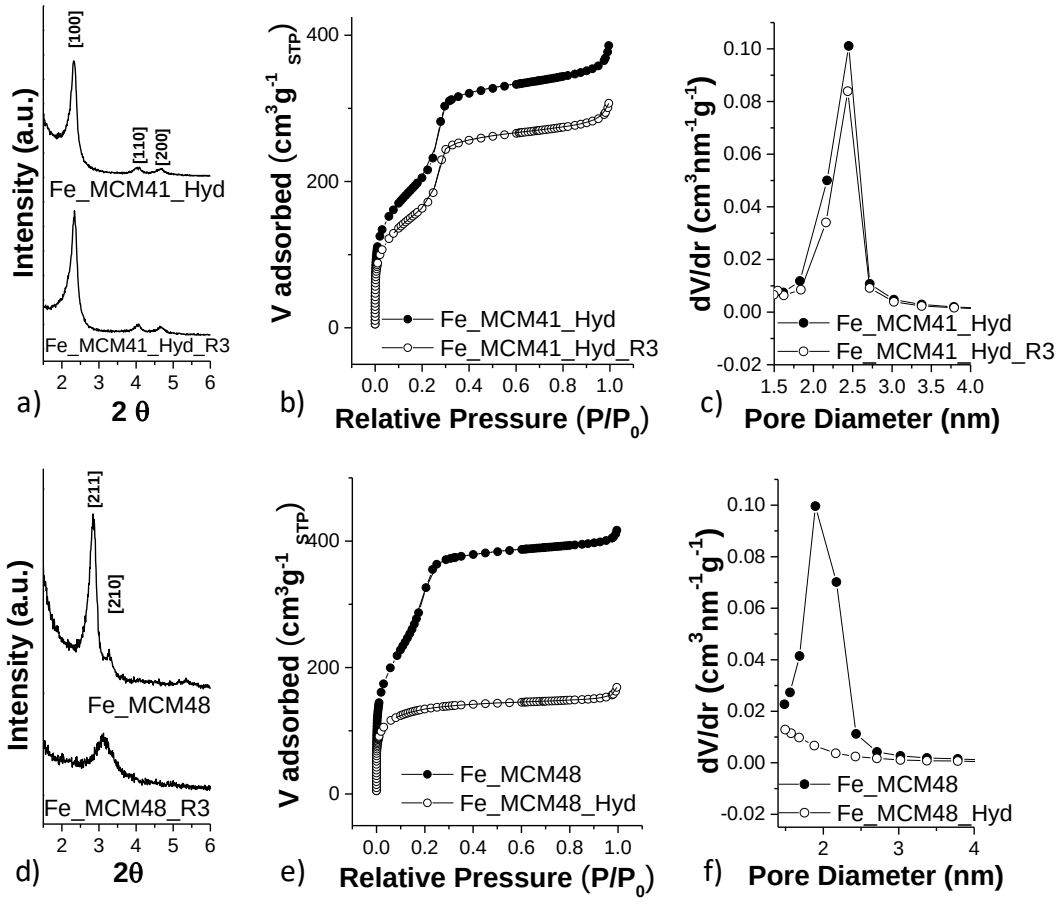

Figure 6.5 N_2 adsorption-desorption isotherms, pore size distributions and low angle XRD of: Fe_MCM41 and Fe_MCM41_R3 (a, b, c); Fe_MCM48 and Fe_MCM48_R3 (d, e, f)

Conversely, an almost complete structural collapse is observed for Fe_MCM48_R3 by LA_XRD and pore size distribution (Figure 6.5d, f) and also by the absence of the capillary condensation due to mesopores. (Figure 6.5e).

Sample	S_{BET} (m^2g^{-1})	V_p (cm^3g^{-1})	$V_{tot\ t\text{-}plot}$ (cm^3g^{-1})	$V_{micro\ t\text{-}plot}$ (cm^3g^{-1})	D_{pore} (nm)	w_t (nm)	d_{100} d_{211}	a_0
Fe_Hex_Hyd	744	0.60	0.48	0.01	2.4	2.0	3.80	4.4
Fe_Hex_Hyd_R3	593	0.47	0.40	0.01	2.4	2.0	3.80	4.4
Fe_Cub	911	0.65	0.57	0.02	2.1	1.4	3.10	7.6
Fe_Cub_R3	482	0.26	0.21	0.04	-	-	2.84	7.0

Table 6.4 Textural features obtained by N_2-physisorption data for fresh and three times-regenerated composites. d-spacing (d_{100} and d_{211}) and lattice parameter (a_0) obtained from the LA-XRD data

In this case, *t-plot* graph (Figure 6.6b) permits to better clarify the typology of pores involved in the collapse phenomena. Beside the complete absence of the capillarity condensation a gradual increase of the microporous volume is detected, probably due to the formation of new micropores as a consequence of the collapse of the mesopores.

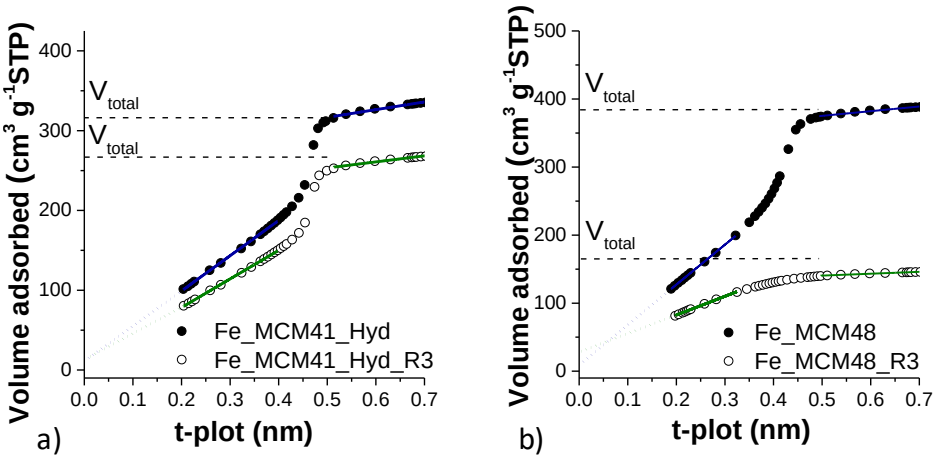

Figure 6.6 *t-plot* graph of the samples Fe_MCM41_Hyd and Fe_MCM41_Hyd_R3 (a); Fe_MCM48 and Fe_MCM48_R3 (b). The intercept of the dashed blue line with the y-axis provides an estimation of the total porous volume, while the intercept of the green line provides an estimation of the microporous volume

6.6 Discussion

Mesostructured γ-Fe_2O_3@MCM-41 composites have already been proved to be promising sorbents for H_2S removal at mid-temperature due to the high surface area and the homogenous dispersion of ultrasmall particles of maghemite within the small mesopores. Starting from this finding, in order to improve the H_2S removal performance, the attention has been focalized on the increase of the pore interconnection to improve the accessibility, and to the strengthen of the pore structure in order to improve the lifetime of the sorbent. For these purposes, a bicontinuous pore structure has been achieved by a free-Pluronics synthetic pathway, in which ethyl acetate has been properly added to CTAB in hydro-ethanolic media, while a more robust porous structure has been obtained by some modifications of the strategy proposed for MCM41. The two supports have been used to develop the corresponding Fe_2O_3 composites and tested as H_2S remover at mid temperature and compared with the reference one (MCM41_M). The comparison (Figure 6.7a) pointed out that the bi-continuous porous structure, that theoretically should lead to an improvement in the sulphur retention capacity of the sorbent, leads to the worst performance. In fact, even though the Fe_MCM48 sorbent has shown the highest surface area and a high SRC in the first sulphidation cycle a gradual worsening in the H_2S removal performance was detected. This behaviour can be probably explained considering its *fragile* pore structure built up of very thin silica walls (1.4 nm) if compared with the other two sorbents (1.7 nm and 2.0 nm for MCM41_M and MCM41_Hyd, respectively), that collapse almost completely after repeated sulphidation and regeneration cycles. The gradual SRC decrease is also consistent with the water release profile during the

three sulphidation runs (Figure 6.7b): a significant broadening of the water band is evident suggesting as diffusion phenomena become more and more important.

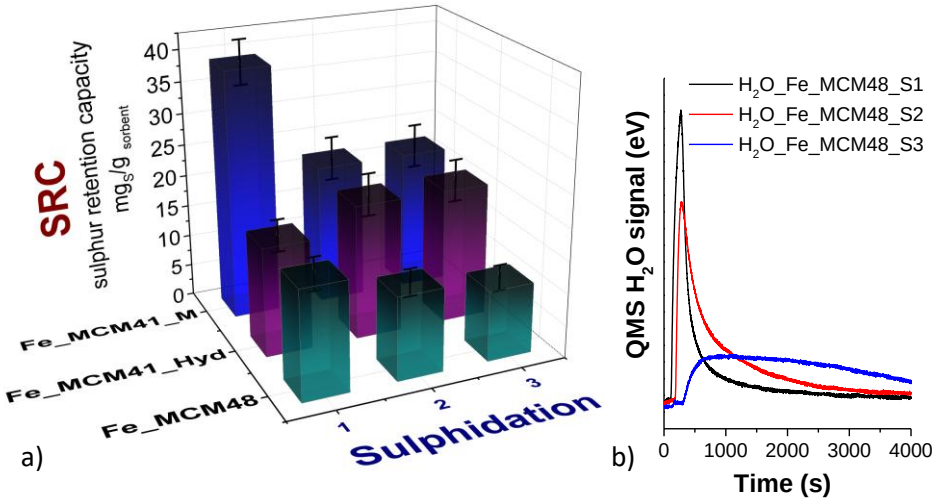

Figure 6.7 SRC values of Fe_MCM41_M, Fe_MCM41_Hyd and Fe_MCM48 sorbents (a); water release of Fe_MCM48 during the first (H_2O_Fe_MCM48_S1), second (H_2O_Fe_MCM8_S2) and third (H_2O_Fe_MC48_S3) sulphidation runs (b).

Taking into account the importance of the walls thickness on the lifetime of the sorbent, we tried to render MCM41_M more robust. Commonly, in order to strengthen the porous structure, an additional hydrothermal treatment is applied during the synthesis of the mesostructured MCM41.[4,5] Moving in this direction, the synthetic strategy used for hexagonal sample (MCM41_M) was modified adding a further hydrothermal treatment at 100 °C for 24 hours. The effects were a significant increase in both the walls thickness (from 1.7 to 2.0 nm) and pores size (from 2.2 to 2.4 nm). The comparison of the SRC of the two hexagonal sorbents (Fe_MCM41 and Fe_MCM41_Hyd) highlighted similar performances except for the first sulphidation run. Even if a gradual decrease of the SRC values over successive cycles is expected due to different phenomena (uncompleted regeneration of the active phase, sintering of the particles or a gradual collapse of the silica matrix) different trends can be found in the literature. For example, ZnO@SBA15 sorbents showed a remarkable increase of SRC after the first sulphidation,[6] Fe_2O_3 on SBA-15 as well as on MCM41, showed in some cases the expected trend, with a gradual decrease of the SCR, in others a steady trend.[2] These findings can be explained by taking into account the possible differences in terms of active phase crystallinity, particles dimension, interaction with the matrix, sintering phenomena induced by the repeated cycles. A first difference should derive from the different features (crystallinity, particle size, reactivity with H_2S) of the fresh active phase obtained by decomposition of the metal nitrate precursor, with the one achieved from the gas solid

reaction between the regenerating gas, and the sulphide derived material. Secondly, the presence of water that easily can be adsorbed at the surface of this type of materials, could also influence the sorbent's performance. Aware of this, a pre-treatment at 120 °C for 48 hours has been applied for each sorbent before loading the reactor, followed by a further treatment at 300°C under helium flow before the H_2S test. However, considering that DFT calculations showed similar binding energies of H_2S and H_2O with some metal oxide as Cu and Fe,[7] even a small content of water can affect the SRC values. In our conditions, sintering and unreacted-core phenomena should be hampered due to the low active phase loading, small pore size and high surface area of the support that assure a high spread ultrasmall nanoparticles into the matrix. Therefore, it is more proper to compare the sulphidation cycles subsequent to the first one. Considering these points, the H_2S removal performances of the two sorbents (MCM41 and MCM41_Hyd) can be considered very similar having SRC of 22 and 21 mg_s $sorbent^{-1}$, respectively. This can be justify considering the similarities on the pore diameter and wall thickness as well as on the particle size and crystallinity of the active phase. The decrease on the surface area due to the hydrothermal restructuring does not seems to be detrimental for the dispersion of the phase, being the textural features suitable to disperse efficiently such low amount of the active phase.

6.7 Conclusion

In this chapter, it is proved that, other factors besides surface area (higher than 700 m^2/g) pore diameter (about 2 nm) and particle size (micrometric) of the support, crystallographic phase (maghemite) and particle size (about 2 nm) of the active phase, have to be optimized in order to design an efficient and regenerable sorbent of H_2S removal. In fact, although the significant differences on the surface area of the three selected supports (MCM41_M, MCM41_Hyd and MCM48), all the values are high enough to disperse homogeneously the active phase, being the loading quite low (10% w/w). Considering the similarities of the three sorbents in the other features (pore diameter and particle size of the support, crystallographic phase and particle size of the active phase), the performances could be justified in the light of the different pores structure or wall thickness. However, the exclusive effect of changing the porous structure from hexagonal (MCM41) to cubic (MCM48) cannot be evaluated due to the contemporary reduction on the walls thickness from 2 nm to 1.4 nm, that causes the collapse of the structure. Therefore, the fragility of the porous structure prevails on the possible effect deriving from the interconnection of the pores typical for a cubic structure. In the light of these results, the strengthening of the porous structure represents another key aspect to be considered in the development of long lifetime sorbent. In this context, even if the two

MCM41 sorbents show very similar performances in all the three cycles, the one showing thicker should guarantee steady performances for a higher number of cycles.

References

1 M. Mureddu, I. Ferino, A. Musinu, A. Ardu, E. Rombi, M. G. Cutrufello, P. Deiana, M. Fantauzzi and C. Cannas, *J. Mater. Chem. A*, 2014, **2**, 19396–19406.

2 C. Cara, E. Rombi, A. Musinu, V. Mameli, A. Ardu, M. Sanna Angotzi, L. Atzori, D. Niznansky, H. L. Xin and C. Cannas, *J. Mater. Chem. A*, 2017, **5**, 21688–21698.

3 M. Thommes, K. Kaneko, A. V. Neimark, J. P. Olivier, F. Rodriguez-Reinoso, J. Rouquerol and K. S. W. Sing, *Pure Appl. Chem.*, 2015, **87**, 1051–1069.

4 M. Kruk, M. Jaroniec and A. Sayari, *Adsorption*, 2000, **6**, 47–51.

5 P. Van Der Voort, M. Mathieu, F. Mees and E. F. Vansant, *J. Phys. Chem. B*, 1998, **102**, 8847–8851.

6 M. Mureddu, I. Ferino, E. Rombi, M. G. Cutrufello, P. Deiana, A. Ardu, A. Musinu, G. Piccaluga and C. Cannas, *Fuel*, 2012, **102**, 691–700.

7 M. S. Shah, M. Tsapatsis and J. I. Siepmann, *Chem. Rev.*, 2017, **117**, 9755–9803.

7. H_2S removal from sour syngas by iron oxide-based MCM41 and TiO_2 sorbents

Abstract

This chapter aims to verify whether MCM41-based sorbents can be actually proposed as efficient systems in conditions that better simulate the real sour syngas. Among the different silica based sorbents tested in H_2S/He atmosphere, Fe_MCM41_Hyd was chosen, owing to its high and steady performance together with its potentiality to be used for repeated cycles. In addition, in order to study the effect of the chemical nature of the support a new sorbent in which the active phase is dispersed in mesotructured crystalline titania (Fe_TiO_2) is studied.

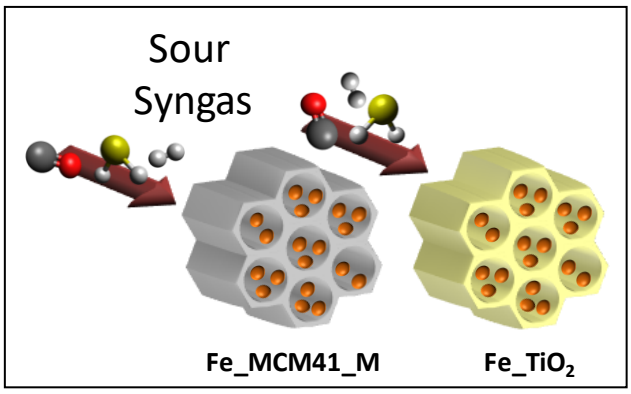

7.1 Introduction

In order to prove that the promising sorbents tested in H_2S/He atmosphere can be proposed for the selected application, the further step was the use of a simulated sour syngas containing CO, H_2, H_2S, and N_2 (CO 24.88% H_2 14.84 %H_2S 1.52 % in N_2). In this condition, it should be possible to evaluate eventual concomitant reactions of the active phase with the other gaseous species present in the syngas. The characterization by ^{57}Fe Mössbauer Spectroscopy and magnetic measurements has pointed out that iron oxide in all the mesostructured silica-based sorbents is present in the form of ultrasmall maghemite nanoparticles, the iron oxide crystallographic phase that has been declared to be the most active for H_2S removal.[1] Although the difficulties in studying such diluted and ultrasmall nanoparticles, some interesting aspects have been evidenced: the particle size is not strictly related to the pore size and surface area, but other factors such as the silanol species distribution, the hydrophilicity of the silica surface, the interaction of the silanol groups with the metal cations, as well as the concentration of the iron (III) precursors used during the impregnation process can influence the final

crystallinity/particle size of the active phase (Chapter 5, paragraph 3). Considering these aspects, and how the dispersion of the active phase into the matrix can affect the performances of the sorbents, we decided to propose a mesostructured support with a different chemical nature, with the intent to act on the different capacity to interact with and disperse the active phase. Inspired by this idea, mesostructured anatase was chosen to build up the corresponding iron oxide composites. The important differences between silica-based and titania-based supports, in terms of type of surface atoms and crystallinity (silica is amorphous, titania is crystalline) should strongly influence the interaction between the iron precursor and support surface during the impregnation step, causing remarkable differences in terms of distribution of the active phase into the support and particle size. To the best of the author's knowledge, this is the first example of synthesis and application of Fe_2O_3@TiO_2 nanocomposite in which titania is in form of mesostructured anatase.

In the previous chapters, it was found that among the different tested sorbents, Fe_MCM41_M and Fe_MCM41_Hyd show the best SRC values. Between these two, being the SRC equal within the experimental error, the sorbent Fe_MCM41_Hyd with thicker silica walls was selected because it can assure, at least in principle, a better stability in a high number of sulphidation and regeneration cycles. Furthermore, an iron oxide nanocomposites (Fe_TiO_2) built up with mesostructured anatase as support is studied in order to verify the effect of the chemical nature of the matrix on the sorbent's performance.

Support	Surface Area (m^2g^{-1})	Pore volume (cm^3g^{-1})	Pore diameter (nm)	Thermal stability	Porous structure	Space group	Walls thickness (nm)	Support particle size
MCM41_Hyd	877	0.69	2.4	up to 600°C	Hexagonal	*P6mm*	2.0	micrometric
TiO_2*	274	0.3	3.9	up to 400°C	Hexagonal	*P6mm*	4.8	micrometric

Table 7.1 Main features of the selected silica and titania supports for the development of the corresponding iron oxide-based sorbents. *TiO_2 corresponds to the sample previously labelled TiO_2_$450N_2$_$360O_2$

7.2 Sorbent preparation

The preparation of the new mesostructured sorbent (Fe_TiO_2) was performed following the *Two-Solvents* impregnation approach described for the preparation of silica based nanocomposites (see Chapter 5, paragraph 2). The calcination step, being the thermal porous structure stability of titania assured at temperatures below 360 °C (see Chapter 4, paragraph 3.1.1), in this case was carried out at 350 °C (heating rate 2 °C min^{-1}) under static air for 2

hours. Table 6.1 reports the synthetic conditions for the impregnation procedure of Fe_TiO_2, and for comparison those used for Fe_MCM41_Hydr.

Sample	Support	Support amount (mg)	Support Pore volume (cm^3g^{-1})	Volume aqueous solution (μL)	$[Fe(NO_3)_3]$ in water	Fe_2O_3 (w/w)%
Fe_TiO_2	TiO_2*	0.15	0.34	51	4.01	9.9
Fe_MCM41_Hyd	MCM41_Hyd	0.2	0.69	138	1.99	9.8

Table 7.2 *Two-Solvents* impregnation conditions for Fe-Tio2 and Fe_MCM41_Hyd. *TiO_2 corresponds to the sample previously labelled TiO_2_450N_2_360O_2

7.3 Sorbent characterization

In Figures 1 and 2, the characterization of Fe_TiO_2 is reported and compared with TiO_2 support, being Fe_MCM41_Hyd already studied in chapter 6, paragraph 3. LA-XRD pattern (Figure 7.1a) of the composite confirms the well-ordered porous structure (space group *p6mm*) of the anatase support, even if a slight shift of the main reflex is detected. The corresponding *d*-spacing, and cell parameters (a_0) have been calculated and reported in Table 6.2. WA-XRD patterns (Figure 7.1b) of the bare TiO_2 and Fe_TiO_2 are almost completely overlapped: the most intense reflexes are ascribable to anatase phase (space group $I4_1$ PDF card N. 084-1286) with crystallite dimension of 4.3 ± 0.5 nm while two further weak and broad contributions (indicated with the symbol * in the graph) can be assigned to a certain amount of carbonaceous residues deriving from the pyrolysis. This is confirmed by the absence of these reflexes in the WA-XRD pattern of the TiO_2_400O_2, that was submitted to the same pyrolysis treatment (450°C in N_2) but at a higher calcination temperature (400°C in place of 360 °C). Contrary to the silica composites, in this case no weak and broad reflexes ascribable to the iron-based phase are visible, indicating the possible formation of an amorphous phase or small clusters, not detectable with conventional WA-XRD equipment.

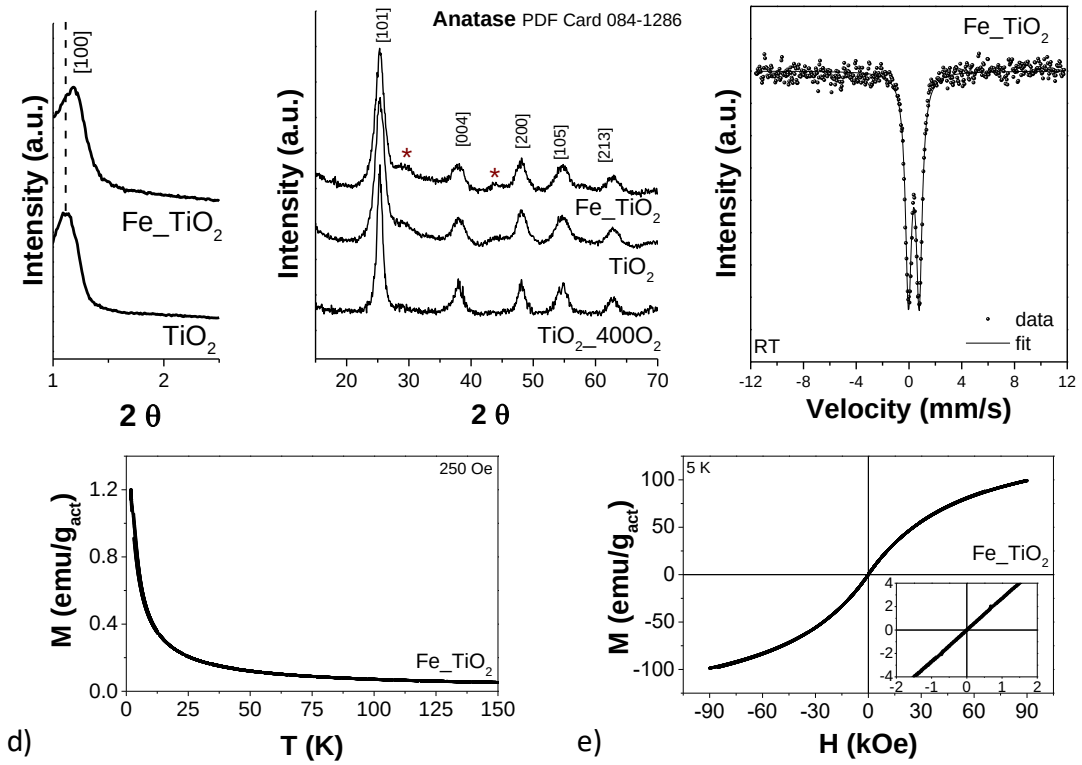

Figure 7.1 LA-XRD (a) and WA-XRD (b) patterns of bare TiO_2 and Fe_ TiO_2, ^{57}Fe Mössbauer spectrum (c), magnetic field (d) and temperature (e) dependences of the magnetisation for the sample Fe_ TiO_2.

^{57}Fe Mössbauer spectrum recorded at room temperature shows symmetric sharp doublet (FWHM 0.55 mm/s), that on the bases of the isomer shift (0.37 mm/s) and quadrupole splitting (0.81 mm/s) can be ascribed to the presence of Fe^{3+} with octahedral coordination. These features can be ascribed to hematite ultrasmall particles with dimension of 1-2 nm because of the very sharp doublet or to the formation of a solid solution with titania to form a ternary compound with Fe^{3+}.[2] DC magnetic measurements confirm this scenario: ZFC-FC curves show a complete overlapping of the magnetization values and *M vs H* curves at 5 K highlight the absence of hysteretic behaviour (coercivity and remanent magnetization equal to zero). The S-shape of the curves can be associated with an uncompleted antiferromagnetic order, or a paramagnetic phase. All these findings lead to exclude the formation of a ferro-ferrimagnetic phase as in the case of siliceous sorbents, and to hypothesize the formation of ultrasmall antiferromagnetic particles or Fe-doped TiO_2.[3]

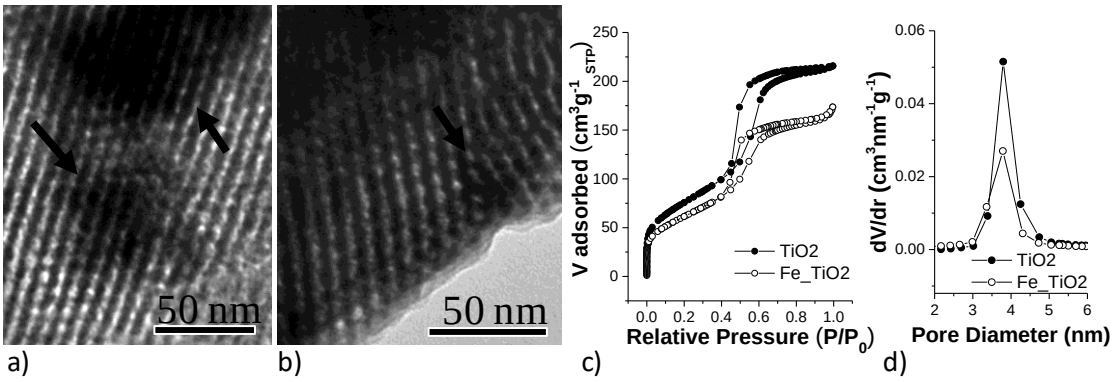

Figure 7.2 Bright field TEM images of Fe_TiO_2 (a, b). N_2 adsorption-desorption isotherms (c) and pore size distributions (d) of the Fe_TiO_2 composite and its corresponding support

Figure 7.2a, b reports representative TEM images of the composite Fe_TiO_2, in which the ordered porous structure is well visible. Although the difficulties in evidencing the incorporation of other phases inside such 3D mesostructures, a lower contrast between the crystalline walls is visible in some portions of the sample (see dark arrows), suggesting the presence of another phase inside the pores. N_2 adsorption-desorption isotherms of TiO_2 support and relative composite (Fe_TiO_2) (Figure 7.2c) highlight that the characteristic IVA type isotherm is maintained after impregnation and calcination, due to the clear presence of capillary condensation in the range 0.5-0.7 P/P_0 and the H1 type hysteresis loop.[4] However, the impregnation process induces, as expected, a reduction in the surface area, as well as in the pore volume (Table 6.2) mainly due to the decrease in the extent of mesopores adsorption. Pore size distribution (PDS) calculated on the desorption branch points out that the dimension of the pores in the composite is still centred at 3.8 nm.

Sample	S_{BET} (m^2g^{-1})	V_p (cm^3g^{-1})	D_{pore} (nm)	w_t (nm)	d_{100} (nm)	a_0 (nm)
TiO_2	274	0.33	3.9	4.8	7.5	8.7
Fe_TiO_2	223	0.24	3.8	4.8	7.5	8.7

Table 7.3 Textural features obtained by N_2-physisorption data for the support (TiO_2) and the corresponding composite (Fe_TiO_2). S_{BET}=Surface area; V_p=Pore volume; D_p=pore diameter. Relative standard deviation: %RSD (S_{BET})=2.1%; %RSD(V_p)=1.1%; %RSD(D_p)=1.8%. The last two columns list the d-spacing (d_{100}) and lattice parameter (a_0) obtained from the LA-XRD data

7.4 Sulphidation and regeneration processes

7.4.1 Sulphidation runs under sour syngas

In order to test the H_2S performances under a simulated sour syngas containing 1.52 vol % H_2S (15 200 ppm), 24.88 vol % of CO and 14.84 vol % H_2, three repeated sulphidation runs (Figure

7.3) at mid-temperature (300 °C) have been carried out on the selected two sorbents (Fe_MCM41_Hyd and Fe_TiO_2).

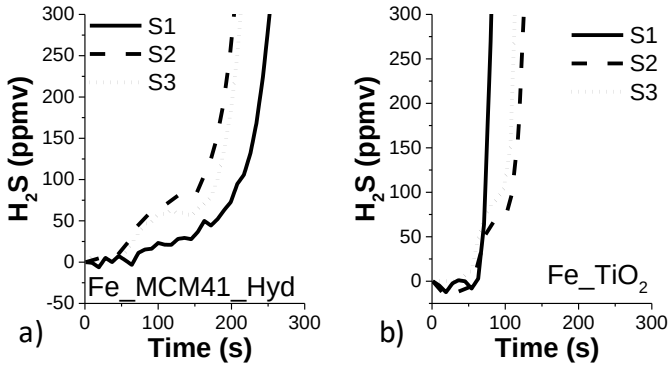

Figure 7.3 H_2S breakthrough curves upon three sulphidation–regeneration cycles (1S = first sulphidation, 2S = second sulphidation; 3S = third sulphidation) for the sample Fe_MCM41_Hyd (a), Fe_TiO_2 (b)

Sample	Sulphidation run	B_t (s)	SRC ($mg_S\ g_{sorbent}^{-1}$) (under sour syngas)	SRC ($mg_S\ g_{sorbent}^{-1}$) (under H_2S/He)*
Fe_MCM41_Hyd	1st	187	25	17
Fe_MCM41_Hyd_R1	2nd	136	18	21
Fe_MCM41_Hyd_R2	3rd	156	20	21
Fe_TiO_2	1st	48	6	-
Fe_TiO_2_R1	2nd	85	11	-
Fe_TiO_2_R2	3rd	70	9	-

Table 7.4 Breakthrough time (Bt) and sulphur retention capacity (SRC) of fresh and regenerated iron oxide-based sorbents. R1 and R2 refer to the first and second regeneration, respectively. The error in SRC value is estimated to be ± 2 $mg_S\ g_{sorbent}^{-1}$. *For comparison, SRC values obtained under H_2S / He flow has been reported for the Fe_MCM41_Hyd composite.

The SRC values (Table 4) evidence that the best sulphidation performance is reached for Fe_MCM41_Hyd, in which the SRC value results to be about 4 times and 2 times higher than that for Fe_TiO_2, for the first and the successive sulphidation, respectively. The comparison between the SRC obtained under sour syngas with those under H_2S, points out that, keeping out the first sulphidation that can be considerate unreliable, the performances are very similar.

Even if the SRC values obtained under sour syngas are very similar to those obtained under H_2S/He flow, considering the strong reducing environmental of the syngas, it is reasonable to think that different reactions can take place during the sulphidation runs. Therefore, in order to get more information about these possible reactions different gas species (CO, CO_2, H_2, H_2O)

were monitored by QMS. The profiles reported in Figure 7.4 are normalized in order to catch the variations.

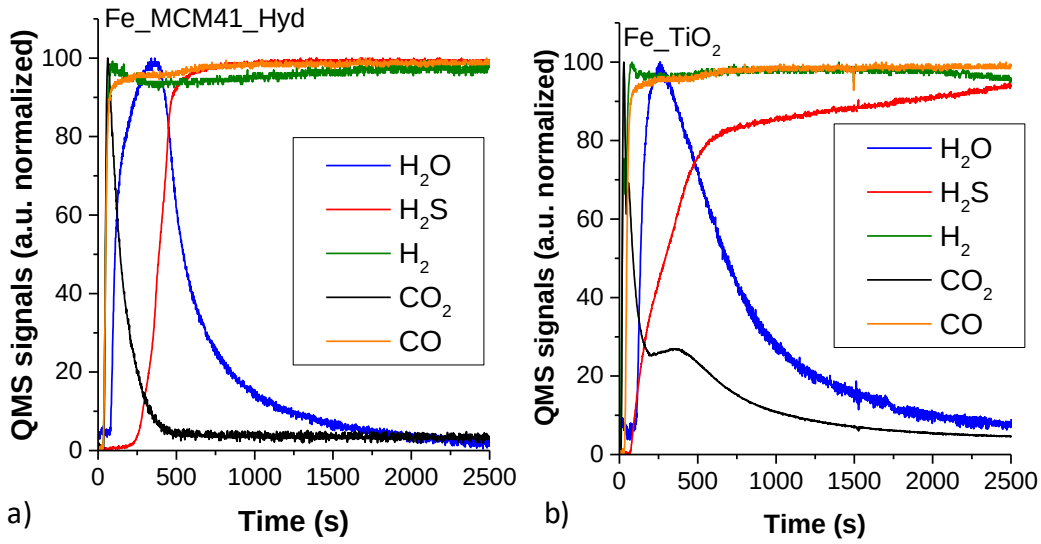

Figure 7.4 H_2O, H_2S, H_2, CO_2 and CO normalized Quadrupole Mass Spectrometer (QMS) profiles during the first sulphidation of the samples Fe_MCM41_Hyd (a), Fe_TiO_2 (b)

The gases profiles of the two sorbents are quite different. Fe_MCM41_Hyd composite shows a sharp peak ascribable to the CO_2 release, due to the possible reduction of Fe_2O_3 by CO, and a H_2S retention soon after the sulphidation beginning, according with the following reaction:[5]

$$Fe_2O_3 + 2\,H_2S + CO \rightarrow 2FeS + 2H_2O + CO_2 \qquad \textit{equation 7.1}$$

It is important to note that due to the high content of CO in the mixture its reduction as an effect of the reaction cannot be appreciated.

However, the slight decrease of H_2 in combination with the increase of H_2O, does not exclude that the reduction of iron oxide by H_2 can take place (*equation 7.2*):[5]

$$Fe_2O_3 + 2\,H_2S + H_2 \rightarrow 2FeS + 3H_2O \qquad \textit{equation 7.2}$$

In the case of Fe_TiO_2, the sharp band deriving from the release of CO_2 due to the reduction of the Fe(III) based-phase (equation 7.1) is accompanied by another broad contribute. In order to better understand this behaviour and assure the inertness of the mesostructured titania support, a sulphidation run has been carried out also on TiO_2 (Figure 7.5). Even if the support result to be inert toward H_2S, a remarkable release of CO_2 was detected, probably due to the reduction of Ti^{4+} to Ti^{3+}.[6] Therefore, this reaction could justify the second slow release of CO_2.

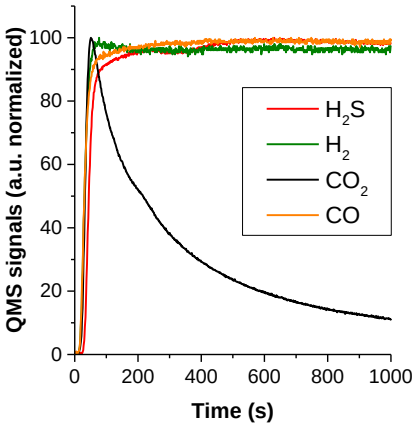

Figure 7.5 H_2S, H_2, CO_2 and CO normalized QMS profiles during the first sulphidation of the bare mesostructured TiO_2

Figure 7.6 shows the gases profiles of the two composites during the second sulphidation run. It is worth nothing that a remarkable amount of H_2 (almost 10 % of the normalized signal) and CO_2 are formed for both sorbents soon after the sulphidation beginning, according to the water gas shift reaction (equation 7.3). Being proved that magnetite phase (Fe_3O_4) is the catalyst of this reaction,[5] its formation can be hypothesized.

$$CO + H_2O \rightleftarrows H_2 + CO_2 \qquad \textit{equation 7.3}$$

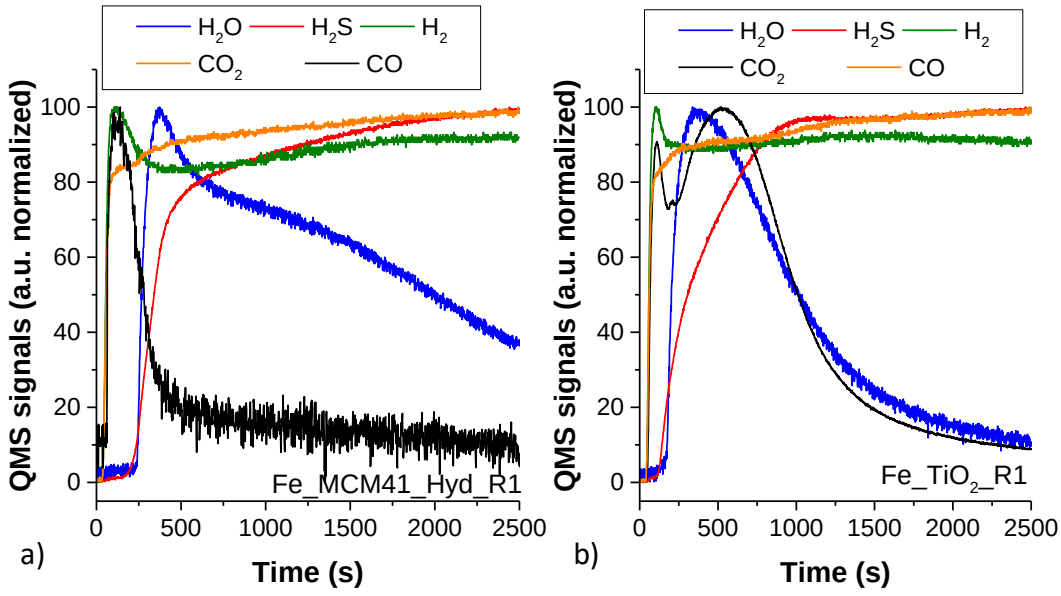

Figure 7.6 H_2O, H_2S, H2, CO_2 and CO normalized Quadrupole Mass Spectrometer (QMS) profiles during the second sulphidation of the samples Fe_MCM41_Hyd (a), Fe_TiO_2 (b)

7.4.2 Regeneration runs

The regeneration process, carried out at 500 °C for 2 hours for Fe_MCM41_Hyd (Chapter 5, paragraph 4.2 for more details) and at 350 °C for 2 hours in the case of the Fe_TiO_2, was

monitored by both a thermal conductivity detector (TCD) and a quadrupole mass spectrometer (QMS). As an example, the first regeneration run for the Fe_MCM41_Hyd and Fe_TiO_2 composites is reported in

Figure 6.4 TCD profile and SO_2 and O_2 Quadrupole Mass Spectrometer (QMS) signals of Fe_MCM41_Hyd (a) and Fe_MCM48 (b) during the first regeneration run.

, being the two further regenerations very similar.

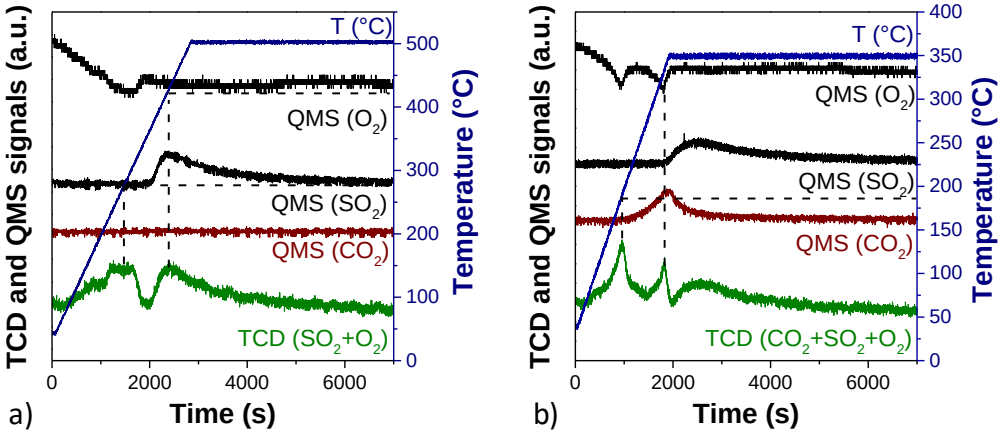

Figure 7.7 Thermal conductivity detector (TCD) profiles and SO_2, O_2 and CO_2 Quadrupole Mass Spectrometer (QMS) signals of Fe_MCM41_Hyd (a) and Fe_TiO_2 (b) during the first regeneration run

The TCD profiles of the two sorbents are rather different. In the case of Fe_MCM41_Hyd, a first peak centred at about 275 °C, corresponding to the O_2 consumption (upper curve, QMS (O_2)) is accompanied with another one centred at about 425 °C due to a release of SO_2, as confirmed by the QMS (SO_2). Even though the regeneration of Fe_TiO_2 composite was performed at lower temperature than the Fe-MCM41_Hyd one in order to preserve the porous structure, the gases release demonstrate that sorbent is at least partially regenerated. TCD profile shows the presence of two sharp peaks centred at about 175 °C and 340 °C, associable to O_2 consumption (upper curve, QMS (O_2)) and a broad one due to SO_2 release, as confirmed by QMS (SO_2). Besides the typical signals of O_2 and SO_2, a further contribution due to the release of CO_2 was detected by QMS. In order to clarify this aspect, the regeneration run on the sulphided mesostructured anatase support was performed (Figure 7.8), revealing a CO_2 release without any O_2 consumption. Therefore, in spite of the different temperature of the release (about 340°C for Fe_TiO_2 and 125°C for TiO_2) it could be hypothesized that CO_2 derives from an adsorption at the anatase surface.

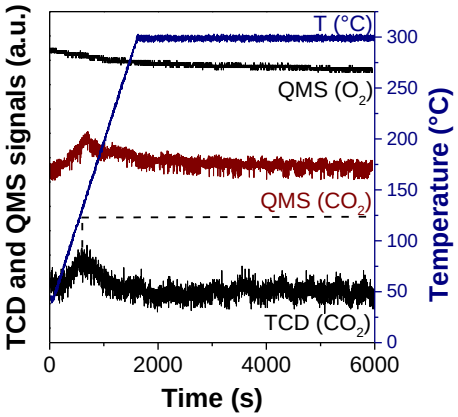

Figure 7.8 TCD profile and CO_2 and O_2 QMS signals of mesostructured bare TiO_2

The presence of magnetite, previously hypothesized, cannot be excluded due to its possible formation during the regeneration run, according to this reaction:[7]

$$Fe_3S_4 + 2O_2 \rightarrow Fe_3O_4 + 4S \qquad \textit{equation 7.4}$$

A further hypothesis can be the reaction of the sulphidated species with the SO_2, formed during the regeneration process (equation 7.5).[8]

$$3FeS_{1-x} + 2SO_2 \rightarrow Fe_3O_4 + (5-3x)S \qquad \textit{equation 7.5}$$

Unfortunately, WA-XRD analysis does not show any evidence of the presence of sulphur, thus some other phases, like hematite, has to be hypothesized. In fact, it is reported in the literature that hematite in reducing atmosphere and relatively mild temperature (300-450 °C) can form magnetite justifying the water gas shift reaction.[9]

7.5 Regenerated sorbents characterization

As expected by the performances, the porous structure is retained for both sorbents (Fe_MCM41_Hyd_R3 and Fe_TiO_2_R3) also after three repeated sulphidated-regenerated cycles (Figure 6.5 and Table 6.4). A slight decrease in the surface area from 744 to 695 m^2/g with an almost overlapped PSD is observed for Fe_MCM41_Hyd_R3 when compared with fresh one. In the case of Fe_TiO_2_R3, a greater variation with respect to the fresh one is revealed both in the surface area and PSD. However, the performances do not seem to be influenced by the worsening of the textural properties.

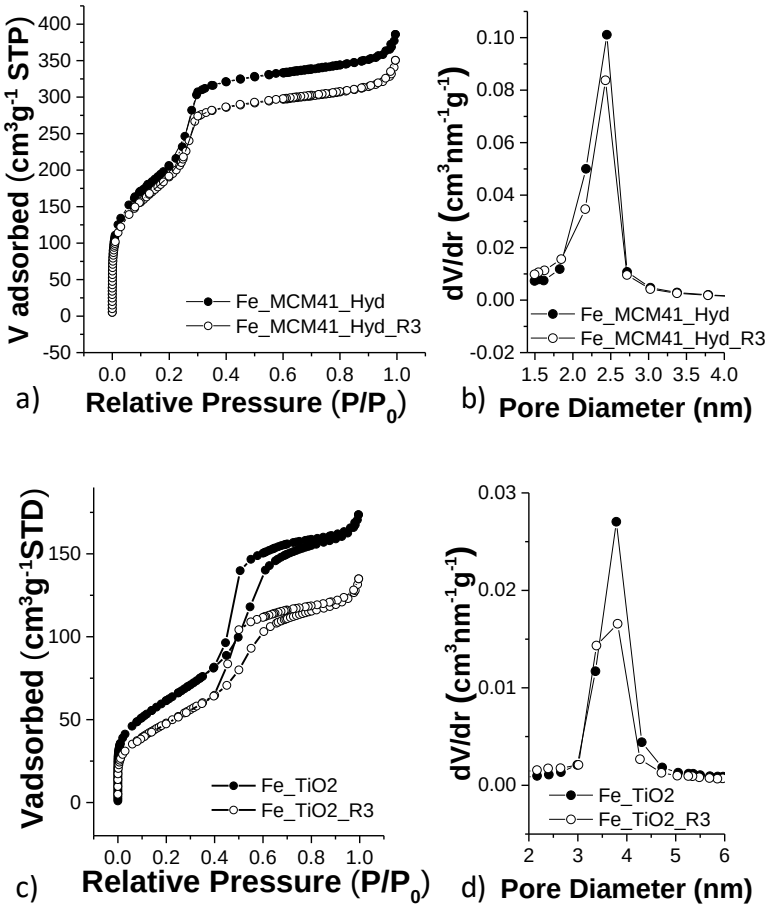

Figure 7.9 N_2 adsorption-desorption isotherms, pore size distributions of: Fe_MCM41_Hyd and Fe_MCM41_Hyd_R3 (a, b); Fe_TiO_2 and Fe_ TiO_2_R3 (c, d)

Sample	S_{BET} (m^2g^{-1})	V_p (cm^3g^{-1})	D_{pore} (nm)	w_t (nm)	d_{100} d_{211}	a_0
Fe_MCM41_Hyd	744	0.60	2.4	2.0	3.8	4.4
Fe_Hex_Hyd_R3	695	0.57	2.4			
Fe_TiO_2	223	0.24	3.8	4.8	7.5	8.7
Fe_ TiO_2_R3	177	0.21	3.6			

Table 7.5 Textural features obtained by N_2-physisorption data for fresh and three times-regenerated composites. The last two columns list the d-spacing (d_{100} and d_{211}) and lattice parameter (a_0) obtained from the LA-XRD data

7.6 Discussion

Even if the number of papers in which the performance of nanocomposites as H_2S removers have been gradually increasing during the last years,[7,10–13] just in few cases the studies are carried out under a simulated sour syngas. Nevertheless, the crucial step before proposing a material for a specific application is to simulate as close as possible the actual operating conditions.

Therefore, starting from the promising results obtained for MCM41-based sorbents in an atmosphere containing only H_2S in helium, we decided to move on toward the use of gaseous mixture (sour syngas) containing besides H_2S, also CO and H_2. In this context, among the different MCM41-based systems, Fe_MCM41_Hyd has been chosen to be tested also under sour syngas due to its high H_2S performance and thicker silica walls with respect to the others, that should assure long lifetime sorbent. Moreover, a nanocomposite made up of an iron phase embedded on mesostructured anatase (Fe_TiO_2) has been synthesized for the first time and tested for the specific application. The H_2S removal tests point out as the promising performance of Fe_MCM41_Hyd obtained in H_2S/He mixture is maintained also when a sour syngas is used, as proved by the similar SRC values and the steady performances after the first sulphidation (Figure 7.10a). Furthermore, the H_2 enrichment at the expense of CO, according to the water gas shift reaction (WGS) (*equation 7.3*) takes place during the second sulphidation. This result represents a further positive aspect considering that conventionally, IGCC plants include after a desulphidation step, a H_2 enrichment of the syngas in through WGS reaction by iron-oxide based catalysts. Commonly Fe_2O_3 (hematite),[9] with Cr_2O_3 and MgO are used, and under WGS reaction conditions the formed magnetite (Fe_3O_4) results to be the active phase for the reaction.[5] Taking into account these findings, and considering that WGS reaction does not occur during the first sulphidation run, once again we can confirm the presence of maghemite in the fresh MCM41-based sorbents, and hypothesize the formation, at least partial, of hematite phase starting from the first regeneration.

The use of a crystalline support with a different chemical nature with respect to amorphous silica MCM41 has caused remarkable effects in the dispersion of the iron oxide phase, as well as in the SRC values (Figure 7.10a). Indeed, no experimental evidence of the presence of maghemite as in the case of MCM41 and SBA15 support has been found in the fresh sorbents, and the ^{57}Fe Mössabauer spectroscopy together with DC magnetometry in this case cannot univocally identify the iron-based phase. Considering this fact, the worse H_2S removal capacity of the Fe_TiO_2 composite with respect to the Fe_MCM41_Hyd one could be correlated both to the lower surface area, that result to be more than 3 times lower, and to the different iron-based active phase. However, unexpectedly, the TiO_2 support, that results inert toward H_2S, reacts with CO forming CO_2 due to the reduction of the Ti^{4+} to Ti^{3+}.[6] The CO_2 amount result seventy times bigger than the CO_2 formed during the reduction of the iron oxide phase in the Fe_MCM41_Hyd (see Figure 7.10b, in which the CO_2 profiles are not normalized). This detrimental effect can represent a serious drawback for the use of Fe_TiO_2 in this specific application.

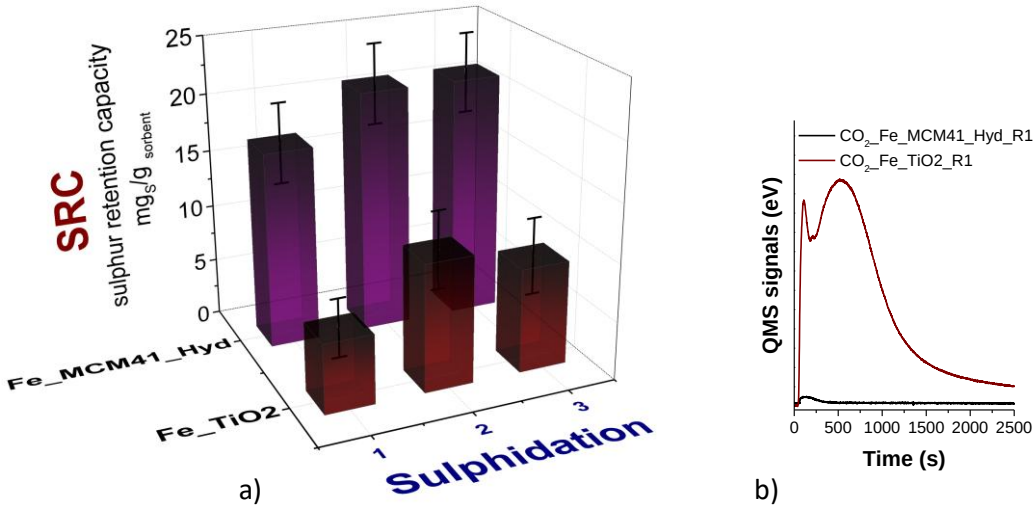

Figure 7.10 Comparison of SRC values of Fe_MCM41_Hyd and Fe_TiO_2 sorbents (a); CO_2 release during the second sulphidation runs of Fe_MCM41_Hyd and Fe_TiO_2 sorbents (b)

7.7 Conclusion

In this chapter, we proved that MCM41-based sorbents can be proposed as efficient and regenerable systems for H_2S removal at mid temperature from sour syngas. Not only the presence of other than H_2S reducing species (H_2 and CO) does not affect the sulphur retention capacity, but the occurrence of the water gas shift reaction causes the H_2 enrichment of the gaseous mixture. These findings prove the actual possibility to employ these materials for the selected application.

Concerning the mesostructured anatase-based sorbent, even if the results seem disheartening for this particular application, it can be proposed for other applications due to its interesting features. In fact, the support is easily functionalizable and the composite retain the porous structure also under repeated sulphidation and regeneration cycles in the mid-temperature conditions. Therefore, this attempt goes over the single use in this specific field, but represents one of the rare attempts to obtain a mesostructured metal oxide composite. It is worth noting that TiO_2@Fe_xO_y composites made up of mesoporous amorphous titania or anatase and maghemite/hematite/magnetite are widely proposed in a great variety of applications such as enhanced photoelectrochemical[14] water spitting and photocatalysis[15], and the use of mesostructured crystalline anatase can improve significantly the final performances of the composite.

References

1 G. Huang, E. He, Z. Wang, H. Fan, J. Shangguan, E. Croiset and Z. Chen, *Ind. Eng. Chem. Res.*, 2015, **54**, 8469–8478.

2 R. A. Borzi, S. J. Stewart, G. Punte, R. C. Mercader, M. Vasquez-Mansilla, R. D. Zysler and E. D. Cabanillas, *J. Magn. Magn. Mater.*, 1999, **205**, 234–240.

3 C. E. Rodríguez-Torres, A. F. Cabrera, L. A. Errico, C. Adán, F. G. Requejo, M. Weissmann and S. J. Stewart, *J. Phys. Condens. Matter*, 2008, **20**, 135210.

4 M. Thommes, K. Kaneko, A. V. Neimark, J. P. Olivier, F. Rodriguez-Reinoso, J. Rouquerol and K. S. W. Sing, *Pure Appl. Chem.*, 2015, **87**, 1051–1069.

5 Y. H. Lin, Y. C. Chen and H. Chu, *Chemosphere*, 2015, **121**, 62–67.

6 L.-B. Xiong, J.-L. Li, B. Yang and Y. Yu, *J. Nanomater.*, 2012, **2012**, 1–13.

7 C. Cara, E. Rombi, A. Musinu, V. Mameli, A. Ardu, M. Sanna Angotzi, L. Atzori, D. Niznansky, H. L. Xin and C. Cannas, *J. Mater. Chem. A*, 2017, **5**, 21688–21698.

8 S. C. Tseng, S. S. Tamhankar and C. Y. Wen, *Chem. Eng. Sci.*, 1981, **36**, 1287–1294.

9 R. Bouarab, S. Bennici, C. Mirodatos and A. Auroux, *J. Catal.*, 2014, **2014**, 1–6.

10 M. Mureddu, I. Ferino, A. Musinu, A. Ardu, E. Rombi, M. G. Cutrufello, P. Deiana, M. Fantauzzi and C. Cannas, *J. Mater. Chem. A*, 2014, **2**, 19396–19406.

11 M. Mureddu, I. Ferino, E. Rombi, M. G. Cutrufello, P. Deiana, A. Ardu, A. Musinu, G. Piccaluga and C. Cannas, *Fuel*, 2012, **102**, 691–700.

12 L. Li, T. H. Sun, C. H. Shu and H. B. Zhang, *J. Hazard. Mater.*, 2016, **311**, 142–150.

13 B. Elyassi, Y. Al Wahedi, N. Rajabbeigi, P. Kumar, J. S. Jeong, X. Zhang, P. Kumar, V. V. Balasubramanian, M. S. Katsiotis, K. Andre Mkhoyan, N. Boukos, S. Al Hashimi and M. Tsapatsis, *Microporous Mesoporous Mater.*, 2014, **190**, 152–155.

14 H. Han, F. Riboni, F. Karlicky, S. Kment, A. Goswami, P. Sudhagar, J. Yoo, L. Wang, O. Tomanec, M. Petr, O. Haderka, C. Terashima, A. Fujishima, P. Schmuki and R. Zboril, *Nanoscale*, 2016, **9**, 134–142.

15 B. Pal, M. Sharon and G. Nogami, 1999, **59**, 254–261.

Conclusions and future insights

This thesis deals with the development of mesostructured nanocomposites made up of a siliceous (MCM41S) or a non-siliceous (TiO_2 in form of anatase phase) mesostructured support and an iron-based active phase homogenously dispersed within the pores and their use as sorbents for H_2S removal at mid-temperature. To this aim, from one side, different synthetic approaches were set up to tune both the features of the support and the iron oxide active phase embedded into the mesochannels. From the other side, a careful and detailed characterization of the supports (WA-XRD, LA-XRD, N_2-physisorption, TEM, DLS) and of the iron oxide-composites (WA-XRD, LA-XRD, N_2-Physisorpion, TEM, EDS-STEM, ^{57}Fe Mössbauer spectroscopy, DC magnetometry) was carried out in order to correlate the features of the sorbents with their performances, and therefore to properly design a synthetic strategy to develop a sorbent able to guarantee high performances for a higher and higher number of cycles. Concerning the H_2S removal tests, both sulphidation and regeneration processes were carried out in the mid-temperature range, and studied by monitoring the formation of different outlet gases species by thermal conductivity detector and quadrupole mass spectrometer, to understand the evolving gas-solid reactions of the processes. The sulphur retention capacity for each sorbent was evaluated under three repeated cycles, and the porous stability of the three times sulphided-regenerated sorbent were verified. In order to verify the possibility of using the most promising sorbents in conditions simulating the actual syngas, the performances obtained in a simplified system with H_2S/He atmosphere were further compared to those obtained in a simulated sour syngas (CO, H_2, H_2S).

Some of the notable achievements of this work are listed below for both the **mesostructured siliceous-based sorbents** and **mesostructured anatase-based sorbent.**

For the mesostructured siliceous-based sorbents:

- novel mesostructured iron oxide-MCM41S composites with hexagonal (MCM41) and cubic (MCM48) porous structure in form of micrometric and nanometric particles have been successfully synthesized using a *Two-Solvents* incipient impregnation approach;
- the combined use of WA-XRD, ^{57}Fe Mössbauer spectroscopy and DC magnetometry has permitted to identify maghemite (γ-Fe_2O_3) in form of ultrasmall nanoparticles as active phase, in all iron oxide-MCM41S composites;

- all the **γ-Fe_2O_3@MCM41S** composites show better and more steady performances under three repeated sulphidation and regeneration cycles than those of an unsupported commercial sorbent. Specifically, the sulphur retention capacity (SRC) of the best sorbent (Fe_MCM41_M) is twice and twenty times higher than that of the commercial one in the first and successive sulphidation, respectively.
- among the γ-Fe_2O_3@MCM41S composites, both micrometric and nanometric γ-Fe_2O_3@MCM41 sorbents (Fe_MCM41_M, Fe_MCM41_Hyd, Fe_MCM41_N) show better performance than γ-Fe_2O_3@SBA15, recently proposed as efficient sorbent for H_2S. In particular, the SRC of the best MCM-41-based sorbent (Fe_MCM41_M) is more than twice and one and half times higher than that of Fe_SBA15 for the first and successive sulphidations, respectively. This result can be correlated to the higher surface area and the higher crystallinity of the maghemite nanoparticles in the Fe_MCM41_M.
- The comparison between micrometric Fe_MCM41_M and nanometric Fe_MCM41_N composites pointed out that, although the shorter length of the pores that should improve the accessibility to the active phase, the nanometric composite shows the worst performance due to the collapse of the porous structure under repeated cycles.
- The comparison between micrometric Fe_MCM41_M composite and micrometric Fe_MCM48 pointed out that, although the interconnection of the pores typical for a cubic structure should improve the accessibility to the active phase, the Fe_MCM48 composite shows the worst performance due to the collapse of the fragile porous structure made up of very thin silica walls.
- Micrometric Fe_MCM41_Hyd, in which the support has been submitted to an additional hydrothermal treatment to strengthen the porous structure (thicker mesochannels walls), shows steady performances and very similar to those of the micrometric Fe_MCM41_M in all three cycles. Considering their possible use for a high number of cycles, Fe_MCM41_Hyd should guarantee a longer lifetime.
- The comparison of the performances of Fe_MCM41_Hyd under a H_2S/He atmosphere and a simulated sour syngas atmosphere (H_2S, CO, H_2) highlighted that, although the presence of other reducing gases as CO and H_2, the promising performances are retained. Furthermore, an H_2 enrichment has been evidenced as positive possible effect from water gas shift reaction.

In the light of these results, this work highlights that mesostructured Fe_2O_3@MCM-41 composites can be proposed as promising sorbents for H_2S removal at mid-temperature due to

the high surface area, the stability of the porous structure and the homogenous dispersion of ultrasmall crystalline maghemite nanoparticles within the mesochannels. Furthermore, the high and steady H_2S removal capacity even under a sour syngas atmosphere and the regeneration temperature in the mid-temperature range render Fe_2O_3@MCM-41 composites a potential new class of regenerable sorbents for thermally efficient cleaning up of sour syngas produced from coal feedstock.

In the future in order to maximize the performances of these composites and make them proposable as cleaning technology in Integrated Gasification Combined Cycles (IGCC) systems, it could be interesting:

- to evaluate loadings higher than 10 %w/w. However, in order to assure a high dispersion into the pores and avoid plugging phenomena, the loadings cannot be too high. A good compromise could be 15-20 % w/w.

- to evaluate a higher sulphidation temperature and a regeneration temperature equal to the sulphidation one. A good compromise could be 400 °C, temperature that could assure even higher H_2S removal capacity than 300 °C and a good regenerability, being the average regeneration temperatures for Fe_2O_3 near 400 °C.

- to evaluate the possibility of increasing the crystallinity of iron oxide nanoparticles through prolonged or higher temperature calcination or using alternative impregnation procedures.

- to evaluate the stability of the performances in a higher number of cycles.

For the mesostructured non-siliceous TiO_2-based sorbent:

- novel mesostructured iron oxide-TiO_2 composite with hexagonal porous structure in form of micrometric particles has been synthesized for the first time by using EISA method for the support and *Two-Solvents* incipient impregnation approach for the dispersion of the active phase.
- the combined use of WA-XRD, ^{57}Fe Mössbauer spectroscopy and DC magnetometry techniques excluded the formation of a ferro-ferrimagnetic phase as in the case of siliceous sorbents, and hypothesize the formation of ultrasmall particles of an antiferromagnetic Fe^{3+}-based system or Fe-doped TiO_2.

- The performance under sour syngas, although half than that of the most promising MCM41 sorbent (Fe_MCM41_Hyd) results to be good and steady after the first sulphidation cycle.

Even if the performances of the iron-based-TiO_2 are worse than those obtained for siliceous based-composites, there is a great interest in TiO_2@Fe_xO_y composites, due to their potential application in enhanced photoelectrochemical water splitting and photocatalysis. Therefore, this attempt goes over the single use in this specific field, but represents one of the rare example of synthesis and application of a mesostructured metal oxide composite.

Therefore, future perspectives can be:

- studying the actual composition and structure of the iron oxide active phase in the Fe_TiO_2 by X-Ray Photoelectron Spectroscopy (XPS) and X-Ray Absorption techniques (EXAFS, XANES);

- studying the effect on the Fe_TiO_2 performances and thermal stability of changes in support's features (crystallinity, pore size, wall thickness) by using different block copolymers during the EISA synthesis;

- testing the suitability of this system for As (III) removal, being able to combine in a multifunctional material both the arsenic adsorption ability of the iron oxide phase and the photocatalytic activity of the anatase.

Appendix

Materials, methods, characterization techniques and experimental setup

In this section will be described the experimental setup employed to study the sulphidation and regeneration proprieties of the sorbent, and a description of the scale-laboratory pilot plant will be presented. Finally, the characterization techniques employed during this work.

Sulphidation retention capacity and lab-plant for H_2S removal.

Determination of the sulphur retention capacity

The desulphidation performance of each sorbent were determined by the breakthrough curve analysis. The breakthrough curve reports the concentration of the adsorbate (H_2S) in the outlet gas from the reactor as a function of the time. The typical profile of this curve has been reported in Figure A.1a. The shape of the breakthrough curve contain information about the mass transfer of the adsorptive-adsorbens system. The profile tendency of the curve can be explained considering the concentration of adsorbate (H_2S) within the sorbent as a function of the time, as represented on the Figure A.1b: when fluid starts to flow to the bed, it comes in contact with the first layer of the sorbents (t_1). Quickly, the amount of available sorbent fall down and the adsorbed close on the first layer will be saturated. In this case, the fluid emerging from the bed will have no H_2S remaining, and this situation will be kept until all the sorbent will not be saturated (t_2). The break point occurs when the H_2S concentration begins to increase in the outlet gas (t_3). Therefore, the estimation of the time passed until the break point Figure A.1a occurs can be directly correlated to the removal capacity of the sorbent.

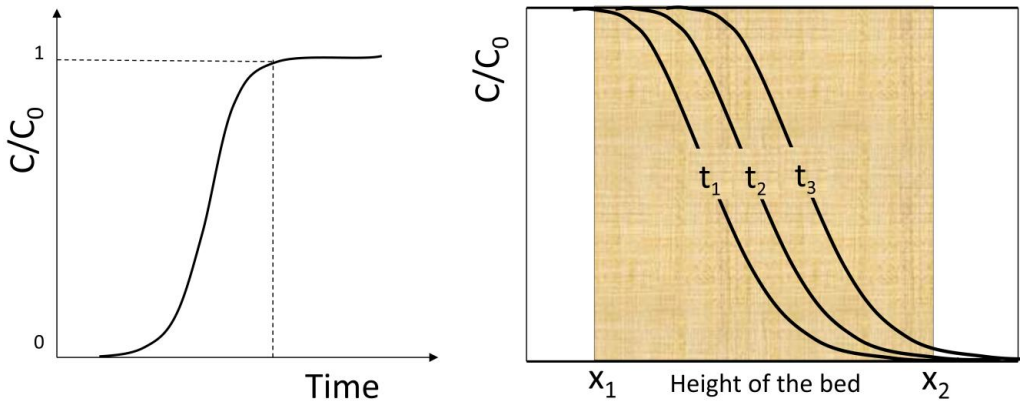

Figure A.1 Typical breakthrough curve (a) development and progression of a transition gas along the bed: transition zones at different times t1, t2 and t3 (b).

Therefore, for a breakthrough curve, two values can be extract and used to evaluate the H_2S removal performance of the sorbent:

Breakthrough time (t_b): defined as the time passed between the beginning of the desulphidation run and moment in which the H_2S concentration reached a set value in the outlet gas (in our experiment set up to 100 ppm)

Breakthrough capacity or sulphur retention capacity (SRC): that represent the mass of sulphur adsorbed (in mg) per gram of sorbent until the breakthrough time. It was calculated according to the followed equation:

$$SRC = \frac{V_{H_2S} \cdot t_b \cdot C_{A,in} \cdot MW_S}{W_{sorb}}$$

Where :

V_{H2S}: volumetric rate of feed stream ($m^3 \cdot s^{-1}$)

T_b: breakthrough time (s)

$C_{A,in}$: H_2S concentration ($mol \cdot m^{-3}$)

M_{Ws}: molecular weight of elemental sulphur ($g \cdot mol^{-1}$)

W_{sorb}: adsorbed loading in the reactor (g)

Description of the desulphidation-regeneration experimental setup

The desulphidation performance were detected at mid-temperature (300°C) and atmospheric pressure, using initially a reactant gas containing 15 200 ppm (1.52 vol %) of H_2S in helium (inlet flow, 20 cm^3 min^{-1}), and successively a simulated syngas with a composition of 1.52 vol % H_2S, 25 vol % CO and 15 vol % H_2, and N_2 as balance gas (inlet flow, 20 cm^3 min^{-1}). To determine the desulphidation and regeneration activity, 50 mg of composite were placed on a quartz wool bed (50 mg) in a vertical quartz tubular reactor coaxially located in an electrical furnace. Before desulphidation, a pre-treatment at 300°C for 30 min under a helium flow was performed to remove air and water from the sorbent and the reactor. Then, a reactant gas containing 15 200 ppm (1.52 v/v%) of H_2S (in helium or syngas) was fed into the reactor and the H_2S content in the outlet flow during the adsorption was monitored by using a quadruple mass spectroscopy (Thermo Electron Corporation). At the same time, H_2O and SO_2 signals were also monitored when H_2S in helium was fed, while CO, CO_2, H_2 and H_2O signals were further monitored when syngas fed. When the H_2S outlet gas concentration reached 15 200 ppm, the

measurement was stopped and the system was purged in flowing helium (20 cm^3min^{-1}) for 1 hour. The sulphur retention capacity of the sorbents was obtained as the difference between the b_t time of the composite and the b_t value of the bare support. The error on SRC values was estimated at 2 $mg_S g_{sorbent}^{-1}$ by carrying out several sulphidation cycles on fresh portions of the commercial sorbent $Katalko_{JM}$ 32-5. A schematic representation of the experimental setup and a picture scale-laboratory pilot plant are reported in Figure A.2b.

a)  b) 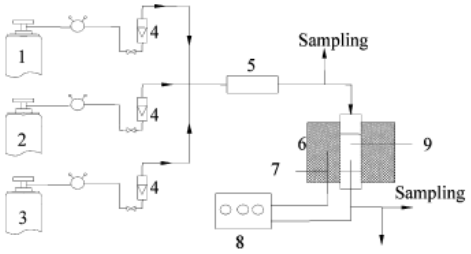

Figure A.2 a) schematic diagram of experimental setup 1) He 2) air 3)H_2S or syngas containing 1.52 vol % H_2S, 25 vol % CO and 15 vol % H_2 4)mass flow controllers 5) gases mixer 6) furnace 7) thermocouple 8)temperature controller 9) fixed-bed reactor. Reprinted with permission from ([6]). Copyright (2007) American Chemical Society b) scale-laboratory pilot plant for desulphidation-regeneration testes.

The regeneration process was performed on a Thermoquest 1100TPD/R/O apparatus equipped with a thermal conductivity detector (TCD) and a quadrupole mass spectrometer (QMS) for monitoring SO_2 and O_2 signals. The composite was heated under an air flow (20 cm^3min^{-1}) up to 500°C(heating rate, 10°$Cmin^{-1}$) and the temperature was kept constant for 3 hours. To identify the samples after different cycles of sulphidation or regeneration processes, a letter (S o R, respectively) and a number (denoting successive cycles) were added in the sample name.

The lifetime of the sorbent, intended as regenerability of the active phase, thermal stability and constant sulphur retention capacity value represent one of the key point in the evaluation of a sorbent. For this reason, three repeated sulphidation-regeneration cycles have been performed on each sorbent. At the end of the cycles, a study of the thermal stability of the sorbents were carried out by N_2-physisorption and low angle XRD diffraction analysis, in order to evaluate the thermal stability of the mesostructured after repeated sulphidation and regeneration cycles.

Characterization techniques

All siliceous and non-siliceous supports and the corresponding sorbents have been characterised by a multi-techniques approach in order to investigate their structural, textural and morphological. Moreover, the magnetic properties were studied for the iron based-composites.

Powder X-Ray Diffraction (PXRD)

Concerning the silica supports since they are amorphous materials, Powder X-Ray Diffraction has been no longer used to get information on their microstructure but instead to study the ordering of the mesoporous channels and the active phase dispersed within them in the composites. For this reason, the X-ray scattering phenomena have been exploited in the "*low-angle mode*" meaning that the X-rays are collimated towards the sample with an angle of incidence in the range 0.4°-3° paying attention to the use of proper slits in order to avoid any damage of the detector. Indeed, according to the Bragg's equation and for this angular range, it is possible to investigate distances in the range between 1.5 nm and 10 nm, which is exactly the typical order of magnitude of the d-spacings in the hexagonal and cubic porous lattices of the SBA15 and MCM41S. The lattice parameter (a_0) for the hexagonal (*P6mm* space group) and cubic (*Ia3d space group*) porous structures have been calculated according to the following equations:

$$a_0(\text{hex}) = \frac{2d_{100}}{\sqrt{3}} \qquad \textit{Hexagonal porous structure}$$

$$a_0(cub) = \sqrt{6} \cdot d_{211} \qquad \textit{Cubic porous structure}$$

Where d_{100} and d_{211} are the d-spacing of the most intense reflexes.

The X-Ray Diffraction has been also used to record the diffraction patterns in a "wide-angle mode" (2Θ=10°-70°) to verify the effectiveness of the impregnation process, i.e. to verify the presence of the reflections typical of iron oxides phases, to study their crystallinity and, whether it is possible, to identify the specific crystalline phase and to estimate the particle size by the Scherrer's equation:

$$< D_{XRD} >= \frac{K \cdot \lambda}{\beta \cdot cos\theta}$$

where, K is a constant taking into account the crystallite shape and the definition of both β and $< D_{XRD} >$, λ is the wavelength of the X-rays, β is the half-maximum line breadth of the peak.

All titania supports and the corresponding composite have been characterised by Powder X-ray Diffraction with regards to the previously-cited features as for the silica ones but also concerning their microstructure, to identify the TiO_2 crystalline phase.

All X-ray data have been collected by using a Seifert X 3000 diffraction system equipped with a Cu Kα source (λ=1.54056 Å) with a θ-θ Bragg–Brentano focalizing geometry, a graphite monochromator on the diffracted beam and a scintillation counter. For the *low-angle* measurements the investigated angular range 2Θ has been 0.8° - 2.5° for SBA-15 and 0.9° – 6° for MCM-41, while the wide-angle patterns have been collected between 10° and 70°. The divergence and scattering slits have been selected depending on the mode of use: 0.3 mm - 0.5 mm and 0.5 mm - 1.0 mm for the *low-angle* and *wide-angle* modes, respectively. The samples have been analysed in the form of powders by using a zerobackground silicon sample holder.

Transmission Electron Microscopy (TEM, EDS-STEM)

The ordering of the microporous channels has been investigated also by transmission electron microscopy for both the bare supports and the composites. In the case of the nanometric samples the particle size distribution has been calculated. Moreover, Energy Dispersive Scattering in Scanning TEM mode has been adopted to perform the chemical mapping of some composites (Fe_SBA15, Fe_MCM41_M, Fe_MCM41_N) and, in particular, to visualise the distribution of iron and, consequently, of the active phase in the support.

The transmission electron microscopy analyses have been carried out by means of a JEOL 200CX microscope operating at an accelerating voltage of 160 kV and a JEOL JEM 2010 UHR microscope equipped with a Gatan Imaging Filter (GIF). The particle size distribution has been determined through manual measuring by analysing several TEM images *by ImageJ software*, assuming spherical particles. The as-obtained size distribution has been then fitted by a Gaussian function to determine the mean particle size and the dispersity. The chemical mapping has been obtained in STEM mode using a FEI Talos F200X scanning/transmission electron microscope with a field-emission gun operating at 200 kV, equipped with a four quadrant 0.9-sr energy dispersive X-ray spectrometer. For all TEM analyses, the samples have been finely ground, dispersed in ethanol and sonicated. The suspensions were then dropped on carbon-coated copper grids and left to dry.

N_2-physisorption

The textural properties as surface area, pore volume, mean pore diameter and pore size distribution have been obtained by N_2-physisorption.

All nitrogen adsorption–desorption isotherms have been obtained at 77 K by means of a Micromeritics 2020 system. The samples have been pre-treated by heating up for 24 hours under vacuum at 250 °C (heating rate, 1 °C min^{-1}). The Brunauer–Emmett–Teller (BET) theory has been applied to calculate the specific surface area (S_{BET}) from the adsorption data in the P/P_0 range 0.05-0.17 for all MCM-41 supports and 0.05–0.3 for SBA-15 and TiO_2. The total pore volume (V_p) has been calculated at the point P/P_0 = 0.99 for all micrometric silica supports but the nanometric MCM41_N for which the computation has been done at P/P_0 = 0.87. The mean pore diameter (D_{pore}) has been determined by applying the Barrett–Joyner–Halenda (BJH) model to the isotherm desorption branch. In addition, the wall thickness (w_t) has been calculated in agreement with the following equations:

$$w_t(hex) = a_0 - D_{pore} \qquad \textit{Hexagonal porous structure}$$

$$w_t(cub) = \frac{a_0}{3.092} - \frac{D_{pore}}{2} \qquad \textit{Cubic porous structure}$$

Where a_0 is the lattice parameter calculated from the XRD data and D_{pore} is the pore diameter.

Dynamic Light Scattering

Dynamic Light Scattering (DLS) measurements have been conducted in order to determine the mean hydrodynamic diameter and its distribution for the nanometric sample MCM41_N. The analyses have been carried out by means of a Malvern Instrument Zeta Zetasized Ver 7.03, equipped with a He–Ne laser (λ = 663 nm, max 5 mW) and operating at a scattering angle of 173 °. 2 mg of silica particles have been dispersed in 2 mL of distilled water and sonicated for 2 min. An aliquot of the dispersion was then transferred in a plastic cuvette and analysed.

^{57}Fe Mössbauer Spectroscopy

The ^{57}Fe Mössbauer spectroscopy has been exploited together with DC/AC magnetometry to study the active phase, which XRD data have suggested to be in the form of small nanoparticles and therefore it is impossible to study by more conventional techniques. Details on the oxidation state, coordination environment and magnetic behaviour of iron in iron-containing materials can be indeed obtained by ^{57}Fe Mössbauer spectroscopy.

The ^{57}Fe Mössbauer spectra have been measured at room temperature on a Wissel spectrometer using transmission arrangement and proportional detector LND-45431 with ^{57}Co

diffused into a Rh matrix as the source moving with constant acceleration. The spectrometer has been calibrated by means of a standard α–Fe foil and the isomer shift has been expressed with respect to this standard at 293 K. The curve fitting of the spectra has been done by the NORMOS program using Lorentzian profiles to determine the isomer shift, the quadrupole splitting and the full width at half maximum.

DC magnetometry

DC magnetic properties have been studied by means of a Quantum Design PPMS Dynacool (H_{max} = 90 kOe) by using the VSM module owned by Centro Servizi di Ateneo per la Ricerca (CeSAR) which is gratefully acknowledged. Different kind of magnetic measurements have been carried out. The field dependence of the magnetisation has been studied at 5 K and 300 K between -90 kOe and +90 kOe.

The temperature dependence of the magnetisation has been studied by using Zero-Field-Cooled (ZFC), Field-Cooled (FC) protocols: the sample has been cooled down from 300 K to 2 K in zero magnetic field; then, the curves have been recorded under a static magnetic field of 250 Oe. M_{ZFC} has been measured during the warmup from 2 K to 300 K, whereas M_{FC} was recorded both during cooling and warmup. From these data, the characteristics temperatures T_{max} and T_{irr} have been computed as follows. T_{max} is the temperature of the maximum in the Zero Field Cooled curve. T_{irr} has been calculated by considering a 3% difference between the M_{FC} and the M_{ZFC}.

CHNS analyses

Elemental analysis (CHNS) was carried out with an EA 1108 CHS-O analyzer (Fisons Instruments) by total combustion of the samples in an oxygen and helium mixture.